

Numerical and Experimental Study of Heat and Mass Transfer Enhancement using Phase Change Materials

by

YASMIN KHAKPOUR

A Thesis

Submitted to the Faculty

of the

WORCESTER POLYTECHNIC INSTITUTE

In partial fulfillment of the requirements for the

Degree of Doctor of Philosophy

in

Mechanical Engineering

May 2014

APPROVED:

Professor Jamal S. Yagoobi, Thesis Advisor

Professor Richard D. Sisson, Graduate Committee Member

Professor John J. Blandino, Graduate Committee Member

Professor Michael T. Timko, Graduate Committee Member

Professor Cosme Furlong, Graduate Committee Representative

Abstract

Conventional heat transfer enhancement methods have focused on the surface characteristics of the heat-exchanger. The enhancement of heat transfer through altering the characteristics of the working fluid has become a new subject of interest. The application of phase change materials (PCM) in the working fluid is an example of achieving such enhancement which is being explored in recent years.

Micro-encapsulated phase change material (MEPCM) slurries show improved heat transfer abilities compared to single phase heat transfer fluids such as water due to their higher specific heat values in their phase change temperature range. Latent heat storage technology has seen a considerable scientific advancement since it can gain high energy storage density as well as capability of energy release at a constant temperature or over a small temperature range, corresponding to the phase transition temperature of the PCM.

The present work is a numerical and experimental study towards fundamental understanding of the impact of using PCM on thermal and fluid flow characteristics of different single-phase and two-phase heat transfer applications. The mathematical formulation to represent the presence of single and multi-component MEPCM is developed and incorporated into the numerical model for single-phase and two-phase fluid flow systems. In particular, the use of PCM in its encapsulated form for heat transfer enhancement of liquid flow in the presence of evaporation is explored. In addition, an experimental study is conducted to validate the numerical model in a setting of natural convection flow. Finally, the application of PCM in its layered form on the effectiveness of drying of moist porous materials (e.g. paper) is investigated.

Acknowledgements

This work was sponsored by a grant from National Science Foundation - Division of Chemical, Bioengineering, Environmental, and Transport Systems (CBET). I would like to take this opportunity to express my special appreciation to my advisor, Professor Jamal S. Yagoobi. I thank him for his guidance, encouragement and support, and his valuable advice during my graduate program. I would also like to gratefully and sincerely thank my thesis committee members, Professor Richard D. Sisson, Professor John J. Blandino, Professor Michael T. Timko and Professor Cosme Furlong. I appreciate their time and valuable comments. I am also very grateful to my dear family whose presence in my life is worth more than anything else and my wonderful friends who have always been encouraging me towards my academic success.

Contents

1	Introduction	3
1.1	Core Material of PCM	3
1.2	Encapsulation	5
1.3	Phase Change Slurries	7
1.4	Stability of the MEPCM	8
1.5	Specific Heat of PCM	8
1.6	Applications	9
2	Objectives	10
3	Numerical Study of Heat Transfer Characteristics of Liquid Flow in a Microtube with Blend of MEPCM	13
3.1	Objective	13
3.2	Introduction	14
3.3	Theory	17
3.4	Results and Discussions	22
3.5	Conclusions	32
4	Numerical Study of Liquid Film Flow Evaporation in the Presence of MEPCM	33
4.1	Objectives	33

4.2	Introduction	34
4.3	Theory	35
4.4	Operating Conditions	44
4.5	Numerical Technique	45
4.6	Results and Discussions	46
4.7	Conclusions	53
5	Natural Convection in an Enclosure with MEPCM	54
5.1	Objective	54
5.2	Introduction	55
5.3	Numerical Study	57
5.3.1	Theory	57
5.3.2	MEPCM Slurry Properties	60
5.3.3	Numerical Technique	63
5.4	Analysis of Numerical Results	64
5.5	Experimental Study	68
5.6	Experimental Procedure	71
5.7	Analysis of Experimental Results	77
5.8	Comparison of Numerical and Experimental Results	81
5.9	Conclusions	88
6	Enhancement of Paper Drying Process with PCM	89
6.1	Objective	89
6.2	Introduction	90
6.3	Approach	93
6.4	Theory	96
6.4.1	Governing Equations	98

6.4.2	Boundary Conditions	100
6.5	Numerical Technique	102
6.6	Case Description	104
6.7	Results and Discussions	106
6.7.1	Conventional Heating Arrangement	106
6.7.2	Periodic Heating Arrangement	108
6.8	Conclusions	116
7	Conclusions and Recommendations	117
7.1	Conclusions	117
7.2	Recommendations	118

List of Figures

1.1	Schematic representation of phase change phenomena in PCM [1].	4
3.1	Schematic of 2-D representation of axisymmetric numerical domain.	17
3.2	Variation of specific heat with temperature for encapsulated PCM1 and PCM2 derived from the heat-flow measurements of Sinha-Ray et [2].	20
3.3	Variation of slurrys effective specific heat with temperature for the case of single component and blend PCM.	23
3.4	Local heat transfer coefficient for MEPCM slurries of different types and different particle diameters. The heat transfer coefficient for pure-water is also presented for comparison.	26
3.5	The net enhancement in average heat transfer coefficient as a function of particle diameter for different slurries.	27
3.6	Variation of temperature, temperature difference and $c_{p,eff}$ along the tubes wall and axis for the case of encapsulated S2 slurry with $d_p = 10\mu m$	28
3.7	Local heat transfer coefficient for MEPCM slurries of different types and different MEPCM concentrations. The heat transfer coefficient for pure-water is also presented for comparison.	30
3.8	The net enhancement in average heat transfer coefficient as a function of MEPCM concentration for different slurries.	31

4.1	Schematic of 2-D representation of the numerical domain.(not to scale)	37
4.2	Variation of the specific heat of PCM with temperature [2].	42
4.3	Variation of slurry's specific heat with temperature for the case of pure R134a, 5% and 15% MEPCM slurry.	43
4.4	Comparison of current numerical model and Nusselt theory for falling film evaporation [3] for the evolution of liquid film thickness and local average heat transfer coefficient.	48
4.5	Temperature distribution and interface profile for $q''_w = 400 \text{ W/m}^2$ and $G_{in} = 10 \text{ kg/m}^2 \cdot \text{s}$ for (a) pure R134a and (b) $\xi_{in} = 15\%$ MEPCM slurry.	49
4.6	Variation of the Peclet number along the channel for $q''_w = 400 \text{ W/m}^2$	50
4.7	Variation of liquid film thickness along the channel for $q''_w = 400 \text{ W/m}^2$: (a) effect of MEPCM inlet concentration, ξ and (b) effect of liquid inlet mass flux, G	50
4.8	Variation of evaporation heat transfer coefficient along the channel for $q''_w = 400 \text{ W/m}^2$: (a) effect of MEPCM inlet concentration, ξ and (b) effect of liquid inlet mass flux, G	52
4.9	Variation of MEPCM concentration along the channel for various applied heat fluxes.	52
5.1	Schematic of the numerical domain and the boundary conditions.	58
5.2	Schematic description of fluid and thermal boundary conditions for the present numerical model.	59
5.3	DSC curves for the MEPCM used in this study [4].	61
5.4	Variation of (a) heat transfer coefficient of pure water and slurry with applied heat flux and (b) the ratio of heat transfer coefficient of slurry flow to that of water and the corresponding hot plate temperature with applied heat flux.	65

5.5	Dimensional velocity field at the symmetry plane, for (a) pure water and (b) 15% MEPCM slurry flow.	66
5.6	Dimensional temperature field at the symmetry plane, for (a) pure water and (b) 15% MEPCM slurry flow.	67
5.7	Schematic of the experimental setup.	68
5.8	The main enclosure.	69
5.9	The side wall copper plates.	70
5.10	The front window of the main enclosure.	71
5.11	Photo of the experimental setup arrangement.	72
5.12	Schematic of the experimental setup arrangement.	72
5.13	Samples of MEPCM slurries.	73
5.14	Flow rate vs. frequency of the flow meter.	76
5.15	The LabVIEW GUI for the current experiment.	76
5.16	Experimental measurement of temperature profile along the centerline for case of pure water for different tests.	78
5.17	Experimental measurement of temperature profile along the centerline for case of pure water and slurry of different MEPCM concentrations.	79
5.18	Experimental measurement of temperature profile along the centerline for case of pure water and slurry of different MEPCM types.	80
5.19	Variation of the deviation of local wall temperature from the mean temperature both calculated on the cold plate: Comparison of experimental measurement and numerical prediction for case of pure water.	81
5.20	Temperature profile across the centerline of the enclosure: Comparison of experimental measurement and numerical prediction for case of pure water and MEPCM slurry.	82

5.21	Experimentally measured temperature profile across the centerline for different MEPCM concentrations.	84
5.22	Variation of heat transfer coefficient (left) and its ratio with respect to the one for pure water with MEPCM concentration: Comparison of experimental measurement and numerical prediction	84
5.23	Average heat transfer coefficient for pure water and 15% MEPCM slurry at $q'' = 3524W/m^2$ and $T_c = 30^\circ C$: Comparison of experimental measurement and numerical prediction	85
5.24	Average heat transfer coefficient for pure water and 15% MEPCM slurry at $q'' = 2701W/m^2$ and $T_c = 20^\circ C$: Comparison of experimental measurement and numerical prediction	86
5.25	Average Nusselt number as a function of Ra number for case of pure water and 15% MEPCM slurry: Comparison of experimental measurement and numerical prediction	87
6.1	Schematic illustration of the approach presented in this work.	95
6.2	Variation of PCM specific heat during the solid-liquid phase change.	96
6.3	Schematic description of different phases during the drying process.	97
6.4	Schematic of the theoretical domain in the absence and presence of PCM layer.	98
6.5	Schematic representation of drying process in the conventional heating arrangement.	104
6.6	Schematic representation of drying process in the periodic heating arrangement.	105
6.7	Time evolution of paper sheet average temperature (top) and moisture content (bottom) in the presence and absence of PCM layer for conventional heating arrangement.	107

6.8	Temperature profiles across the paper sheet in the presence and absence of PCM layer for different points during the drying process for conventional heating arrangement.	109
6.9	Moisture content profiles across the paper sheet in the presence and absence of PCM layer for different points during the drying process for conventional heating arrangement.	110
6.10	Time evolution of paper sheet average temperature (top) and moisture content (bottom) in the presence and absence of PCM layer for periodic heating arrangement.	113
6.11	Temperature profiles across the paper sheet in the presence and absence of PCM layer for different points during the drying process for periodic heating arrangement.	114
6.12	Moisture content profiles across the paper sheet in the presence and absence of PCM layer for different points during the drying process for periodic heating heating arrangement.	115

List of Tables

1.1	Measured thermophysical data of some PCMs [5].	6
3.1	Summary of dimensionless hydrodynamic and energy boundary conditions.	18
3.2	Physical properties of PCM and he PMMA materials [6].	19
3.3	Summary of operating conditions.	23
3.4	Quantitative impact of particle diameter on slurry’s thermal conductivity. .	25
4.1	Summary of hydrodynamic and energy boundary conditions.	40
4.2	Physical properties of the MEPCM core, PS shell and R134a	40
4.3	Summary of the operating conditions.	45
5.1	Physical properties of the PCM and the PMMA material	61
5.2	PCM properties provided by PureTemp [4]	73
5.3	Summary of operating conditions.	74
5.4	Accuracy of the measurement devices.	77
6.1	Summary of mass transfer boundary equations.	103
6.2	Summary of energy transfer boundary equations.	103
6.3	Summary of the operating conditions for the present case study.	105
6.4	Summary of the properties for the present case study.	105
6.5	Correspondence of the cylinder numbers in the two heating arrangements.	108

Nomenclature

BW	basis weight; weight of air-dry sheet/sheet area, kg/m^2
c_p	specific heat at constant pressure, J/kgK
Cyl	cylinder number
d	particle diameter, m
D	diffusivity, m^2/s
D_h	hydraulic diameter, $D_h = 2\delta W/(\delta + W)$, m
DSC	differential scanning calorimetry
e	shear rate, $1/s$
f	conductivity ratio, k_{eff}/k_b
g	gravitational acceleration, m/s^2
G	mass flux, kg/m^2s
h	heat transfer coefficient, W/m^2K
h_{fg}	latent heat of evaporation, J/kg
H	height of the channel or the container, m
H	enthalpy, J/kg
J	mass flux, kg/m^2s
k	thermal conductivity, W/mK
K	permeability, m^2

L	length of the channel, m
\dot{m}	mass flow rate, kg/s
MC	moisture content per dry basis, kg/kg
$MEPCM$	micro encapsulated phase change material
n	normal vector
N	number of PCM blend components
P	pressure, Pa
PCM	phase change material
$PMMA$	poly-methymethacrylate
PS	Polystyrene
Pe	Peclet number, $Pe = Re.Pr$
Pr	Prandtl number, $Pr = \frac{c_p \mu}{k}$
Pe_p	Particle Peclet number, $Pe_p = \frac{ed_p^2}{\gamma}$
Pr	Prandtl number, $Pr = c_p \mu / k$
q''	heat flux, W/m^2
Re	Reynolds number, $Re = \rho u D_h / \mu$
S_E	source term in energy equation
St	Stokes number, $St = \tau \mu / d$
t	time, s
T	temperature, K
u	velocity in x direction, m/s
v	velocity in y direction, m/s
V	volume, m^3
W	width of the channel, m

x	horizontal coordinate axis
y	vertical coordinate axis
y	mole fraction
α	volume fraction of vapor phase
α	thermal diffusivity, m^2/s
γ	thermal diffusivity, $\gamma = k/\rho c_p$, m^2/s
Δ	liquid film thickness, m
δ	non-dimensional liquid film thickness, m
ρ	density, kg/m^3
ζ	particle volume concentration in the slurry
ϕ	particle mass concentration in the slurry
Φ	mass fraction of PCM material in the particle
Ψ_{vis}	viscous dissipation, W/m^3
χ	volume fraction of PCM material in the particle
τ	shear stress, Pa
θ	non-dimensional temperature
μ	dynamic viscosity, $Pa.s$
ν	kinematic viscosity, m^2/s
ω	moisture content, wet basis; weight of water/(weight of water + weight of dry fiber)

Subscripts

<i>a</i>	air
<i>ap</i>	apparent
<i>atm</i>	atmospheric
<i>b</i>	bulk
<i>c</i>	cold
<i>ca</i>	capillary
<i>cf</i>	carrier fluid
<i>cyl</i>	cylinder
core	core of the MEPCM
eff	effective
evap	evaporation
<i>f</i>	fiber
<i>h</i>	hot
<i>i</i>	index for particles
<i>in</i>	inlet
<i>int</i>	interface
<i>l</i>	liquid
<i>m</i>	mixture

<i>o</i>	outlet
<i>p</i>	particle
<i>s</i>	solid
<i>sh</i>	sheet
sat	saturation
shell	shell of the MEPCM
<i>th</i>	thermal
<i>v</i>	vapor
<i>w</i>	wall

Chapter 1

Introduction

Phase Change Materials (PCM) absorb and release heat at pre-set temperatures. Due to their high values of latent heat, they are capable of storing and releasing large amounts of energy during phase change. Figure 1 is a schematic representation of phase change phenomena in PCM ¹.

1.1 Core Material of PCM

The PCM materials are made, in large, from organic and inorganic compounds. The advantages characteristics of organic PCMs can be summarized as follows [7],

- non-corrosive
- chemically stable
- little or no subcooling
- compatible with most building materials
- high latent heat per unit weight

¹<http://www.microteklabs.com/how-do-pcms-work.html>

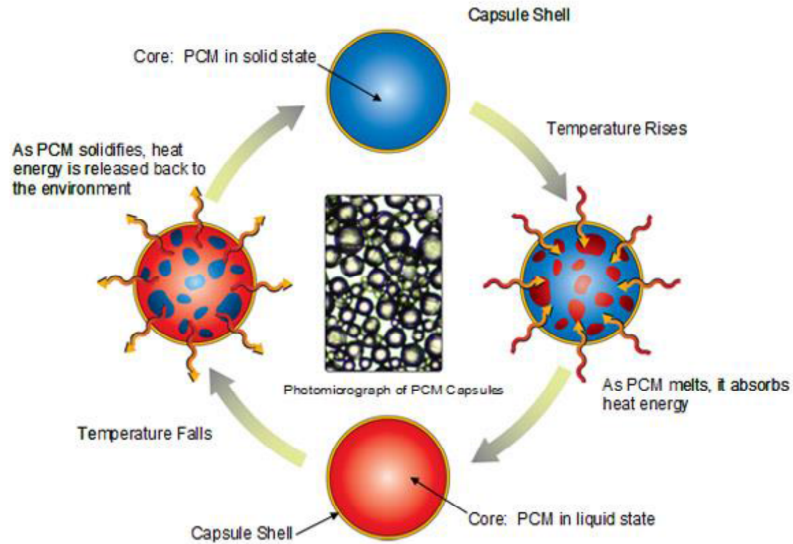


Figure 1.1: Schematic representation of phase change phenomena in PCM [1].

- low vapor pressure

And their disadvantages are,

- low thermal conductivity
- large volume change during phase change
- flammability

The advantages of non-organic PCM materials are as follows, [7]

- high latent heat per unit volume
- high thermal conductivity
- non-flammable and low cost compared to organic compounds

The disadvantages of the non-organic PCMs, however are them being corrosive and often having a significant subcooling and decomposition. Their applications, therefore, should be accompanied by the use of nucleating and thickening agents to minimize subcooling

and phase segregation. Extensive research is being conducted to discover new agents with the aforementioned properties.

An example of organic PCM is paraffin waxes which are cheap with moderate thermal storage densities (200 kJ/kg) and a wide range of melting temperatures [8–10]. They are manufactured to undergo negligible subcooling and are chemically inert and stable with no phase segregation. However, they have low thermal conductivity (0.2 W/mK), which limits their applications. Their thermal conductivity has been improved by metallic fillers, metal matrix structures, finned tubes and aluminum shavings were used to improve their thermal conductivity [11]. Also, the effect of adding nano-materials to enhance paraffins thermal performance has been explored recently [12].

In addition to their thermal properties, the density of a PCM is important because it affects its storage effectiveness per unit volume. Salt hydrates are generally denser than paraffins and, hence, are even more effective on a per volume basis. The change of volume with the transition, which is in the order of 10%, could represent a minor problem [13]. Table 1.1 presents the experimental thermophysical properties of both the liquid and solid states for several PCMs as reported by Lane [5, 14]. It is worth emphasizing that pure paraffin waxes are very expensive, and therefore, only technical grade paraffins can be used [14].

1.2 Encapsulation

The main objective of micro-encapsulation is to prevent the PCM from leaking into the base fluid while in liquid phase. In addition, the encapsulation results in improved heat transfer area and reducing a possible interaction with the outside environment while constraining the eventual volume change of the PCM during phase change. For instance, encapsulation of the phase change materials enables the particles to disperse in water and

Table 1.1: Measured thermophysical data of some PCMs [5].

Compound	Melting temp. (°C)	Heat of fusion (kJ/kg)	Thermal conductivity (W/m K)	Density (kg/m ³)
<i>Inorganics</i>				
MgCl ₂ · 6H ₂ O	117	168.6	0.570 (liquid, 120 °C) 0.694 (solid, 90 °C)	1450 (liquid, 120 °C) 1569 (solid, 20 °C)
Mg(NO ₃) ₂ · 6H ₂ O	89	162.8	0.490 (liquid, 95 °C) 0.611 (solid, 37 °C)	1550 (liquid, 94 °C) 1636 (solid, 25 °C)
Ba(OH) ₂ · 8H ₂ O	48	265.7	0.653 (liquid, 85.7 °C) 1.225 (solid, 23 °C)	1937 (liquid, 84 °C) 2070 (solid, 24 °C)
CaCl ₂ · 6H ₂ O	29	190.8	0.540 (liquid, 38.7 °C) 0.1.088 (solid, 23 °C)	1562 (liquid, 32 °C) 1802(solid, 24 °C)
<i>Organics</i>				
Paraffin wax	64	173.6	0.167 (liquid, 63.5 °C) 0.346 (solid, 33.6 °C)	790 (liquid, 65 °C) 916 (solid, 24 °C)
Polyglycol E600	22	127.2	0.189 (liquid, 38.6 °C) –	1126 (liquid, 25 °C) 1232 (solid, 4 °C)
<i>Fatty acids</i>				
Palmitic acid	64	185.4	0.162 (liquid, 68.4 °C) –	850 (liquid, 65 °C) 989 (solid, 24 °C)
Capric acid	32	152.7	0.153 (liquid, 38.5 °C) –	878 (liquid, 45 °C) 1004 (solid, 24 °C)
Caprylic acid	16	148.5	0.149 (liquid, 38.6 °C) –	901 (liquid, 30 °C) 981(solid, 13 °C)
<i>Aromatics</i>				
Naphthalene	80	147.7	0.132 (liquid, 83.8 °C) 0.341 (solid, 49.9°C)	976 (liquid, 84 °C) 1145 (solid, 20 °C)

to melt without any interaction between the PCM and the carrier fluid [15]. Examples of such use of encapsulation of dispersed PCMs are polymethyl methacrylate (PMMA), polystyrene (PS), polyethyl methacrylate (PEMA) and poly vinyl acetate (PVAc) [16]. While these particles can be made in variety of sizes, an example of such encapsulation is 20nm thickness of the shells which encapsulate particles of 1-20 μ m [15].

Lane [17, 18] has identified over 200 potential phase change heat storage materials melting from 10 to 90°C to be used for encapsulation. They successfully demonstrated the application of microencapsulation of CaCl₂ · 6H₂O in polyester resin for developments of wall and floor panels as well as its application in plastic film containers for heating systems using air as the heat transfer medium [18]. The encapsulation of PCMs into the micropores of an ordered polymer film was investigated by Stark [19]. They showed that paraffin wax and high density polyethylene wax can be infiltrated into extruded films of ordered polymer using solvent exchange technique so as to produce microcomposites

with PCM levels of the order of 40% in volume. These microcomposite films exhibit excellent mechanical stability under cyclic freezethaw conditions. The operating temperature of PCM materials was also subject of recent studies. Royon et al. [20] have developed a new material for low temperature storage. They contained the water as a PCM within a three dimensional network of polyacrylamide during the polymerization process. Recently Hong and Xin-shi [21] have employed a compound phase change material, which consists of paraffin as a dispersed phase change material and a high density polyethylene (HDPE) as a supporting material. This new generation phase change material is very suitable for application in direct contact heat exchangers. The 75% paraffin and 25% HDPE mixture provided a phase change material that has a latent heat of 157 kJ/kg compared to 199 kJ/kg for the paraffin used and with a transition temperature of approximately $57^{\circ}C$, which is close to that of paraffin.

All being said and despite the extensive research in area of microencapsulation of PCMs, their use was still limited due, in large part, to the cost associated with the encapsulation process [7, 14].

1.3 Phase Change Slurries

The mixtures of PCMs and carrier fluids are called MEPCM slurries. The heat transfer ability and energy transport ability of the MEPCM can be highly improved compared to the conventional heat transfer fluids such as water due to their higher effective specific heats in the phase change temperature range. Therefore, they have many potentially important applications in fields such as heating, ventilating, air conditioning, refrigeration and heat exchangers [16].

1.4 Stability of the MEPCM

The stability of PCM slurries is characterized by the number of operation cycles (i.e. heating and cooling cycles) they can withstand without degradation of their properties as well as the corrosive interaction of the PCM materials and the embodiment in which they are being used [22].

Kimura and Kai [23] have used NaCl to improve the stability of $\text{CaCl}_2 \cdot 6\text{H}_2\text{O}$, containing slightly more water than the stoichiometric composition. The salt was found to be very stable following more than 1000 heating-cooling cycles. Gibbs and Hasnain [24] have successfully demonstrated the thermal stability of paraffins by showing that their properties remain intact during extensive number of cycles with no interaction with the metals. Most investigations on corrosion tests using PCMs were performed with salt hydrates [25]. Further efforts have been conducted on the use of PCM for wallboards and the change of their thermal characteristics (e.g. [26] and references therein).

Gschwander et al. [15] also studied the stability of the MEPCM by exposing them to high shear stresses, that normally occur mainly in pumps and examined the compatibility of different components when used together with the MEPCM slurries. They concluded that centrifugal pumps are best suited for use in conjunction with MEPCM slurries without the PCM particles being self-destructed or destructive to the shells of the microencapsulation. This good stability of the capsules can further be improved by thickening the encapsulation shell, albeit that results in a smaller volume fraction occupied by the PCM material which adversely impacts the thermal performance of the MEPCM slurry.

1.5 Specific Heat of PCM

The heat of melting of PCM is measured by differential scanning calorimetry (DSC) where the temperature of a sample is increased linearly and the heat flux into the sample

is measured. The heat of melting is then calculated by using the known sample mass.

1.6 Applications

The PCM materials have been applied almost exclusively for thermal storage purposes, ranging from heat and coolness storage in buildings to thermal storage in satellites and protective clothing. A PCM with an easily adjustable melting point would be a necessity as the melting point is the most important criterion for selecting a PCM for passive solar applications. Many more applications are yet to be discovered [7, 14].

In addition to thermal storage applications, PCM materials have shown promising benefits for thermal management applications as technology advances in microchips, batteries, and various other small scale and high power applications are increasingly hindered by the thermal performance of such systems. For example, increasing the speed of microprocessors may depend on effective new thermal management techniques to dissipate high heat fluxes. Similarly, electronic actuators that may take the place of hydraulics and mechanical actuators in aircraft may require similarly effective thermal management schemes. It is desirable that these thermal management, i.e., thermal transfer, schemes meet the criteria of low power consumption, low physical volume, and low weight owing to the small scale of many intended applications. Further, it is desirable that the heat transfer system should have few moving parts, require very little maintenance, and perform reliably in variable environmental conditions [27].

Particles of microencapsulated PCM (3- 100 μm) and/or macroencapsulated PCM (1-3 mm) can be included within textile fibers, composites, and clothing to provide greatly enhanced thermal protection in both hot and cold environments [7, 28].

Chapter 2

Objectives

The core objective of this research is to provide fundamental understanding of heat transfer enhancement using micro encapsulated phase change materials (MEPCM) through numerical and experimental investigations. Formulations of fluid properties containing single-component as well as blend-component MEPCM are introduced and various scenarios including internal flow, free convection and film evaporation are studied. The objective of this research is also to investigate the effect of using a layered MEPCM in drying processes where the effective latent heat of the MEPCM enhances the moisture removal efficiency.

In general, this research is accomplished through five parts as summarized below,

I - Numerical Study of Heat Transfer Characteristics of Liquid Flow in a Micro-tube with Blend of Micro Phase Change Materials

- The mathematical formulation for calculation of thermal and flow properties of slurry flow with multi-component MEPCM particles is developed for the first time.
- Effect of various operating conditions including the ones pertaining to the flow as well as MEPCM particles on hydrodynamics and thermal characteristics of

the microtube flow is investigated.

- The change in flow and thermal characteristics due to using blend of MEPCM particles with different melting ranges along with single-component MEPCM is explored and compared to the case of pure water.

II - Natural Convection in an Enclosure with Micro Encapsulated Phase Change

Materials: A Numerical Study

- This part is an extension of the previous section to explore, numerically, the thermal and hydrodynamic characteristics of natural convection flow of MEPCM slurry.
- The heat transfer enhancement due to the use of MEPCM particles is quantified under various operating conditions.

III - Natural Convection in an Enclosure with Micro Encapsulated Phase Change

Material Slurry: An Experimental Study

- This experimental study aims to validate the numerical model developed in the previous section in the presence of MEPCM particles under various operating conditions.

IV - Liquid Film Evaporation in the Presence of Micro Encapsulated Phase Change

Materials: A Numerical Study

- The mathematical formulation for slurry flow in the presence of film evaporation is developed.
- The numerical model is demonstrated on a single-component MEPCM slurry liquid film flow subject to an external heat input applied at the channel wall.

- The numerical results for the flow and heat transfer characteristics, including the variation of liquid film profile and MEPCM concentration along the evaporation path are illustrated and physically analyzed.
- Effect of MEPCM particles on heat transfer enhancement of evaporating liquid film is quantified under various operating conditions.

V - Fundamental Study of Drying of Moist Porous Media in the Presence of Phase Change Materials

- An innovative drying concept is introduced that utilizes the latent heat of fusion associated with the phase-change of PCM to improve the energy efficiency of moisture extraction process from porous media.
- The mathematical model is developed for the transport characteristics of drying of moisture porous media and demonstrated on drying process in the presence of PCM as a thin layer.
- The numerical model is applied on a conventional setting for paper drying process as well as a proposed arrangement in which the benefits of using PCM in moisture removal is shown to be enhanced.
- The numerical results for the time-evolution of moisture content and temperature profile across the paper sheet are presented and physically analyzed.

Chapter 3

Numerical Study of Heat Transfer

Characteristics of Liquid Flow in a

Microtube with Blend of MEPCM

3.1 Objective

This numerical investigation explores the heat transfer characteristics of liquid flow with two- component (blend) micro encapsulated phase change materials (MEPCM) and compares them with those of a single component MEPCM slurry. The numerical domain is comprised of an axisymmetric microtube in contact with a finite-thickness solid zone with uniform heat flux applied on the solid outer wall. The ultimate objective is to demonstrate the tunability of PCM fluids thermal properties when the phase transition temperatures of the blend PCMs are chosen within a range required for a specific application. This is because different pure PCM materials store latent heat at a specific range of temperatures. The single and multi-component MEPCM slurry flows do not reach a fully developed condition as long as the MEPCM particles experience phase change in the developing

region. The local heat transfer coefficient strongly depends on the corresponding location of the melting zone interface.

3.2 Introduction

There has been a number of publications in regards to the application of Phase Change Materials (PCM) for heat transfer enhancement. Colvin and Mulligan [29, 30] reported that by using a slurry with phase change material, for the same temperature rise, the flow rate can be reduced to one-tenth and the pumping power can be reduced to one-hundredth for a given heat flux. Similar reductions in pumping power have also been reported by Goel et al. [31]. In an experimental study by Inaba et al. [32], the heat transfer enhancement of the plural (having different diameters) PCMs slurry has mainly been investigated experimentally under the flow conditions of both laminar and turbulent flow in a circular tube with a constant wall heat flux. The influence of latent heat evolved during the phase change process and microconvection around the PCM particles were clarified for both small sized PCM and plural PCMs slurries. Their experimental results demonstrated significant improvement in heat transfer coefficient of plural PCM slurry flows compared to that of pure water. They also showed that the wall surface temperatures of heating tube for the plural PCMs slurry were lower than those for small sized PCM slurry.

Alvarado et al. [33] determined the thermal performance of microencapsulated phase change material slurries containing n-Tetradecane. They reported thermal capacity enhancement of 40% for the MEPCM slurry (7% conc. by wt.). At higher mass fractions, experimental heat capacity enhancement increased to 70%. At lower mass fractions, the ratio of heat transfer coefficients of MEPCM slurry to that of pure water was 0.6 whereas at higher mass fractions, it decreased to 0.4, suggesting lower turbulence (due to higher

viscosity) at higher mass fractions. Their study on the effect of flow rate revealed that increase in flow rate had a more significant impact on the percentage of particles undergoing phase change than an increase in heat flux value.

In an experimental study conducted by Wang et al. [34] the pressure drop and local heat transfer coefficients of MEPCM slurries in a circular horizontal tube with constant heat flux at both laminar and turbulent flow conditions were investigated and the influences of various conditions on heat transfer performance were also studied. They concluded that heat transfer coefficients measured for MPCM slurry were significantly higher than for those for single-phase pure fluid flow in laminar flow conditions, but exhibit more complicated phenomenon at low turbulent conditions.

In the parametric study by Zhao et al. [35], they considered the effect of parameters such as Ste number, volume fraction, supercooling, phase change temperature range, ratio of particle size to tube radius and Re number on the enhancement of heat transfer for laminar flow of MEPCM slurries in were the most important parameters influencing the heat transfer enhancement of the microencapsulated suspension.

Sabbah et al. [36] studied the performance of water-based slurry in rectangular channels and showed that a significant increase in the heat transfer coefficient can be achieved under certain conditions of heat flux, channel inlet temperature, and the selected MEPCM melting temperature range. In another study, Sabbah et al. [37] measured the tube wall temperature profile, fluid inlet and outlet temperatures and determined the corresponding heat transfer coefficient for various operating conditions by covering a wide range of the controlling parameters, MEPCM concentration, heat flux, inlet temperature, and flow rates. Their results showed significant enhancements in heat transfer coefficient (up to 50%) and reduction in tube wall temperature (up to 40%). The numerical results provided in [38] are also validated against these experimental data. They also showed that the presence of MEPCM extends the thermal entry length by slowing the growth of the

thermal boundary layer.

Kuravi et al. [39] experimentally investigated the heat transfer performance of water-based MEPCM slurry (particle size 5 μ m) flow inside manifold microchannels of hydraulic diameter 170 μ m and reported poorer performance for the slurry compared to water. They stated that for developing flows, the performance of PCM slurry depends on various parameters such as base-fluid thermal conductivity, channel dimensions, amount of PCM melted, and particle mass concentration.

There are a few works that have studied the PCM slurry flow in microchannels numerically [36,39–41]. In all of those models, it was predominantly assumed that the latent heat of MEPCM as a step or triangle or sine function of MEPCM temperature (e.g. [39,42]). Sabbah et al. [37] incorporated the measured values of specific heat from the Differential Scanning Calorimetry (DSC) curve into the numerical simulation of a laminar minichannel flow which ensured more accurate values for the latent heat of the MEPCM. They showed that the presence of MEPCM in the working fluid slows the growth of the thermal boundary layer and extends the thermal entry length in the channel under the operating conditions considered. In addition, the dependency of the local heat transfer coefficient to the PCMs melting zone was quantified under various operating conditions.

This study is a follow-up of the work by Sabbah et al. [37] via extending the applicability of using PCM to micro-scale heat-exchangers by incorporating multi-component MEPCM slurry as opposed to single MEPCM slurry. Due to the small scale of the tube, the viscous dissipation is included in the mathematical model of this study. The results presented in this paper compare the enhancement of heat transfer of PCM slurry flows to the case of using pure liquid phase water as the working fluid in a forced convection micro-size tube with constant surface heat flux. Furthermore, this study illustrates the thermal characteristics of blend of MEPCMs slurry and its distinction from the single component MEPCM slurry flow. Introducing a blend of MEPCM with different melting

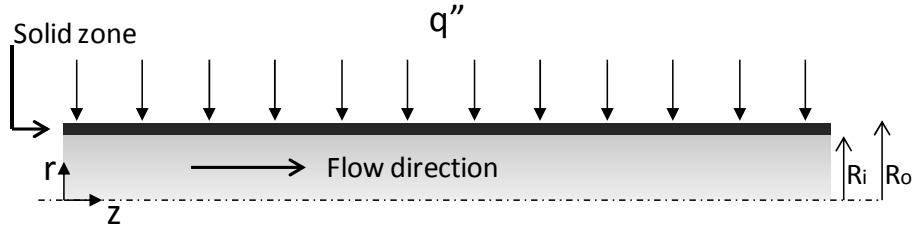


Figure 3.1: Schematic of 2-D representation of axisymmetric numerical domain.

temperature ranges could potentially expand the operability range of the MEPCM slurry under certain operating conditions. Finally, the effect of particles encapsulation as well as the shift in their melting temperature range is investigated in this paper.

3.3 Theory

Figure 3.1 shows the 2D representation of the axi-symmetric numerical domain. The MEPCM-water slurry, which contains micro-sized particles, enters the tube at a specified concentration, temperature, and velocity. The slurry temperature increases as it moves through the tube and reaches the melting temperature of the PCM. When the PCM melts inside the capsules, the melted PCM remains contained inside the capsules and does not mix with the carrier fluid. The carrier fluid exhibits lower temperature rise when PCM melts. The governing equations and assumptions in the numerical model are adapted from the work by Sabbah et al. [37] with the exception of the viscous dissipation effects which were neglected in their model but is considered for the current study because of its importance in microscales. In addition, the slurry properties formulations are revised to accommodate for the multi-component (blend) of PCMs in the slurry. The actual melting curves used for the latent heat of MEPCM particles are obtained from the differential scanning calorimeter (DSC) of Sinha-Ray et al. [2].

The basic approach consists of solving the standard steady state dimensionless continuity, Navier-Stokes and energy equations with variable fluid properties for the Newto-

Table 3.1: Summary of dimensionless hydrodynamic and energy boundary conditions.

	Inlet (z=0)	Outlet (z=L/2R _i)	Axis (r=0)	Tube inner walls (r=1/2)	Tube outer walls (r=R _o /2R _i)
Hydrodynamic	$u_r = 0$ $u_z = 1$	$P = 0$ $\partial_z u_z = 0$	$u_r = 0$ $\partial_r u_z = 0$	$u_r = 0$ $u_z = 0$	-
Energy	$\theta = 0$	$\partial_z \theta = 0$	$\partial_r \theta = 0$	$\theta = \theta_s$ $\partial_r \theta_s = f_s \partial_r \theta$	$\partial_r \theta_s = f_s$

nian fluid zone

$$\nabla \cdot \mathbf{u} = 0 \quad (3.1)$$

$$\mathbf{u} \cdot \nabla(\mathbf{u}) = -\nabla P + \frac{1}{\text{Re}_{\text{eff}}} \nabla^2 \mathbf{u} \quad (3.2)$$

$$\mathbf{u} \cdot \nabla \theta = \frac{1}{\text{Pr}_{\text{eff}} \text{Re}_{\text{eff}}} \nabla^2 \theta + \Psi_{\text{vis}} \quad (3.3)$$

and solving heat conduction equation for the solid zone,

$$\nabla^2 \theta_s = 0 \quad (3.4)$$

where $2R_i$, u_{in} , $\rho_{\text{eff}} u_{\text{in}}^2$ are the normalization factors for length, velocity, \mathbf{u} , and pressure, P respectively. The dimensionless temperature, θ , is defined as follows,

$$\theta = \frac{T - T_{\text{in}}}{q''(2R_i)/k_b} \quad (3.5)$$

In addition, the effective Reynolds number, Re_{eff} , and effective Prandtl number, Pr_{eff} are defined as,

$$\text{Re}_{\text{eff}} = \frac{\rho_{\text{eff}} u_{\text{in}} (2R_i)}{\mu_{\text{eff}}}, \quad \text{Pr}_{\text{eff}} = \frac{\mu_{\text{eff}} c_{p,\text{eff}}}{k_b} \quad (3.6)$$

The boundary conditions are summarized in Table 3.1. Note that an adiabatic thermal boundary condition ($\mathbf{n} \cdot \nabla \theta = 0$) is applied at the inlet and outlet edges of the solid zone.

Table 3.2: Physical properties of PCM and he PMMA materials [6].

Material	ρ (kg/m ³)	c_p (J/kgK)	k (W/m K)
PMMA	1190	1470	0.21
PCM 1, PCM 2	870 (solid) – 750 (liquid)	DSC curve	0.20

MEPCM Slurry Properties

The MEPCM properties are calculated from the volume fraction occupied by the PCM material and the shell as follows,

$$\chi = \frac{V_{\text{core}}}{V_p} = \frac{d_{\text{core}}^3}{d_p^3} \quad (3.7)$$

$$\Phi = \frac{\chi \rho_{\text{core}}}{\chi \rho_{\text{core}} + (1 - \chi) \rho_{\text{shell}}} \quad (3.8)$$

$$\rho_p = \chi \rho_{\text{core}} + (1 - \chi) \rho_{\text{shell}} \quad (3.9)$$

$$c_p = \Phi c_{p,\text{core}} + (1 - \Phi) c_{p,\text{shell}} \quad (3.10)$$

$$\frac{1}{k_p d_p} = \frac{1}{k_{\text{core}} d_{\text{core}}} + \frac{d_p - d_{\text{core}}}{k_{\text{shell}} d_p d_{\text{core}}} \quad (3.11)$$

The thermal conductivity of the MEPCM particle given in the last equation is calculated based on the composite sphere approach [31, 43], where d_{core}/d_p is assumed to be 85% in this work. The encapsulated MEPCM comprises of wax material that is encapsulated inside Polymethyl methacrylate (PMMA) shell [6]. The MEPCM specific heat data are adopted from DSC test reported in [2] where the sample rate of data collection was $5^\circ\text{C}/\text{min}$. Since the density and thermal conductivity values for PCM were not available from [2], they are given based on the values reported in [6] as given in Table 3.2. Figure 3.2 shows the c_p values of MEPCM particles for the two PCMs considered in this work. It can be seen that there is an approximately 10°C temperature shift between the two PCMs melting zones. The slurry's properties are calculated using the superposition of individual particles and carrier fluid properties. For N component blend slurry,

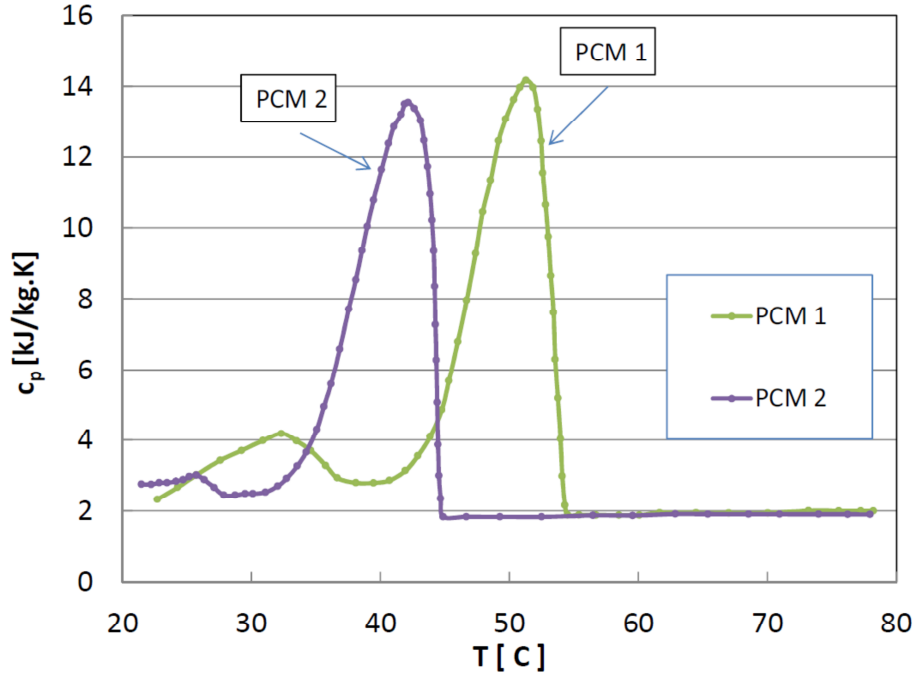


Figure 3.2: Variation of specific heat with temperature for encapsulated PCM1 and PCM2 derived from the heat-flow measurements of Sinha-Ray et [2].

the individual particle mass fraction and the slurry's effective properties are calculated as follows,

$$\phi_i = \frac{\zeta_i \rho_{p,i}}{(1 - \zeta_i) \rho_{water} + \zeta_i \rho_{p,i}} \quad (3.12)$$

$$\rho_{eff} = \sum_{i=1}^N \zeta_i \rho_{p,i} + \left(1 - \sum_{i=1}^N \zeta_i\right) \rho_{water} \quad (3.13)$$

$$c_{eff} = \phi_i c_{p,i} + (1 - \phi_i) c_{p,water} \quad (3.14)$$

$$k_b = k_w \frac{2 \left(1 - \sum_{i=1}^N \zeta_i\right) + \frac{\sum_{i=1}^N \zeta_i k_{p,i}}{k_w} \left[\frac{1}{\sum_{i=1}^N \zeta_i} + 2\right]}{2 \left(1 + \sum_{i=1}^N \zeta_i\right) + \frac{\sum_{i=1}^N \zeta_i k_{p,i}}{k_w} \left[\frac{1}{\sum_{i=1}^N \zeta_i} - 1\right]} \quad (3.15)$$

$$\mu_{eff} = \mu_{water} \left(1 - \sum_{i=1}^N \zeta_i - 1.16 \sum_{i=1}^N \zeta_i^2\right)^{-2.5}, \quad \sum_{i=1}^N \zeta_i \leq 0.37 \quad (3.16)$$

where the formulations for bulk thermal conductivity and viscosity are derived by extending the models developed by [44] and [45], respectively, for single component slurry. Note

that Eq. 3.15 is valid for a stationary multi component slurry. Water conductivity is fitted to a second degree temperature polynomial. Due to the lower particles thermal conductivity, the static thermal conductivity is lower than that of pure water for higher MEPCM concentration. However, the slurry of particles suspended in liquid generates micromixing under shear rate. The micromixing (i.e., microconvection) is a result of particle-particle, particle-liquid, and particle-wall interactions. These interactions increase the effective thermal conductivity of the slurry under motion. The experimental and theoretical studies have been conducted to evaluate the effective thermal conductivity of a single component slurry at motion [46,47]. The effective thermal conductivity of the multi-component slurry flow is specified by the following correlation,

$$k_{\text{eff}} = k_b \left(1 + B \sum_{i=1}^N \zeta_i Pe_{p,i}^m \right), \quad Pe_p = \frac{\mathbf{e}d_p^2}{\alpha} \quad (3.17)$$

where the coefficient B and the exponent m are empirically defined,

$$\begin{aligned} B &= 3, \quad m = 1.5 & Pe_p < 0.67 \\ B &= 1.8, \quad m = 0.18 & 0.67 \leq Pe_p \leq 250 \\ B &= 3, \quad m = 0.091 & Pe_p > 250 \end{aligned} \quad (3.18)$$

The effective thermal conductivity correlation, given above, shows that the thermal conductivity is strongly dependent on the particles diameter as well as the shear stress,

$$\mathbf{e} = \frac{\partial u}{\partial y} + \frac{\partial v}{\partial x}.$$

The working fluid in this study is water with the following temperature dependent

properties [48]:

$$\rho_w = 0.002630252T^2 + 1.24115T + 861.6624 \quad (3.19)$$

$$c_{p,w} = 8.732238e^{-5}T^2 + 0.09657741T^2 - 34.71345T + 8255.769 \quad (3.20)$$

$$k_w = 9.455182e^{-6}T^2 + 0.007289006T - 0.7245947 \quad (3.21)$$

The resultant specific heat, $c_{p,\text{eff}}$, for the slurry with 15% total concentration of the single-component and blend PCM is presented in Fig. 3.3. The lower concentration of individual PCM particles for the case of the blend implies that the peak in the c_p curve occurs at lower values compared to the case of the single-PCM with similar total concentration. This could potentially hinder the potential enhancement of thermal performance in the region where the flow temperature is within the melting range of the PCM particles. However, the c_p curve also suggests that the effective melting region could be expanded by using the blend of different PCM particles.

3.4 Results and Discussions

The governing equations are solved using finite volume SIMPLE algorithm. FLUENT V12 [49] is selected as the primary CFD platform. The MEPCM physical properties are modified using a user defined function (UDF). The UDF reads the temperature and the axial velocity gradient in every element from FLUENT and then calculates the MEPCM physical properties and returns their values to FLUENT. The modified slurry physical properties calculated by the UDF are updated at every iteration. The velocity and energy equations are discretized using second-order upwind scheme and the pressure using standard discretization method. A convergence criterion of 10^{-7} is used for the governing equations. The equations are solved with grid independent mesh. The results presented

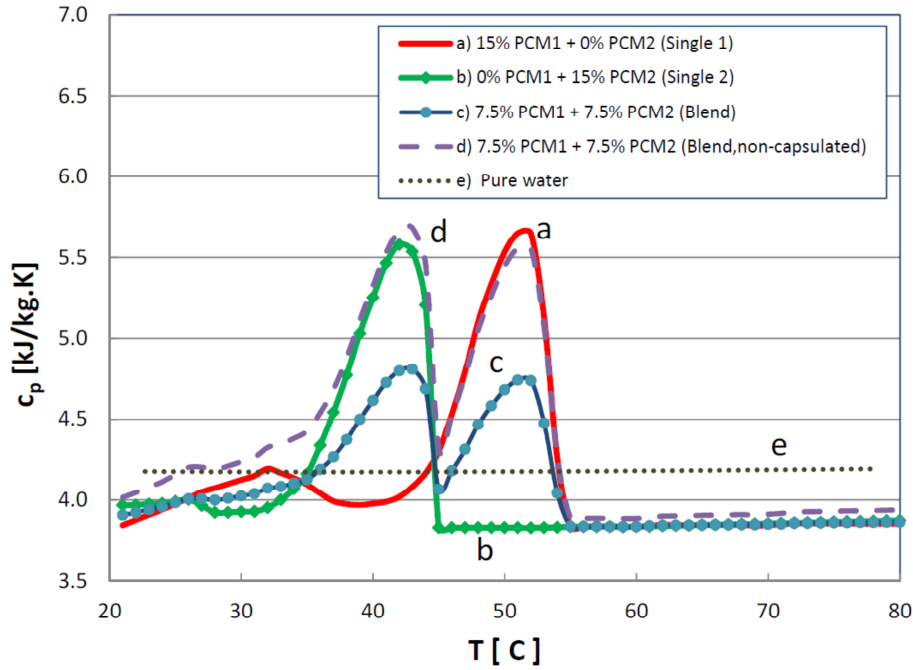


Figure 3.3: Variation of slurries effective specific heat with temperature for the case of single component and blend PCM.

Table 3.3: Summary of operating conditions.

Fluid type	\dot{V} (mm ³ /s)	q'' (W/m ²)	T_{in} (C)	ξ %	d_p (μ m)	R_i (μ m)
Pure water	16.7	9946	24	0	-	215
Slurry with single PCM1	16.7	9946	24	15	1, 5, 10	215
Slurry with two-component PCMs	16.7	9946	24	7.5+7.5	1, 5, 10	215

in this section correspond to the micro-tube shown in Fig. 3.1 under constant heat flux applied at the outer wall. The heat-flux of $9,946W/m^2$ results in total heating rate of $20W$ and the temperature of the slurry at the inlet is $24^\circ C$. These conditions have been chosen to make sure that both PCM-1 and PCM-2 will undergo phase change process. The summary of operating conditions is provided in Table 3.3.

The local heat transfer coefficient over the tube length is presented in Fig.3.4 for two Single component encapsulated PCM slurries (i.e. S1 and S2) as well as Blend of

encapsulated PCMs slurry for different PCM particle diameters, d_p . Also included in Fig. 3.4 is the calculated heat transfer coefficient for pure water as the working fluid. The terms S1 and S2 are referred to the encapsulated PCM-1 and PCM-2, respectively, whose c_p curves are provided in Fig. 3.2. The blend PCM is referred to a combination of PCM-1 and PCM-2 with identical concentration. The c_p values for the single and two-component slurry (blend) are depicted in Fig. 3.3. The local heat transfer coefficient is defined based on the local wall temperature and fluid mean temperature as follows:

$$h = \frac{q''}{T_{wall} - T_m} \quad (3.22)$$

where T_m is the slurry fluid mean temperature,

$$T_m = \frac{\int_0^{R_i} \rho_{\text{eff}} u_z c_{p,\text{eff}} r T dr}{\int_0^{R_i} \rho_{\text{eff}} u_z c_{p,\text{eff}} r dr} \quad (3.23)$$

As shown in Fig. 3.4, for $d_p \geq 10\mu m$, the local heat transfer coefficients of all three slurries prevail the water flows counterpart for the entire tube length. Given the strong dependency of the thermal conductivity of the slurry to the particle diameter (see Eq. 3.17), the bulk enhancement is attributed, in large part, to the enhanced thermal conductivity raised by the micro-convection of particles in the slurry. Despite a lower overall heat transfer coefficient of the slurry flow compared to that of pure water for $d_p \leq 5\mu m$, the local peaks raised by the melting process narrow the gap between the two. At $d_p = 10\mu m$, the slurry's thermal performance surpasses the one for water. Table 3.4 illustrates the qualitative impact of particle diameter on effective thermal conductivity of slurry for various flow conditions according to Eq. 3.17. The shear stress is approximated based on inlet velocity and tube diameter (i.e. $\partial u/\partial r \approx u_{\text{in}}/R_i$). It is observed that the effective thermal conductivity of the slurry remains lower than the case of water (i.e. $k_w \approx 0.6W/mK$) for $d_p = 1\mu m$ and $5\mu m$, leading to a diminished heat transfer performance

Table 3.4: Quantitative impact of particle diameter on slurry's thermal conductivity.

\dot{V} (mm ³ /s)	d_p (μm)	Pe_p	k_{eff} (W/mK)
16.7	1	0.0696	0.5082
16.7	5	1.7390	0.7026
16.7	10	6.9561	0.7593

of the slurry flow for this diameter range.

The local enhancements, however, are the result of augmented heat-capacity as the particles undergo the phase change process along the channel. It will be shown later that as the particle diameter shrinks, the bulk enhancement diminishes resulting in lower overall heat transfer coefficient throughout the tube. The net enhancement in average heat transfer coefficient, \bar{h} , as a function of particle diameter, d_p is presented in Fig. 3.5 which shows that while for smaller particle diameters, the slurry flow suffers from a lower effective thermal conductivity associated with the presence of MEPCM particles, the enhancement of $\geq 25\%$ is achieved for same operating conditions when larger particles are used.

In addition to the bulk enhancement provoked by enhanced effective conductivity, there is slight enhancement of heat transfer performance of blend slurry compared to the S1 slurry around $0.25 < z/l < 0.6$ which is due to the peak in c_p curve, raised by the presence of PCM-2 over lower temperature range (see Fig. 3.3). The enhancement, however, is followed by a dip in thermal performance of blend PCM around $0.6 < z/l < 0.9$. The degradation is, in large part, due to the lower peak of c_p at this temperature range compared to the S1 component PCM-1 as the concentration of each PCM is halved for the case of blend slurry.

The comparison of thermal characteristics of the blend slurry and S2 slurry is presented in Fig. 3.6 which helps in a better understanding of the physics associated with

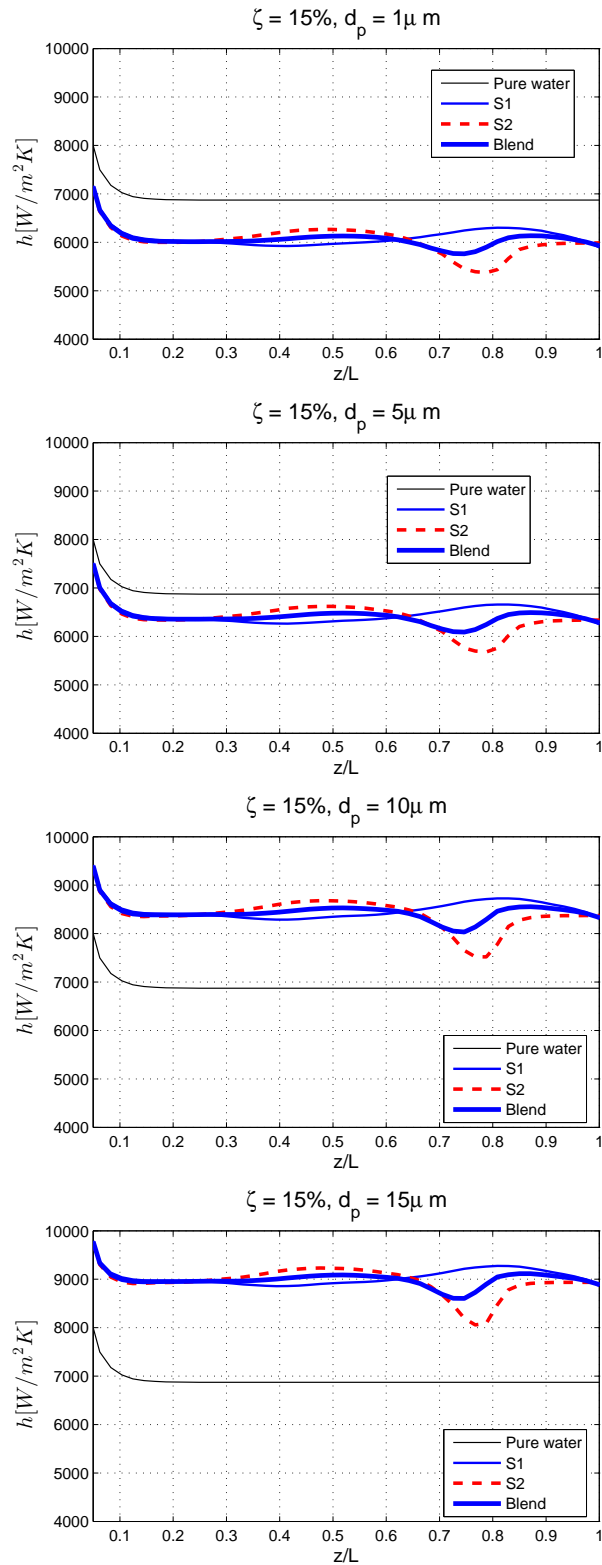


Figure 3.4: Local heat transfer coefficient for MEPCM slurries of different types and different particle diameters. The heat transfer coefficient for pure-water is also presented for comparison.

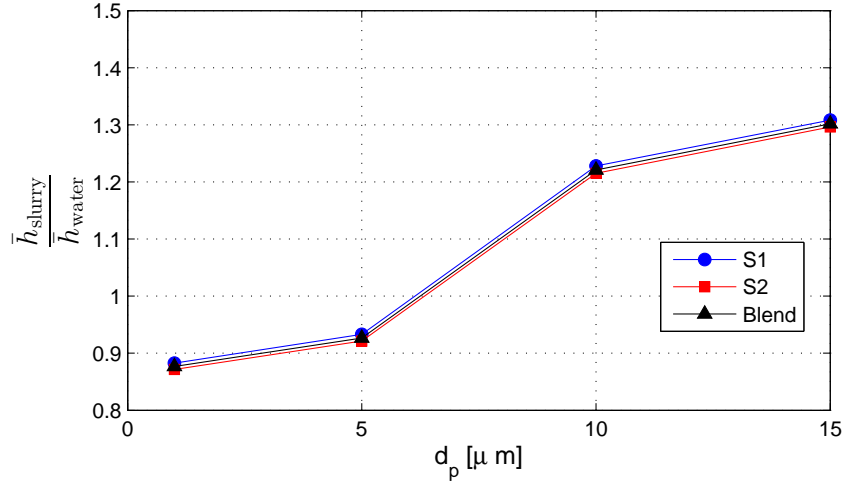


Figure 3.5: The net enhancement in average heat transfer coefficient as a function of particle diameter for different slurries.

these slurry flows. Specifically, the heat transfer coefficient along the channel changes consistently with the changes of specific heat. For example, in the vicinity of $0.25 < z/l < 0.6$, the slurry with single PCM-2 reaches its highest values of c_p near the wall which results in a slow down of the rate of temperature rise at the wall, while the bulk temperature has not been raised enough to enable PCM melting within the channel. This slow down results in a reduction of temperature difference between the wall and the bulk, hence higher local heat transfer coefficients. On the other hand, as one gets closer to the area around $0.6 < z/l < 0.9$, neither of the bulk temperature or the wall temperature are around the melting zone of the PCM; the wall has passed the melting zone and the bulk is yet to reach it. Therefore the difference between the two temperatures is escalated resulting in lower values of local heat transfer. Finally, there is an augmentation in the heat transfer coefficient close to the end of the tube which is attributed to the fluid bulk temperature rise away from the wall, enabling the PCM in that area to go through phase change. Again, there will be a slight change in the rate of bulk temperature increase so the difference of wall temperature and bulk temperature will decrease. At this point and

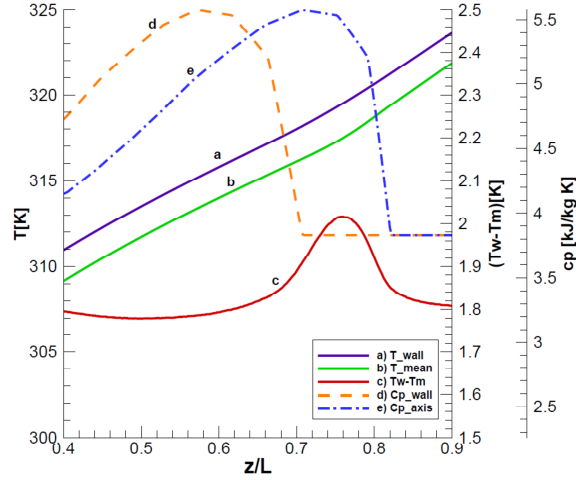


Figure 3.6: Variation of temperature, temperature difference and $c_{p,eff}$ along the tubes wall and axis for the case of encapsulated S2 slurry with $d_p = 10\mu m$.

as the PCM liquidates completely, the heat transfer coefficient for all of the cases reach the same value. Furthermore, it is observed that the variation of specific heat along the axis lags the counterpart along along the wall due to the axis lower temperature. On the other hand, the specific heat on the axis moves towards its maximum along the same path which subdues the rate of temperature increase along the axis. As the result, the temperature difference peaks where the maximum of one curve coexists with the minimum of the other; at $z/l \approx 0.75$. This explanation can be expanded in a similar fashion for behaviors observed in Fig. 3.4 for heat transfer coefficient.

The variation of local and average heat transfer coefficient with MEPCM concentration and their comparison to that of pure water is presented in Figs. 3.7 and 3.8, respectively. For all these cases, the particle diameter is maintained at $d_p = 10\mu m$. As expected, higher MEPCM concentration results in higher overall heat transfer coefficient. In addition, the blend slurry performs intermediary to either of the single-component slurries (see Fig. 3.8), though the distinction almost disappears for low MEPCM concentrations. It is worth emphasizing that the net enhancement achieved by increasing the MEPCM concentration is the net effect of favorably enhanced specific heat and thermal conductivity

against the adverse impact of the increase in liquid viscosity as one goes to higher concentration. Higher concentrations are not investigated in this work as the fluid is believed to behave non-Newtonian for $\zeta > 20\%$.

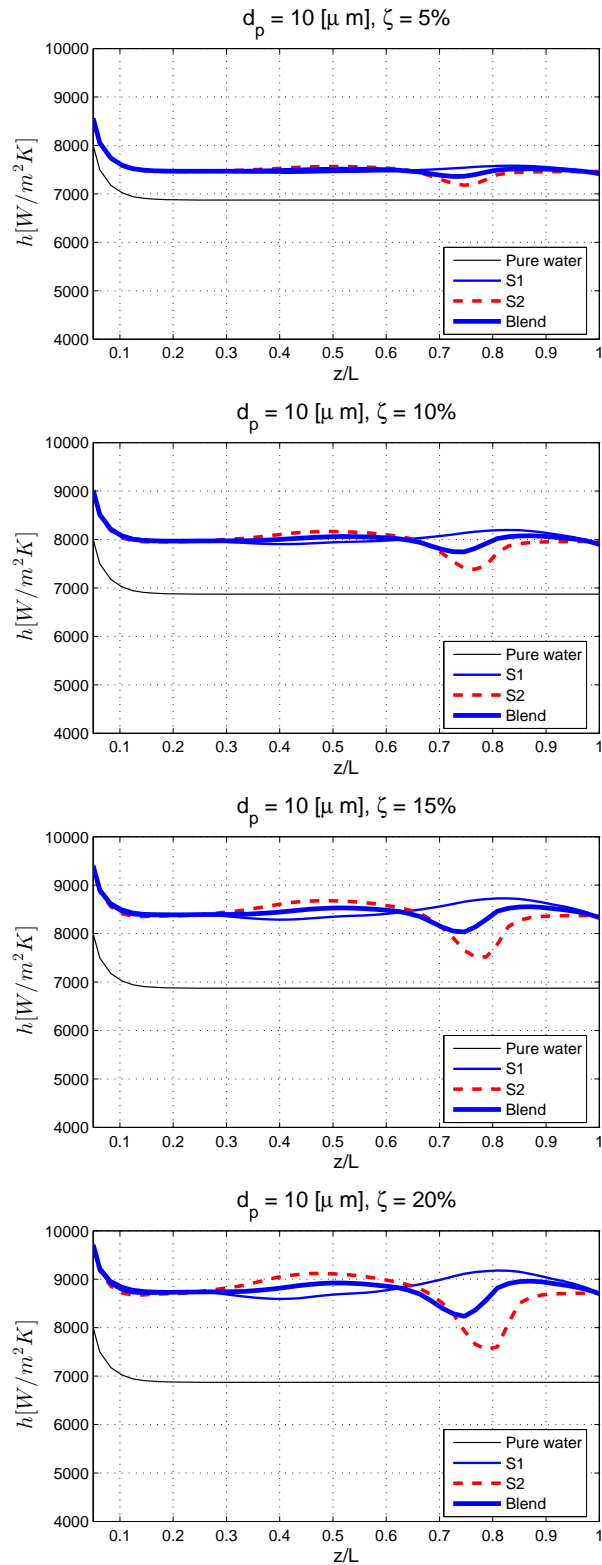


Figure 3.7: Local heat transfer coefficient for MEPCM slurries of different types and different MEPCM concentrations. The heat transfer coefficient for pure-water is also presented for comparison.

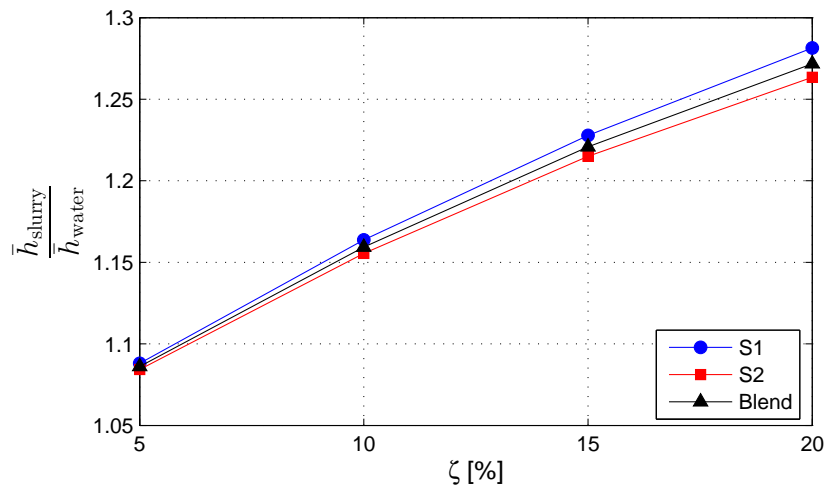


Figure 3.8: The net enhancement in average heat transfer coefficient as a function of MEPCM concentration for different slurries.

3.5 Conclusions

In this study, the fundamental governing equations for properties of a slurry containing a blend of multi-component phase change materials were introduced by extending the available equations currently used in literature for single component slurry. In addition, basic understanding of heat transfer characteristics of the slurry containing a two-component blend of PCMs vs. a single component slurry was investigated. The role of particle diameter on the effective thermal conductivity was studied as well. Moreover, it is shown that changes in the heat transfer coefficient are highly dependent on the values of the effective thermal conductivity as well as the specific heat capacity of the blend which varies according to the temperature profile of the slurry along the tube. The net enhancement in the thermal performance of the slurry flow was found to depend on the MEPCM particle diameter as well as its concentration. Furthermore, although at some locations the blend slurry showed a higher heat transfer coefficient compared to each of the single slurry cases, its overall heat transfer enhancement falls between the ones provided by either of the single-component slurry counterpart.

Chapter 4

Numerical Study of Liquid Film Flow Evaporation in the Presence of MEPCM

4.1 Objectives

This chapter numerically investigates the heat transfer characteristics of a meso-scale liquid film slurry flow containing micro encapsulated phase change material (MEPCM) in the presence of evaporation. During the evaporation process of the base fluid, the concentration of MEPCM in the slurry film increases as it flows along a heated plate, resulting in a continuous variation of its effective thermal properties. The effect of MEPCM on the evolution of the liquid film thickness under different operating conditions is presented. This study also provides an understanding towards delaying of the dry-out condition in slurry liquid film flow evaporation compared to that of the pure fluid.

4.2 Introduction

Recently, few researchers have investigated the effect of MEPCM for heat transfer enhancement of micro- and mini-channel flows using numerical techniques (e.g. [36,40,41,50]). Sabbah et al. [37] numerically studied the performance of water-based slurry in a rectangular channel and conducted a comprehensive parametric study to quantify the heat transfer enhancement obtained by MEPCM over a wide range of operating conditions. They also validated their numerical model against experimental measurements under various operating conditions [38].

Recent studies on the pure two-phase fluid flow and evaporation heat transfer in microchannels include both numerical and experimental works (see e.g. [51–54]). While finding the threshold of transition from macro-scale to micro-scale heat transfer remains one of the controversial topics in this area [52,55], there is a consensus that in contrast to microscale where nucleate boiling controls the evaporation heat transfer, macrochannel evaporation could be dominated by liquid film evaporation convection under certain operating conditions [56]. In addition to extensive experimental studies conducted to characterize the heat transfer of evaporating flows in micro- and macro-scales, there are valuable analytical works to predict these characteristics, especially under thin film evaporation regimes. In the context of numerical simulations of two-phase flows, Lakehal et al. [57] presented a very comprehensive review of the trends in the development of prediction methods for multiphase flows based on the DNS of interface dynamics and inter-phase heat and mass transfer and introduced their new boundary fitting method as a new approach for exploring the inter-phase heat and mass transfer mechanisms. Finally, there are very few publications on enhancement of heat transfer of evaporating two-phase flows with micro- and nano-particles. Zhao et al. [58] developed an analytical model and studied the effect of nanofluids on thin film evaporation in microchannels and

concluded that the nanoparticle deposited porous coating layer improves the surface wettability while significantly reducing the thin film evaporation with increasing coated layer thickness due to the thermal resistance across this layer.

To the best knowledge of the author, no previous study has numerically investigate the effect of presence of MEPCM in the carrier fluid on transport characteristics of an evaporating liquid-film flow. In the current work, the flow and heat transfer characteristics of a meso-scale slurry liquid film flow containing MEPCM in the presence of evaporation of the carrier fluid is numerically studied and the results are compared to those of the evaporation of pure liquid film flow. This study also provides an understanding towards delaying of the dry-out condition in liquid film flow evaporation by increasing the effective latent heat value of the base working fluid via the addition of MEPCM.

4.3 Theory

Figure 4.1 shows the 2D representation of the numerical domain of a meso-scale liquid film flow. The MEPCM-R134a (1,1,1,2-Tetrafluoroethane) slurry film enters the channel at a specified particle concentration with a known temperature and a known base fluid (stratified liquid/vapor fluid flow) quality. Furthermore, the fluid velocity at the both vapor and liquid phases are specified at the channel entrance. The vapor phase velocity is determined based on the entry two-phase fluid quality and the corresponding liquid film velocity. When the PCM undergoes phase change inside the capsules, the melted PCM remains contained inside the capsules and does not mix with the carrier fluid. The carrier fluid exhibits lower temperature rise when PCM melts. However, the concentration of the particles increases as the carrier fluid (R-134a) evaporates. It is also worth to mention that at the operating temperature range, the PCM does not evaporate. Moreover, the MEPCM thermal expansion effect is minimal and is neglected. Finally, the fluid is in contact with a

solid zone of finite thickness (heated from below), leading to a conjugate set of equations for heat transfer. The following additional assumptions are imposed onto the model:

1. Flow is assumed to be 2D, steady, laminar and incompressible.
2. The MEPCM-R134a slurry with spherical particles behaves Newtonian. Previous studies have shown that such behavior can be assumed for spherical particle volumetric concentrations of up to 25% [59].
3. For the particulate film flow, single-phase continuum flow model is assumed since the Stokes number, St , is below unity.
4. MEPCM particles are assumed to be uniformly distributed by the height of the liquid film.
5. The MEPCM particles do not conglomerate or settle on the channel wall.
6. The microconvection caused by the particle-particle, particle-fluid, and particle-wall interactions is lumped together, and its effect is accounted by an effective thermal conductivity.
7. Viscous dissipation is included, although with the current operating conditions it is negligible and could be ignored.
8. The liquid film remains attached to the wall.

The basic approach consists of solving the standard Navier-Stokes and energy equations with variable fluid properties for the liquid and vapor zones. These equations consist of the global continuity, momentum, and energy equations. The global continuity equation is defined as follows:

$$\nabla \cdot \mathbf{u} = 0 \quad (4.1)$$

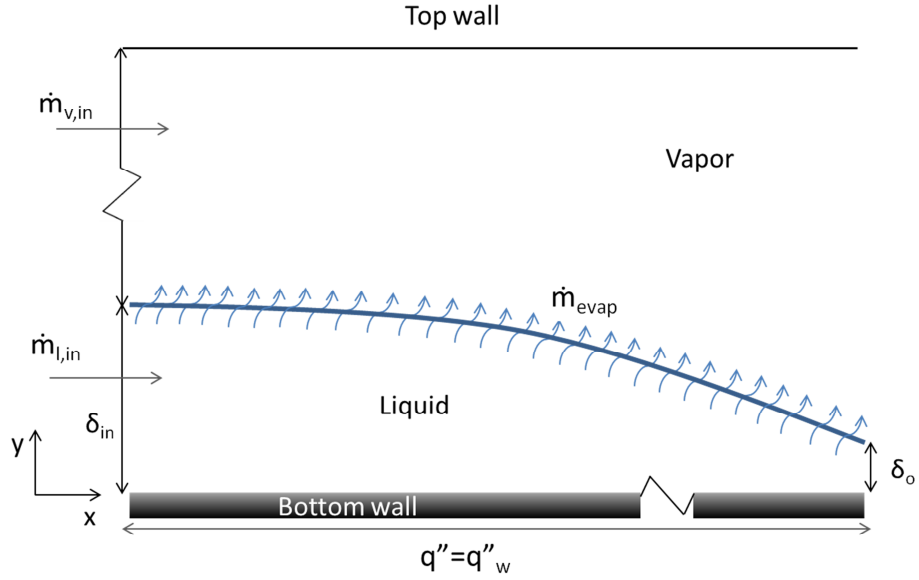


Figure 4.1: Schematic of 2-D representation of the numerical domain.(not to scale)

In the case of a stratified two-phase fluid flow, a one-fluid Volume-of-Fluid (VOF) formulation is adapted to solve for the volume fraction of vapor phase, α , and hence for the liquid phase as well through the following continuity equations,

$$\mathbf{u} \cdot \nabla \alpha \rho_v = \dot{m}_{\text{evap}} \quad (4.2)$$

$$\mathbf{u} \cdot \nabla (1 - \alpha) \rho_l = -\dot{m}_{\text{evap}} \quad (4.3)$$

where $\alpha = 1$ indicates that the given computational cell is full of vapor and $0 < \alpha < 1$ represents the interface between the liquid and vapor phases. Based on the local value of α , the corresponding fluid properties and variables will be assigned to each control volume within the domain:

$$\rho_m = \alpha \rho_v + (1 - \alpha) \rho_{l,\text{eff}} \quad (4.4)$$

$$\mu_m = \alpha \mu_v + (1 - \alpha) \mu_{l,\text{eff}} \quad (4.5)$$

$$k_m = \alpha k_v + (1 - \alpha) k_{l,\text{eff}} \quad (4.6)$$

where the subscript m stands for the properties of the liquid-vapor mixture. Note that the effective liquid slurry properties, referred by the subscript l, eff will be explained in the next section.

The mass source term in the continuity equations (4.2) and (4.3), \dot{m}_{evap} , is the mass transferred from liquid phase to the vapor phase through the evaporation process and can be obtained as follows:

$$\dot{m}_{\text{evap}} = \frac{-q''_{\text{int}} \hat{n} \cdot \nabla \alpha}{h_{fg} |\nabla \alpha|} \quad (4.7)$$

where h_{fg} is the latent heat of evaporation for the carrier fluid at the corresponding saturation temperature and q''_{int} is the net heat transfer across liquid-vapor interface. As a first order approximation,

$$q''_{\text{int}} \hat{n} = -k_m \nabla T \quad (4.8)$$

Therefore, the mass source is defined as:

$$\dot{m}_{\text{evap}} = \frac{k_m (\nabla T \cdot \nabla \alpha)}{h_{fg} |\nabla \alpha|} \quad (4.9)$$

It should be noted that the values of h_{fg} only correspond to that of pure R134a, and not of the slurry, since the MEPCM does not contribute to evaporation. The PCM is encapsulated and furthermore, its boiling point is at a much higher temperature (≥ 643 K) at the corresponding conditions.

In the VOF model, a single set of momentum equations is shared by each phase (liquid/vapor) of the fluid, and the volume fraction of each phase is tracked throughout the domain:

$$\mathbf{u} \cdot \nabla (\rho_m \mathbf{u}) = -\nabla P + \mu_m \nabla^2 \mathbf{u} \quad (4.10)$$

where \mathbf{u} is the velocity vector and μ_m is the dynamic viscosity of the liquid/vapor mixture.

The following energy equation governs the temperature distribution of the fluid (liquid and vapor phases):

$$\rho_m c_{p,m}(\mathbf{u} \cdot \nabla T) = k_m \nabla^2 T + \Psi_{\text{vis}} + S_E \quad (4.11)$$

where T represents the temperature field inside the fluid and the second term in the right hand side represents the viscous dissipation that can be expressed in the following form:

$$\Psi_{\text{vis}} = \mu_m \left[2 \left(\left(\frac{\partial u}{\partial x} \right)^2 + \left(\frac{\partial v}{\partial y} \right)^2 \right) + \left(\frac{\partial u}{\partial y} + \frac{\partial v}{\partial x} \right)^2 \right] \quad (4.12)$$

The energy source term, S_E is defined as follows:

$$S_E = -\dot{m}_{\text{evap}} h_{fg} \quad (4.13)$$

The heated solid temperature distribution is obtained through the following equation:

$$\nabla^2 T_s = 0 \quad (4.14)$$

where T_s represents the temperature field in the solid zone. The boundary conditions are summarized in Table 4.1. At the interface between the fluid and the bottom wall as well as for the channel top wall, the no slip and no permeability conditions are imposed for the velocity field. At the channel inlet, the corresponding liquid and vapor velocities as well as the saturation temperature are prescribed (see § 4.4), while the pressure boundary condition controls the outlet condition. The boundary condition imposed at the liquid/solid interface is the result of conjugate heat-exchange at this zone and guarantees the continuity of heat-flux across the interface. Finally, a constant heat flux is applied to the exterior of the bottom wall while its two sides remain insulated.

Table 4.1: Summary of hydrodynamic and energy boundary conditions.

	Hydrodynamic	Energy
Inlet	$\mathbf{u} = (u_0, 0), u_0 = \begin{cases} u_{0l}, & y \leq \delta_{in} \\ u_{0v}, & y > \delta_{in} \end{cases}$	$T = T_{sat}$
Outlet	$P = P_{sat}$	$T_{backflow} = T_{sat}$
Bottom wall/fluid interface	$\mathbf{u} = (0, 0)$	$k_m \frac{\partial T}{\partial y} = k_s \frac{\partial T_s}{\partial y}$
Outer surface of bottom wall	-	$q'' = q_w''$
Top wall	$\mathbf{u} = (0, 0)$	$\frac{\partial T}{\partial y} = 0$
Side walls	-	$\frac{\partial T}{\partial y} = 0$

Table 4.2: Physical properties of the MEPCM core, PS shell and R134a

Material	ρ (kg/m ³)	c_p (J/kgK)	k (W/mK)
PCM	870 (solid)-750 (liquid)	DSC curve	0.200
Polystyrene (PS)	1040	1300	0.105
Pure R134a (liquid)	1159.9	1480	0.076
Pure R134a (vapor)	45.8	1117	0.015

MEPCM Slurry Properties

The MEPCM comprises of paraffin wax that is encapsulated inside Polystyrene (PS) shell. The physical properties of the PS shell, MEPCM core and R134a as the carrier fluid are provided in Table 4.2 [2, 6, 60]. Polysterene shell is compatible with R134a [61]. Also, the thermal stability of polystyrene microcapsules containing paraffin wax up to approximately 408K has been confirmed according to TGA (Thermogravimetric Analysis) and DSC analysis by [62].

The MEPCM properties are calculated from the volume fraction occupied by the PCM

material and the shell as follows,

$$\chi = \frac{V_{\text{core}}}{V_p} = \frac{d_{\text{core}}^3}{d_p^3} \quad (4.15)$$

$$\Phi = \frac{\chi \rho_{\text{core}}}{\chi \rho_{\text{core}} + (1 - \chi) \rho_{\text{shell}}} \quad (4.16)$$

$$\rho_p = \chi \rho_{\text{core}} + (1 - \chi) \rho_{\text{shell}} \quad (4.17)$$

$$c_p = \Phi c_{p,\text{core}} + (1 - \Phi) c_{p,\text{shell}} \quad (4.18)$$

$$\frac{1}{k_p d_p} = \frac{1}{k_{\text{core}} d_{\text{core}}} + \frac{d_p - d_{\text{core}}}{k_{\text{shell}} d_p d_{\text{core}}} \quad (4.19)$$

The volume fraction of PCM material in the MEPCM particle, χ , is calculated based on $d_{\text{core}}/d_p = 85\%$ where $d_p = 10\mu m$ in this work as provided in Table 4.3. The MEPCM densities as calculated by Eq. (4.17) vary between 862.0 and 935.6 kg/m^3 for the liquid and solid state of PCM, respectively, which are lower than the density of the carrier fluid (R134a). However, with the maximum percent difference of 25%, it is assumed that the MEPCM particles are buoyant in the meso-scale liquid film. It could be possible to simply assign artificial value to the MEPCM density to make it very close to the working fluid. However, our intention was to stay with the real measured values. The MEPCM specific heat data are adopted from differential scanning calorimetry (DSC) measurements reported in [2]. The MEPCM measured DSC curve is directly incorporated into the numerical simulation which ensures more accurate values for the latent heat of the MEPCM. Figure 4.2 shows the corresponding DSC data for the c_p values of MEPCM particles considered in this work. The thermal conductivity of the MEPCM particle given in Eq. (4.19) is calculated based on the composite sphere approach [31, 43].

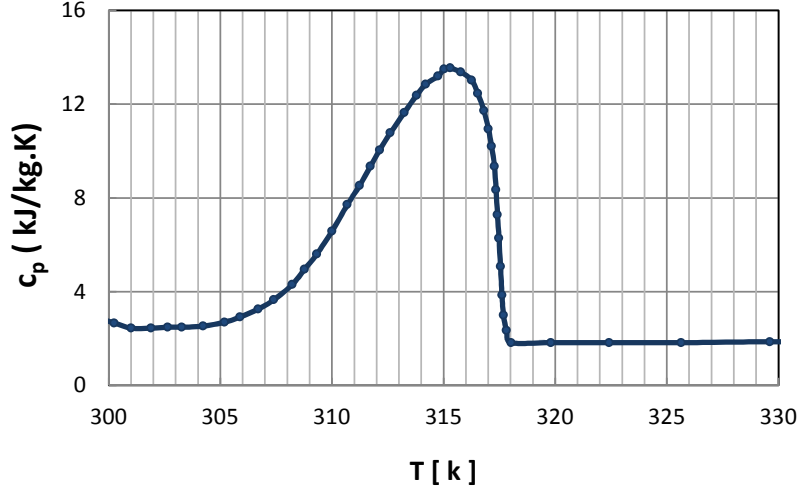


Figure 4.2: Variation of the specific heat of PCM with temperature [2].

The slurry's properties are calculated using the following equations:

$$\phi = \frac{\zeta \rho_p}{(1 - \zeta) \rho_{cf} + \zeta \rho_p} \quad (4.20)$$

$$\rho_{\text{eff}} = \zeta \rho_p + (1 - \zeta) \rho_{cf} \quad (4.21)$$

$$c_{\text{eff}} = \phi c_p + (1 - \phi) c_{cf} \quad (4.22)$$

$$k_b = k_{cf} \frac{2(1 - \zeta) + \frac{\zeta k_p}{k_{cf}} \left[\frac{1}{\zeta} + 2 \right]}{2 + \zeta + \frac{\zeta k_p}{k_{cf}} \left[\frac{1}{\zeta} - 1 \right]} \quad (4.23)$$

$$\mu_{\text{eff}} = \mu_{cf} (1 - \zeta - 1.16\zeta^2)^{-2.5} \quad (4.24)$$

where the formulations for bulk thermal conductivity and viscosity are derived by extending the models developed by [44] and [45], respectively. The micromixing (i.e., microconvection) is a result of particle-particle, particle-liquid, and particle-wall interactions. These interactions increase the effective thermal conductivity of the slurry under motion. The experimental and theoretical studies have been conducted and reported in the literature to evaluate the effective thermal conductivity at motion. The effective thermal

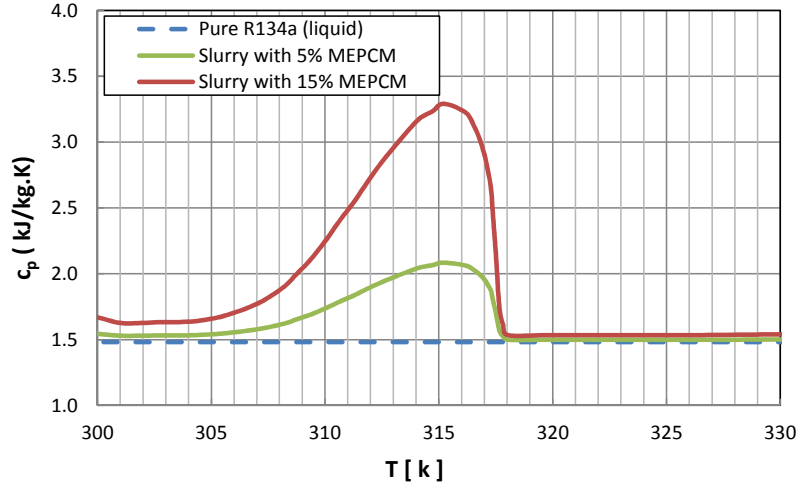


Figure 4.3: Variation of slurry's specific heat with temperature for the case of pure R134a, 5% and 15% MEPCM slurry.

conductivity of the slurry flow can be obtained by the following correlation [46,47],

$$k_{\text{eff}} = k_b (1 + \zeta B Pe_p^m), \quad Pe_p = \frac{\mathbf{e} d_p^2}{\gamma} \quad (4.25)$$

where the coefficient B and the exponent m are empirically defined as follows,

$$\begin{aligned} B &= 3, \quad m = 1.5 & Pe_p < 0.67 \\ B &= 1.8, \quad m = 0.18 & 0.67 \leq Pe_p \leq 250 \\ B &= 3, \quad m = 0.091 & Pe_p > 250 \end{aligned} \quad (4.26)$$

The effective thermal conductivity correlation, given above, shows that the thermal conductivity is strongly dependent on the particle's diameter as well as the shear stress, $\mathbf{e} = \frac{\partial u}{\partial y} + \frac{\partial v}{\partial x}$. The resultant specific heat, c_p , for the slurry with 15% volume concentration of MEPCM is presented in Fig. 4.3.

The concentration of the MEPCM particles in the slurry varies along the channel due to evaporation of the carrier fluid (R134a). This process is formulated through the

following equation:

$$\phi(x) = \frac{\dot{m}_p}{\dot{m}(x)_{cf} + \dot{m}_p} \quad (4.27)$$

where $\phi(x)$ is the local mass fraction of the MEPCM in the slurry and $\dot{m}(x)_{cf}$ is the liquid mass flow rate at any given liquid film cross section and is related to the evaporation rate through:

$$\dot{m}(x)_{cf} = \dot{m}(x - \Delta x)_{cf} - \dot{m}(x)_{evap} \quad (4.28)$$

where \dot{m}_{evap} is the evaporation mass flux as previously defined in Eq. (4.9). Finally, Δx corresponds to the size of the computational grid in the axial direction. One can obtain the MEPCM particle volumetric concentration in the slurry, $\zeta(x)$, by substituting Eq. (4.27) in Eq. (4.20).

4.4 Operating Conditions

A summary of the operating conditions is provided in Table 4.3 for the pure base fluid and the slurry. The solid bottom wall is considered to be made of a $0.0005m$ thick copper block heated from below. In all the cases presented in this section, the liquid film thickness at the inlet is maintained at $\delta_{l,in} = 0.001m$ which represents a meso-scale film height. The vapor phase thickness at the entrance is selected to be, $\delta_{v,in} = 0.015m$, to avoid interface instabilities [63]. Thus, the channel height was assumed to be $H = 0.016m$. These dimensions, along with the prescribed values of liquid mass flux, $G_{in} = 10kg/m^2.s$, and inlet vapor quality of 0.02, determine the inlet liquid velocity of $u_{l,in} = 0.043m/s$ and inlet vapor velocity of $u_{v,in} = 0.005m/s$. The inlet velocities of the liquid and vapor phases for the higher mass flux of $G_{in} = 20kg/m^2.s$ and same inlet vapor quality are $u_{l,in} = 0.086m/s$ and $u_{v,in} = 0.010m/s$, respectively.

The inlet temperature of the carrier fluid is set to be the saturation temperature which

Table 4.3: Summary of the operating conditions.

	Pure R134a	Slurry with MEPCM
T_{in} [K]	310	310
G [kg/m ² .s]	10, 20	10, 20
q'' [W/m ² .K]	200, 400, 600	200, 400, 600
ξ %	0	5, 15
d_p (μ m)	-	10

is selected to be consistent with the melting range of the MEPCM. The implication of this selection of saturation temperature is that the incoming liquid is pressurized to values beyond the atmospheric conditions (i.e., $P_{sat} = 0.93MPa$). Different wall heat fluxes of $q'' = 200, 400$ and $600W/m^2$ are considered under the same flow conditions. These values of the wall heat flux are chosen to avoid transition to boiling regime since the boiling phase-change at higher heat fluxes is beyond the scope of this paper. In addition, for a given wall heat flux, the fluid mass flux at the inlet is varied to illustrate the effect of liquid convection on liquid film thickness change and the resultant heat transfer performance. For the MEPCM slurry cases, two inlet concentrations of $\xi_{in} = 5\%$ and $\xi_{in} = 15\%$ for particle size of $d_p = 10\mu m$ are considered.

4.5 Numerical Technique

The governing equations were solved using FLUENT V14 [49] as the primary CFD platform and the VOF method was selected for solving the multiphase model. The MEPCM physical properties were modified using a user defined function (UDF). The UDF reads the temperature and the velocity gradient in every element from FLUENT and then calculates the MEPCM physical properties and returns their values to FLUENT. The modified slurry physical properties calculated by the UDF are updated at every iteration. The UDF also incorporates the essential source terms for continuity equation and energy equation

for the evaporation process and defines the variation of the MEPCM concentration in the slurry according to the evaporation rate along the interface. The interface is tracked by calculating the gradient of volume fraction of the fluid within the entire domain which returns non zero values only across the interface. The velocity and energy equations are discretized using second-order upwind scheme and the pressure using Standard discretization method. The pressure-momentum coupling is conducted through PISO method. The numerical domain consists of 57,600 quadrilateral cells with progressively increasing resolution near the wall boundaries and in the vicinity of the liquid-vapor interface. A convergence criteria of 10^{-7} is used for the momentum and energy conservation governing equations. Finally, the results presented in the following section correspond to a grid-independent solution associated with the given set of operating conditions.

4.6 Results and Discussions

The results presented in this section correspond to the evaporation of a meso-scale liquid film flow as shown in Fig. 4.1. For all the figures presented in this section, the coordinates and the liquid film thickness are normalized with respect to the thickness of the liquid film at the inlet (i.e. $x = x/\delta_{l,in}$, $y = y/\delta_{l,in}$ and $\delta = \Delta/\delta_{l,in}$). The local heat transfer coefficient is defined based on the difference in the interface temperature of the liquid film and the heated wall as,

$$h(x) = \frac{q''_w}{T_w(x) - T_{sat}} \quad (4.29)$$

The prediction of the current numerical model for the pure base fluid is validated against the classical Nusselt evaporation theory for falling liquid film [3] since no data were available for horizontal liquid film flow studied here. The theoretical model is developed for a laminar liquid film flowing over a vertical plate subject to a constant temperature that is above the saturation temperature of the incoming liquid. The Nusselt evaporation

theory for falling liquid film yields the following relation for the evolution of liquid film thickness and average heat transfer coefficient along the plate,

$$\delta(x) = \left[\frac{3\mu_l \Gamma(x)}{\rho_l(\rho_l - \rho_v)g} \right]^{1/3} \quad (4.30)$$

$$\frac{\bar{h}_x}{k_l} \left[\frac{\mu_l^2}{\rho_l(\rho_l - \rho_v)g} \right]^{1/3} = \left(\frac{4}{3} \right)^{4/3} \frac{\text{Re}_0 - \text{Re}_x}{\left(\text{Re}_0^{4/3} - \text{Re}_x^{4/3} \right)} \quad (4.31)$$

where Re_x is the local film Reynolds number based on the local liquid mass flow, $\Gamma(x)$, which can be related to the operating conditions through,

$$\text{Re}_x^{4/3} = \text{Re}_0^{4/3} - 4 \left(\frac{4}{3} \right)^{4/3} \frac{k_l (T_w - T_{\text{sat}}) x}{\mu_l^{4/3} h_{fg}} \left[\frac{\rho_l (\rho_l - \rho_v) g}{3\mu_l} \right]^{1/3} \quad (4.32)$$

Figure 4.4 shows the comparison of the numerical model prediction for local liquid film thickness and average heat transfer coefficient against the values obtained from Eqs. (4.30) and (4.31) for $T_w - T_{\text{sat}} = 5K$ and $\delta_{l,in} = 40\mu m$ which results in $\text{Re}_0 = 4\Gamma_0/\mu_l = 38.3$. In general, a good agreement is observed except for the region close to the entrance. The disparities in this region are attributed to the fact that in the Nusselt evaporation theory for falling liquid film, the inertia (i.e. convection) terms are ignored.

The role of MEPCM particles on the heat transfer characteristics of the liquid film flow evaporation is explored via comparison of temperature distribution as well as quantifying the heat transfer coefficient and liquid film thickness under the operating conditions stated in Table. 4.3. The temperature distribution as well as the variation of liquid film thickness profile along the heated plate are presented in Figs. 4.5a and 4.5b for the two cases of pure R134a and MEPCM slurry. The liquid film encounters a less pronounced variation along the heated plate for the case of slurry compared to the pure refrigerant. In addition, the temperature gradient in both stream-wise and spanwise directions is suppressed as the result of addition of MEPCM to the liquid. These observations can be explained by the

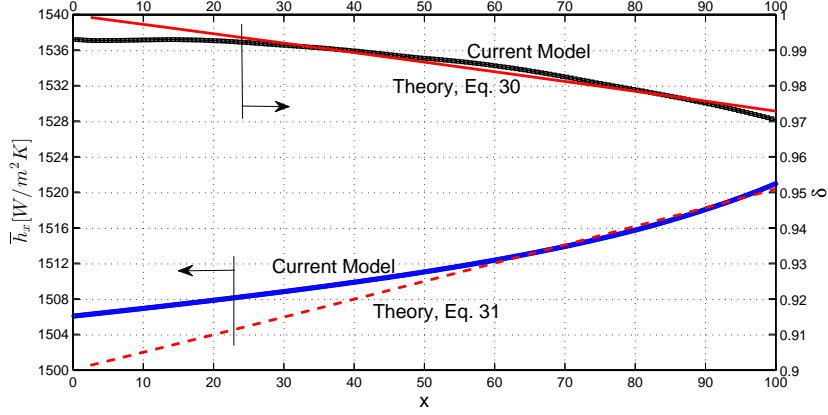


Figure 4.4: Comparison of current numerical model and Nusselt theory for falling film evaporation [3] for the evolution of liquid film thickness and local average heat transfer coefficient.

variation of liquid Peclet number which is defined as follows:

$$Pe_l = Re_l Pr_l = \frac{u_{l,in} \delta_{l,in}}{\gamma_{eff}}; \quad \gamma_{eff} = \frac{k_{eff}}{\rho_{eff} c_{eff}} \quad (4.33)$$

where γ_{eff} is the effective thermal diffusivity of the liquid phase. Figure 4.6 shows that the Pe_l associated with both slurry cases is substantially larger than the pure R134a counterpart, with a gradual increase along the channel length. The larger Pe_l value for slurry cases is primarily due to the enhanced specific heat of the liquid film ($\approx 2400 J/kg.K$ for slurry vs. $\approx 1500 J/kg.K$ for pure R-134a), although the reduction in the effective thermal conductivity (i.e. $\approx 0.060 W/m.K$ for slurry vs. $\approx 0.076 W/m.K$ for pure R-134a) is also contributing to such behavior. As the result of larger Pe_l , the convection term dominates the energy transfer in the fluid region (i.e. see Eq. (4.11)), which in turn, suppresses the temperature gradient in both stream-wise and spanwise directions as observed in Fig. 4.5b. Furthermore, the gradual increase of Pe_l along the channel is attributed to the increase in the effective specific heat of the fluid as the MEPCM particles undergo melting phase change as the result of temperature rise. It is worth noting that the

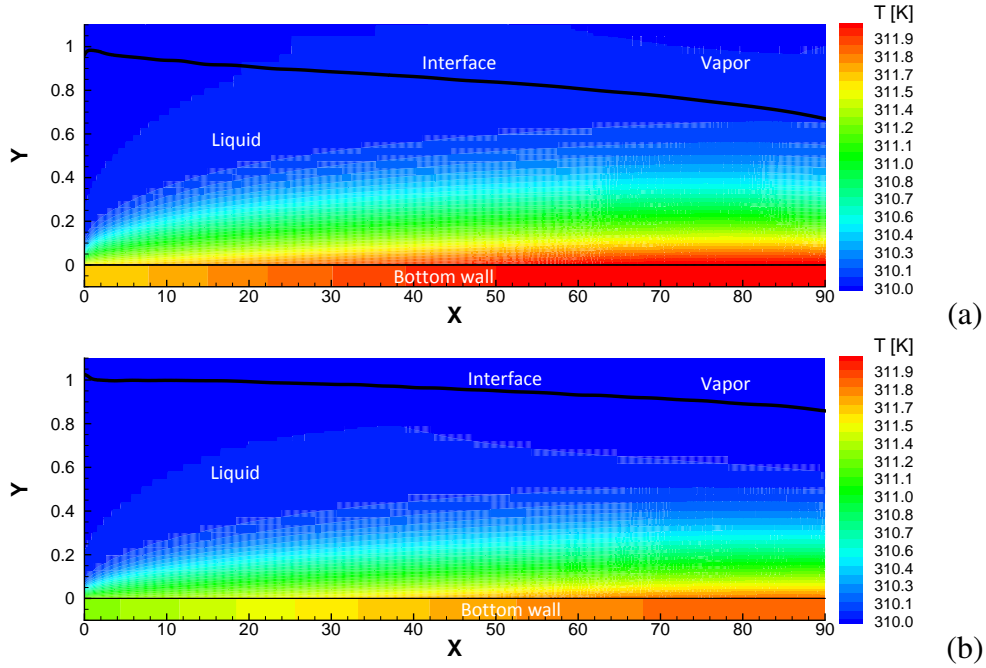


Figure 4.5: Temperature distribution and interface profile for $q_w'' = 400 \text{ W/m}^2$ and $G_{in} = 10 \text{ kg/m}^2 \cdot \text{s}$ for (a) pure R134a and (b) $\xi_{in} = 15\%$ MEPCM slurry.

rise in the value of Pe_l along the channel is due to the fact that the operating temperatures fall into the ascending part of c_p curve in Fig. 4.3. Note that the liquid-vapor phase change (hence variation in liquid film thickness) is a direct consequence of temperature difference across the liquid-vapor interface which is more prominent in the case of pure refrigerant as the result of lower Pe_l values.

Figures 4.7a and 4.7b quantify the changes in the liquid film thickness along the channel for two levels of MEPCM concentration (Fig. 4.7a) and liquid mass fluxes (Fig. 4.7b). As shown in Fig. 4.7a, compared to the case of pure R134a, the presence of MEPCM results in 15% and 20% increase in the liquid film thickness at the end of the evaporation section for $\xi_{in} = 5\%$ and $\xi_{in} = 15\%$ MEPCM inlet concentrations, respectively. The thicker liquid film at the end of the evaporation section suggests that the liquid film is less susceptible to dry-out in the presence of MEPCM for the same applied heat to the working fluid. It is observed by numerical simulation that the length of the evaporation

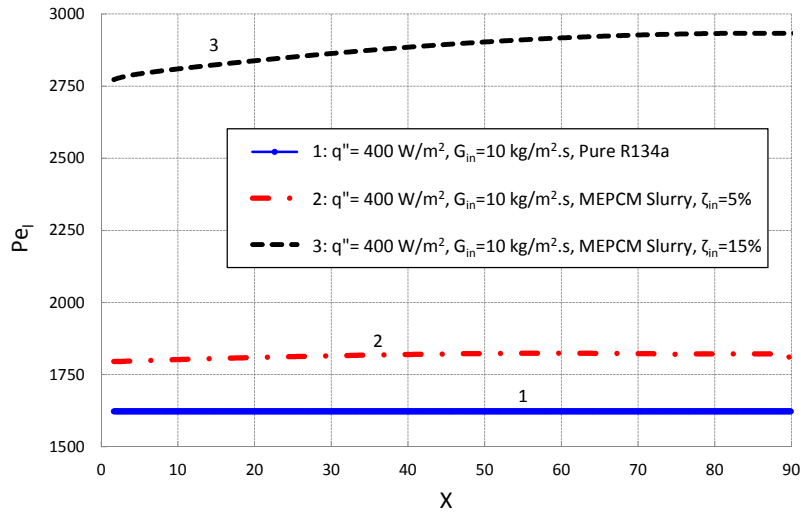
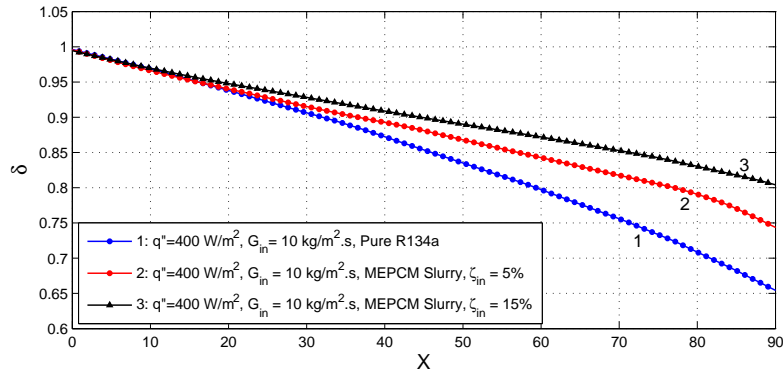
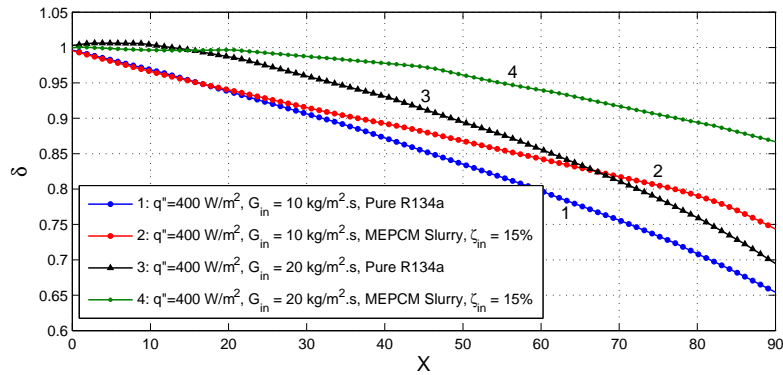


Figure 4.6: Variation of the Peclet number along the channel for $q''_w = 400 \text{ W/m}^2$.



(a)



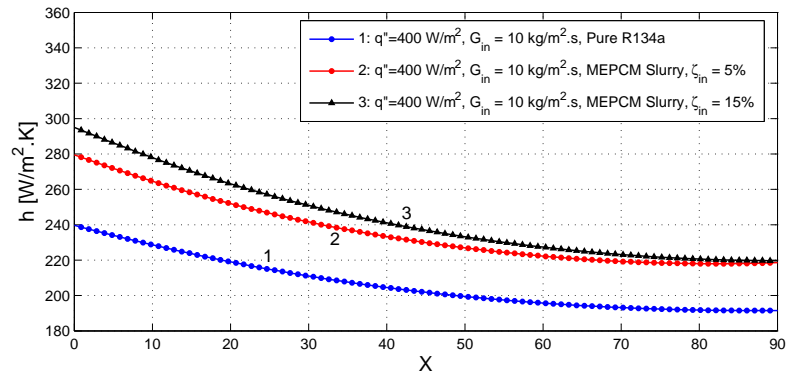
(b)

Figure 4.7: Variation of liquid film thickness along the channel for $q''_w = 400 \text{ W/m}^2$: (a) effect of MEPCM inlet concentration, ξ and (b) effect of liquid inlet mass flux, G .

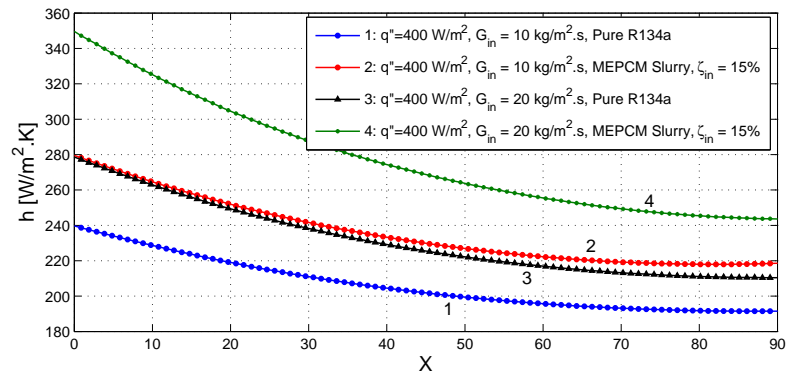
section can be extended by 29.0% and 37.5%, respectively, for $\xi_{in} = 5\%$ and $\xi_{in} = 15\%$ slurries in order to result in the same liquid film thickness as that of the pure R134a at the end of the evaporation section. As explained above, this is the direct consequence of larger Pe_1 values for MEPCM slurry compared to that of the base fluid. As the slurry flow passes along the channel, portion of the applied heat through the solid zone is stored in the MEPCM particles, resulting in a smaller temperature rise inside the liquid film. This effect is augmented along the heated surface as the effective specific heat of the liquid increases with the increase in the MEPCM concentration. While a similar trend is observed for higher liquid mass fluxes in Fig. 4.7b, the overall rate of evaporation is decreased (for same amount of applied heat flux) as the result of higher liquid film velocity and further dominance of liquid convection along the evaporation path.

The local heat transfer coefficient for MEPCM slurry is illustrated in Figs. 4.8a and 4.8b. Significant heat transfer augmentation is obtained in the case of MEPCM slurry compared to that of pure working fluid which corresponds to the smaller difference between the liquid/wall interface temperature and the fluid saturation temperature for the slurry fluid. As stated previously, the presence of MEPCM and the associated large Pe_1 result in smaller temperature rise for a given amount of heat. Moreover, both pure R134a and MEPCM slurries show a larger heat transfer coefficient at a higher inlet mass flux due to the higher convection heat transfer along the channel.

The MEPCM concentration increases up to 5% of the initial value at the outlet of the channel as illustrated in Fig. 4.9 under the corresponding operating conditions considered here. The higher wall heat flux results in a higher rate of evaporation of the base fluid and hence a higher concentration of the particles at the end of the heated wall.



(a)



(b)

Figure 4.8: Variation of evaporation heat transfer coefficient along the channel for $q''_w = 400 \text{ W/m}^2$: (a) effect of MEPCM inlet concentration, ζ and (b) effect of liquid inlet mass flux, G .

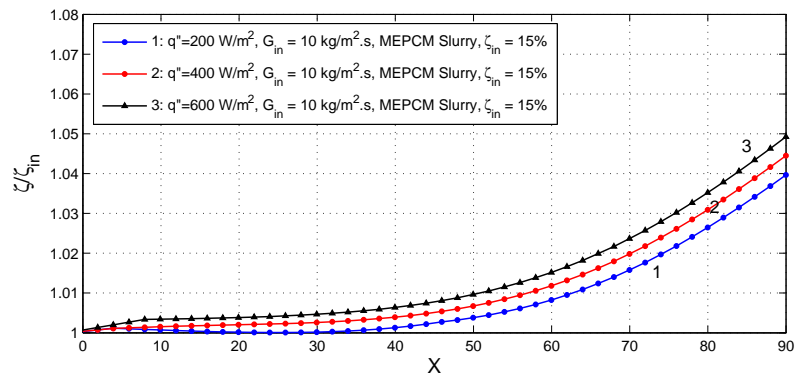


Figure 4.9: Variation of MEPCM concentration along the channel for various applied heat fluxes.

4.7 Conclusions

The heat transfer characteristics of evaporating liquid film under constant wall heat flux in the presence of MEPCM particles was numerically investigated. The formulation of thermodynamic properties of the slurry in the presence of film evaporation was presented and linked to the variation of MEPCM concentration along the channel. It was shown that the liquid film encounters a less pronounced decline of thickness in the presence of MEPCM particles compared to that of pure liquid film under similar operating conditions which is attributed to the augmented liquid Peclet number of the slurry flow. Furthermore, it was concluded that the heat transfer coefficient enhances in the presence of MEPCM particles in the slurry. A more profound effect of MEPCM phase change is expected if one operates the system at temperatures closer to the peak melting temperature of the MEPCM. In addition to an enhanced heat transfer coefficient, it was shown that one of the advantages of adding MEPCM particles is to delay the potential dry-out in liquid film evaporation regime.

Chapter 5

Natural Convection in an Enclosure with MEPCM

5.1 Objective

The present work is a numerical and experimental study to investigate the effect of using micro-encapsulated phase change materials (MEPCMs) on the heat transfer characteristics of a liquid in a rectangular enclosure driven by natural convection. A comparison has been made between pure water and the MEPCM slurry. While the natural convection flow of pure water is induced due to the mere change in the density of the liquid, the MEPCM slurry flow is due to the combination of the density change of the carrier fluid as well as the change in the density of the MEPCM particles during its melting and solidification. The numerical model is validated against experimental measurements over a range of operating conditions.

5.2 Introduction

The subject of natural convection heat transfer has been studied by many researchers over many decades. Recently, this subject has received attention particularly in the areas of heat dissipation from electronic packages and issues related to the thermal design of these devices [64]. Moreover, natural convection plays an important role in different applications such as solar collectors and chemical vapor deposition reactors [65].

In an experimental study by Inaba et al. [66], the stability of Rayleigh-Benard convection was investigated in rectangular enclosures filled with MEPCM slurry. They reported that the critical Rayleigh number decreases with the PCM mass concentration while the PCM is in phase change and the maximum Nusselt number can be reached for all of the slurries while the heating plate is controlled at a temperature that most of the PCM is in phase change process. Omari et al. [67] numerically modeled the natural convection dominated melting of a PCM inside an enclosure. They studied the effect of geometrical shape of the container and the relative location of the cold wall on the heat transfer and flow pattern. It was shown that for thin containers, the region of melting PCM shifts to the top while in wider containers, this region expands horizontally. Sabbah et al. [48] conducted a detailed numerical study on the effect of PCM on the heat transfer characteristics of a fluid in a rectangular cavity driven by natural convection. The use of multiple PCMs with different melting range in the blend slurry was introduced by [68] where they presented the governing equations for the properties of the blend slurry and showed that depending on the melting temperature range of each PCM, the blend slurry could provide locally higher heat transfer coefficient compared to each of the single slurry cases.

This work is an extension of the previous work [48]. The theoretical model is modified to account for the buoyancy driven liquid flow based on the actual temperature change as opposed to the previously adapted Boussinesq approximation. In addition, an experimen-

tal study is conducted to validate the numerical model and provide physical insight into the interaction between the MEPCM particles and the natural convection flow.

5.3 Numerical Study

5.3.1 Theory

Figure 5.1 shows the 3D representation of the numerical domain. The rectangular container has a width of $W=5$ cm, height of $H=13$ cm and length of $L=4$ cm. The governing equations and assumptions in the numerical model are adapted from the work by Sabbah et al. [48].

The following assumptions are imposed into the model:

1. Flow of water and the MEPCM slurry in the enclosure is assumed to be steady state, laminar and incompressible.
2. The MEPCM-water slurry behaves as a Newtonian fluid for MEPCM volumetric concentrations below 25% [59].
3. For the particulate flow, single-phase flow model is assumed since Stokes number St is below unity.
4. The actual density variation profile as a function of temperature is used instead of the Boussinesq approximation for density. The numerical results for case of pure water is verified against the case with Boussinesq approximation for density to assure the validity of the functions used for density variation.
5. The encapsulation shell that encompasses the PCM has enough mechanical flexibility to accommodate the volumetric thermal expansion of the phase change material.
6. The microconvection caused by the particle-particle, particle-fluid, and particle-wall interactions is lumped together, and its effect is accounted by an effective thermal conductivity.

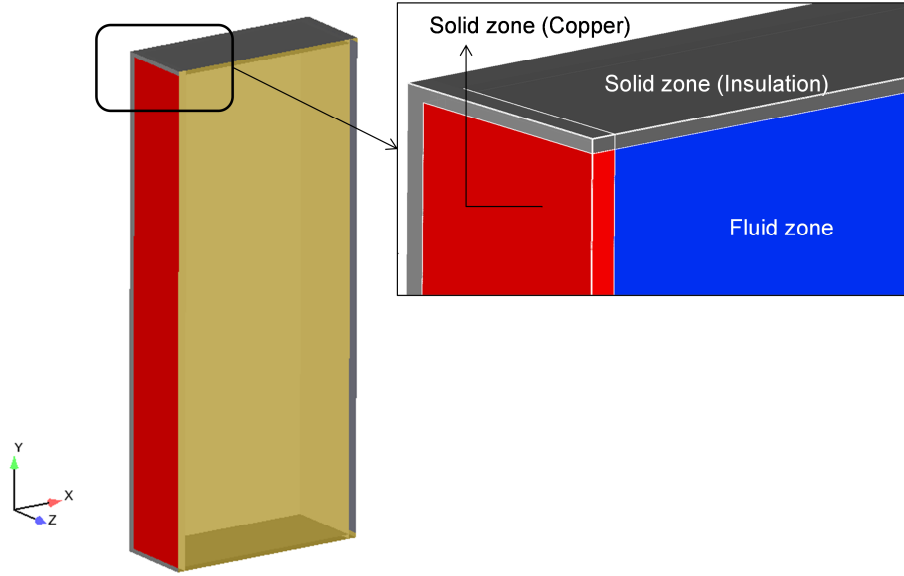


Figure 5.1: Schematic of the numerical domain and the boundary conditions.

7. The melting curve used for the latent heat of MEPCM particles is obtained from the differential scanning calorimeter (DSC) of PureTemp [4].

The numerical model consists of a conjugate set of transport equations where the energy equation is solved for both the liquid phase and for within the solid components of the enclosure wall. To that extend, the steady state non-dimensional continuity and momentum equations for the fluid with variable properties take the following form,

$$\nabla \cdot \mathbf{u} = 0 \quad (5.1)$$

$$\mathbf{u} \cdot \nabla (\rho_{\text{eff}} \mathbf{u}) = -\nabla P + \nabla^2 (\mu_{\text{eff}} \mathbf{u}) + \mathbf{g} \quad (5.2)$$

where \mathbf{u} is the velocity vector. The subscript eff stands for the effective properties of the slurry as given in the next section. The energy equation for the temperature distribution inside the fluid zone and takes the following form:

$$\mathbf{u} \cdot \nabla (\rho_{\text{eff}} c_{p,\text{eff}} T) = k_{\text{eff}} \nabla^2 T \quad (5.3)$$

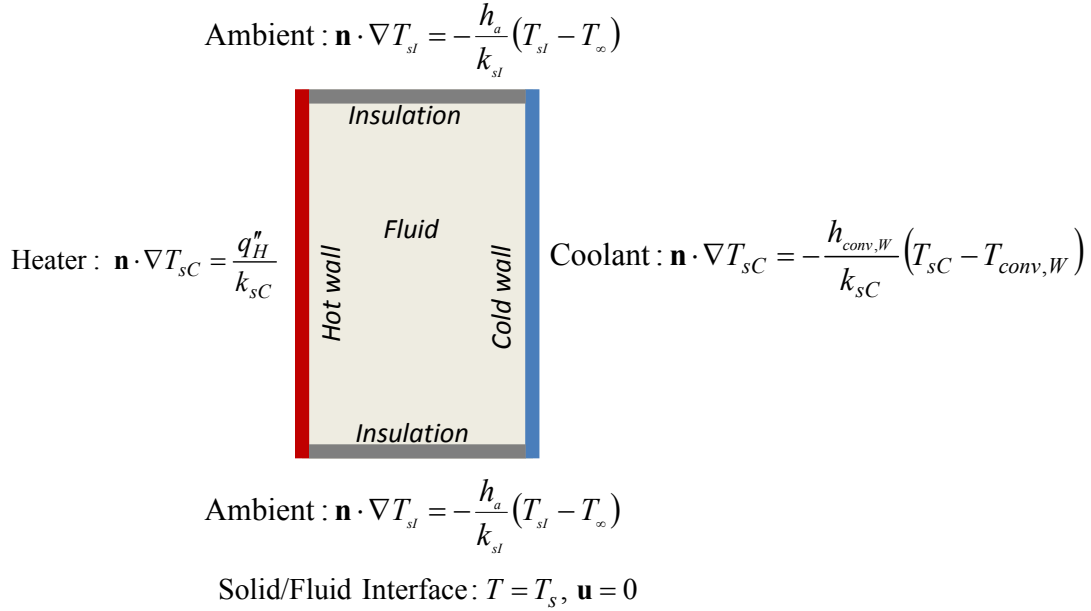


Figure 5.2: Schematic description of fluid and thermal boundary conditions for the present numerical model.

Finally, the Laplace equation governs the temperature distribution within the two solid zones components:

$$\nabla^2 T_{sC} = 0 \quad (5.4)$$

$$\nabla^2 T_{sI} = 0 \quad (5.5)$$

where T_{sC} and T_{sI} , respectively, represent the temperature field within the copper zone and the insulation zone (see Fig. 5.1). The boundary conditions are shown schematically in Fig. 5.2. Note that the insulation solid zone is exposed to the ambient air of temperature T_∞ and the convection heat transfer coefficient, h_a , approximated to be $\approx 10W/m^2K$. In addition, on the cold side, the heat exchange occurs between the cold plate and coolant liquid with heat transfer coefficient, $h_{conv,W}$, approximated through turbulent flow Nusselt number approximation for internal flow. The applied heat flux on the heated side is q'' .

5.3.2 MEPCM Slurry Properties

The MEPCM comprises of wax material that is encapsulated inside Polymethyl-methacrylate (PMMA) shell [6]. The physical properties of the PCM core and the PMMA shell are provided in Table 5.1. The MEPCM properties are calculated from the volume fraction occupied by the PCM material and the shell as follows,

$$\chi = \frac{V_{\text{core}}}{V_p} = \frac{d_{\text{core}}^3}{d_p^3} \quad (5.6)$$

$$\Phi = \frac{\chi \rho_{\text{core}}}{\chi \rho_{\text{core}} + (1 - \chi) \rho_{\text{shell}}} \quad (5.7)$$

$$\rho_p = \chi \rho_{\text{core}} + (1 - \chi) \rho_{\text{shell}} \quad (5.8)$$

$$c_p = \Phi c_{p,\text{core}} + (1 - \Phi) c_{p,\text{shell}} \quad (5.9)$$

$$\frac{1}{k_p d_p} = \frac{1}{k_{\text{core}} d_{\text{core}}} + \frac{d_p - d_{\text{core}}}{k_{\text{shell}} d_p d_{\text{core}}} \quad (5.10)$$

The volume fraction of PCM material in the MEPCM particle, χ , is calculated based on $d_{\text{core}}/d_p = 85\%$ where $d_p = 10\mu\text{m}$ in this work. The density of the PCM in the core of particles in Eq. 5.11 encompasses the volumetric changes due to temperature variation and can be written as a function of particles densities at liquid and solid states:

$$\rho_{\text{core}} = \beta \rho_l + (1 - \beta) \rho_s \quad (5.11)$$

where β is the liquid fraction of the PCM in the core of the particle, as expressed in Eq. 5.12 and ρ_l and ρ_s are the densities of the PCM at liquid and solid states, respectively.

$$\beta = \frac{\int_{T_s}^T c_{p,\text{core}} dT}{\int_{T_s}^{T_l} c_{p,\text{core}} dT} \quad (5.12)$$

The density variation of the PCM core material due to the phase change (from solid to liquid and vice versa) is incorporated into the numerical model by representing the density

Table 5.1: Physical properties of the PCM and the PMMA material

Material	ρ (kg/m ³)	c_p (J/kgK)	k (W/m K)
PMMA	1190	1470	0.21
PCM 1, PCM 2	870 (solid) – 750 (liquid)	DSC curve	0.20

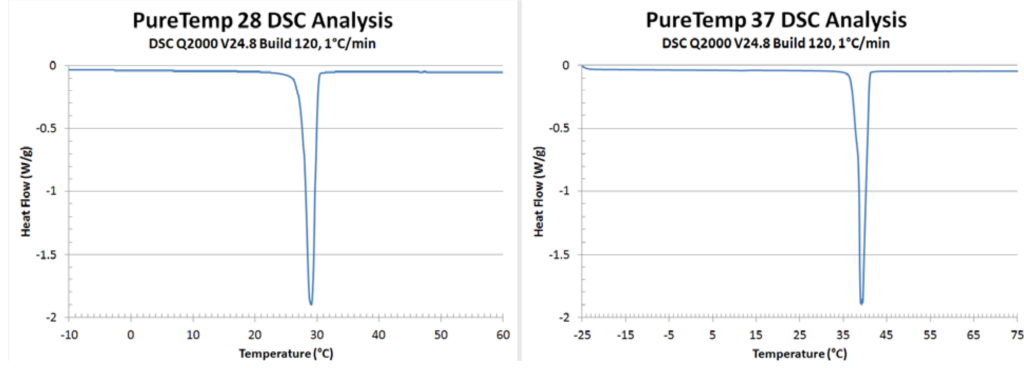


Figure 5.3: DSC curves for the MEPCM used in this study [4].

as a function of temperature. This density variation requires the corresponding change in the volume of the particle through the expansion of the PMMA shell. However, since the particle diameter is related to the power of 1/3 of the volumetric change, it is not incorporated into the model and a constant value of particle diameter is used throughout the model. As an example, for the particle size of $d_p = 10\mu m$, the maximum corresponding change in the particle diameter due to phase change is 2.5%. The MEPCM specific heat data are adopted from DSC measurements reported in [4]. Figure 5.3.2 shows the DSC curves of the PCMs considered in this work. The heat flow values on the DSC curve are proportional to the specific heat of the material. The thermal conductivity of the MEPCM particle given in the last equation is calculated based on the composite sphere approach [31, 43].

The slurry's properties are calculated using the following equations:

$$\phi = \frac{\zeta \rho_p}{(1 - \zeta) \rho_{cf} + \zeta \rho_p} \quad (5.13)$$

$$\rho_{\text{eff}} = \zeta \rho_p + (1 - \zeta) \rho_{cf} \quad (5.14)$$

$$c_{\text{eff}} = \phi c_p + (1 - \phi) c_{cf} \quad (5.15)$$

$$k_b = k_{cf} \frac{2(1 - \zeta) + \frac{\zeta k_p}{k_{cf}} \left[\frac{1}{\zeta} + 2 \right]}{2 + \zeta + \frac{\zeta k_p}{k_{cf}} \left[\frac{1}{\zeta} - 1 \right]} \quad (5.16)$$

$$\mu_{\text{eff}} = \mu_{cf} (1 - \zeta - 1.16\zeta^2)^{-2.5} \quad (5.17)$$

where the formulations for bulk thermal conductivity and viscosity are derived by extending the models developed by [44] and [45], respectively. Note that Eq. 5.16 is valid for a stationary slurry. Water conductivity is fitted to a second degree temperature polynomial. Due to the lower particles thermal conductivity, the static thermal conductivity is lower than that of pure water for higher MEPCM concentration. However, the slurry of particles suspended in liquid generates micromixing under shear rate. The micromixing (i.e., microconvection) is a result of particle-particle, particle-liquid, and particle-wall interactions. These interactions increase the effective thermal conductivity of the slurry under motion. The experimental and theoretical studies have been conducted to evaluate the effective thermal conductivity at motion. The effective thermal conductivity of the slurry flow is specified by the following correlation [46,47],

$$k_{\text{eff}} = k_b (1 + \zeta B \text{Pe}_p^m), \quad \text{Pe}_p = \frac{\mathbf{e}d_p^2}{\gamma} \quad (5.18)$$

where the coefficient B and the exponent m are empirically defined as follows,

$$\begin{aligned}
 B &= 3, \quad m = 1.5 & Pe_p < 0.67 \\
 B &= 1.8, \quad m = 0.18 & 0.67 \leq Pe_p \leq 250 \\
 B &= 3, \quad m = 0.091 & Pe_p > 250
 \end{aligned} \tag{5.19}$$

The effective thermal conductivity correlation, given above, shows that the thermal conductivity is strongly dependent on the particle's diameter as well as the shear stress, $\mathbf{e} = \frac{\partial u}{\partial y} + \frac{\partial v}{\partial x}$. It is worth noting that the span-wise component of the shear stress tensor, (i.e. associated with velocity component in z-direction, Fig. 5.1) is neglected in this expression due to the minimum contribution raised from the span-wise induced velocity field. The working fluid, water, has the following temperature dependent properties [48]:

$$\rho_w = -0.00263T^2 + 1.24115T + 861.6624 \tag{5.20}$$

$$c_{p,w} = -8.732e^{-5}T^3 + 0.097T^2 - 34.713T + 8255.769 \tag{5.21}$$

$$k_w = -9.45518e^{-6}T^2 + 0.00729T - 0.72459 \tag{5.22}$$

5.3.3 Numerical Technique

The governing equations are solved using finite volume SIMPLE algorithm. FLUENT V12 [49] is selected as the primary CFD platform. The MEPCM physical properties are modified using a user defined function (UDF). The UDF reads the temperature and the shear stress in every element from FLUENT and then calculates the MEPCM physical properties and returns their values to FLUENT. The modified slurry physical properties calculated by the UDF are updated at every iteration based on the local temperature and velocity distribution. The momentum and energy equations are discretized using second-order upwind scheme and the pressure using standard discretization method. A conver-

gence criterion of 10^{-7} is used for the governing equations. The equations are solved with grid independent mesh.

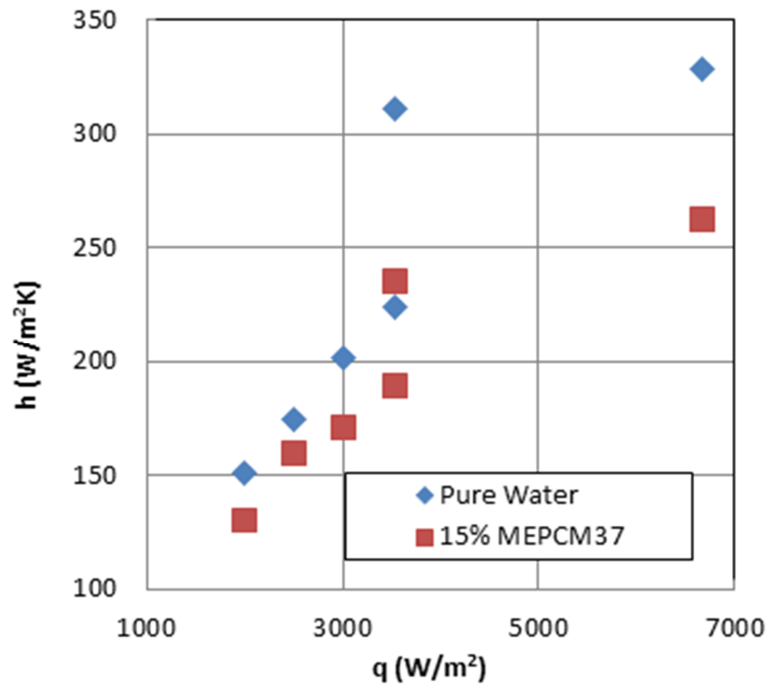
5.4 Analysis of Numerical Results

Effect of operating conditions on heat transfer performance

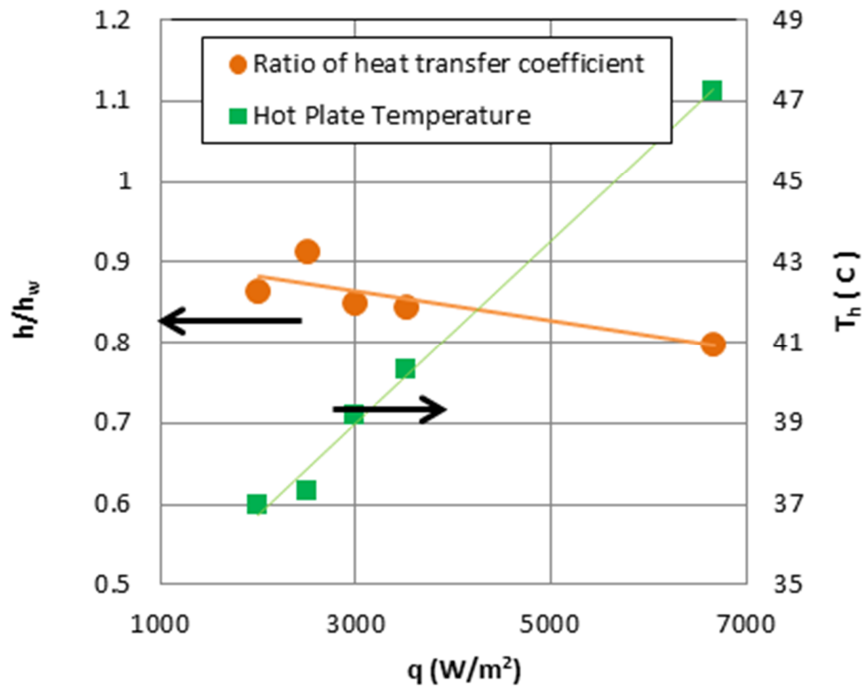
Figure 5.4a shows the comparison of the heat transfer coefficient of 15% MEPCM slurry with that of pure water for a range of applied heat flux. As can be seen, at higher applied heat fluxes, the difference is larger. This is due to the higher increase in the temperature of the hot plate and its moving away from the peak of the specific heat. This is demonstrated in Fig. 5.4b with the variation of the ratio of heat transfer coefficient and the temperature on the hot side, T_h as a function of applied heat flux. The ratio of heat transfer coefficient shows its highest value at the applied heat flux of $q'' = 2500W/m^2K$. At this point, the hot plate temperature has reached to $37^\circ C$ which is very close to the melting temperature of the MEPCM ($T_m = 38^\circ C$). After all, the heat transfer coefficient for all the slurry cases remain below that of water.

Effect of presence of MEPCM on flow field

The following figures display the contour plots of velocity magnitude and temperature of the fluid inside the enclosure. Figures 5.5a and Fig. 5.5b correspond to the velocity field for pure water and 15%MEPCM37 slurry, respectively. As can be seen in the color bar, higher velocity magnitudes are achieved in the case of pure water which is consistent with higher circulation of the fluid and hence better heat transfer coefficient compared to the MEPCM slurry. In both cases, the applied heat flux is $q'' = 6669.82W/m^2$ and the cold wall temperature is $T_c = 22^\circ C$. The heat transfer coefficient for pure water is



(a)



(b)

Figure 5.4: Variation of (a) heat transfer coefficient of pure water and slurry with applied heat flux and (b) the ratio of heat transfer coefficient of slurry flow to that of water and the corresponding hot plate temperature with applied heat flux.

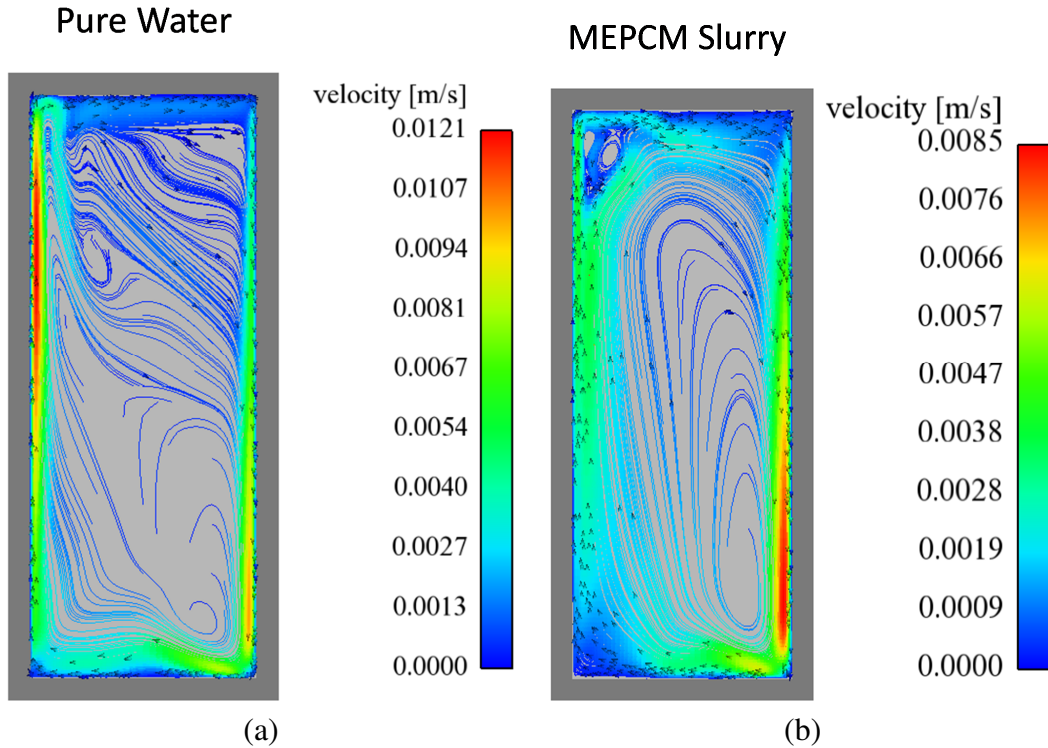


Figure 5.5: Dimensional velocity field at the symmetry plane, for (a) pure water and (b) 15% MEPCM slurry flow.

25% higher than that of MEPCM slurry. ($328.08 \text{ W/m}^2\text{K}$ compared to $261.87\text{W/m}^2\text{K}$ for slurry). The lower velocity for the MEPCM slurry case compared to that of water is attributed to the larger viscosity ($\approx 0.0017\text{Pa}\cdot\text{s}$ vs. $\approx 0.0010\text{Pa}\cdot\text{s}$ for pure water) which diminishes the overall fluid mechanics performance of the system. In addition, the very low overall velocities (and hence, $Pe < 10$) suggest that the heat transfer across the plate is occurring predominantly through conduction rather than convection associated with buoyancy driven flow. This implies that any change in the thermal conductivity of the fluid will be more deterministic to the overall heat transfer performance than the variations of specific heat and density. Considering the lower overall thermal conductivity of the MEPCM slurries ($0.5\text{W/m}\cdot\text{K}$ vs. $\approx 0.6\text{W/m}\cdot\text{K}$ for pure water), one can conclude that the lower thermal conductivity of the MEPCM slurry has an adverse impact on its heat transfer performance that prevail over any benefit associated with larger specific heat.

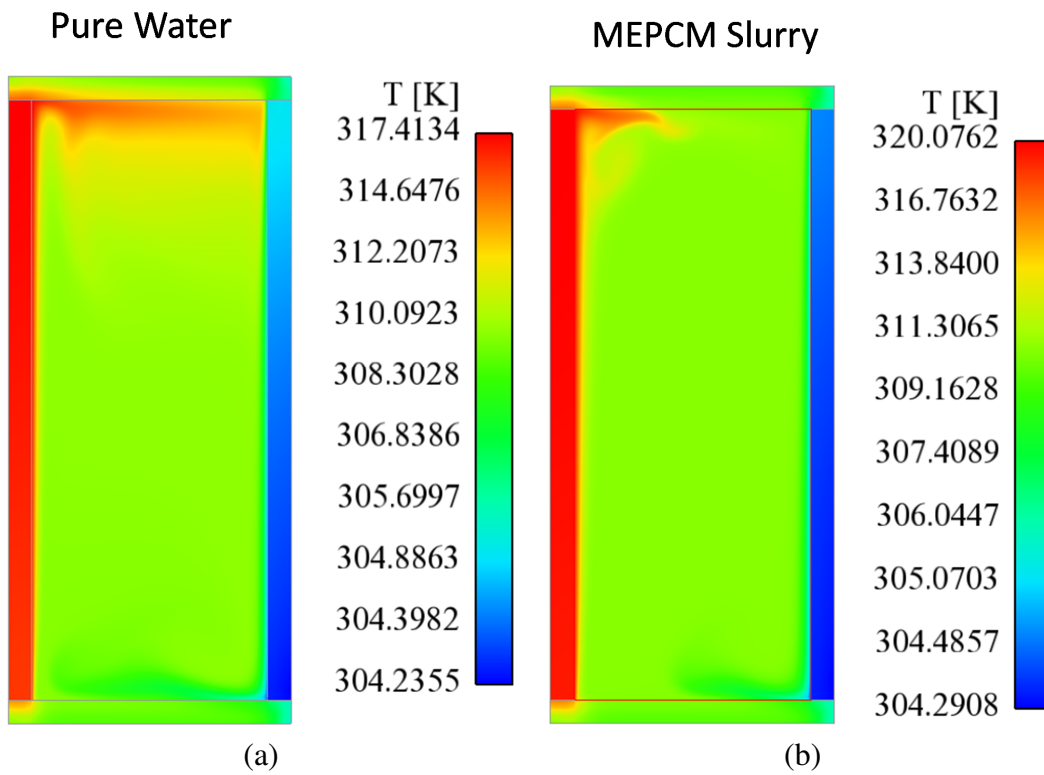


Figure 5.6: Dimensional temperature field at the symmetry plane, for (a) pure water and (b) 15% MEPCM slurry flow.

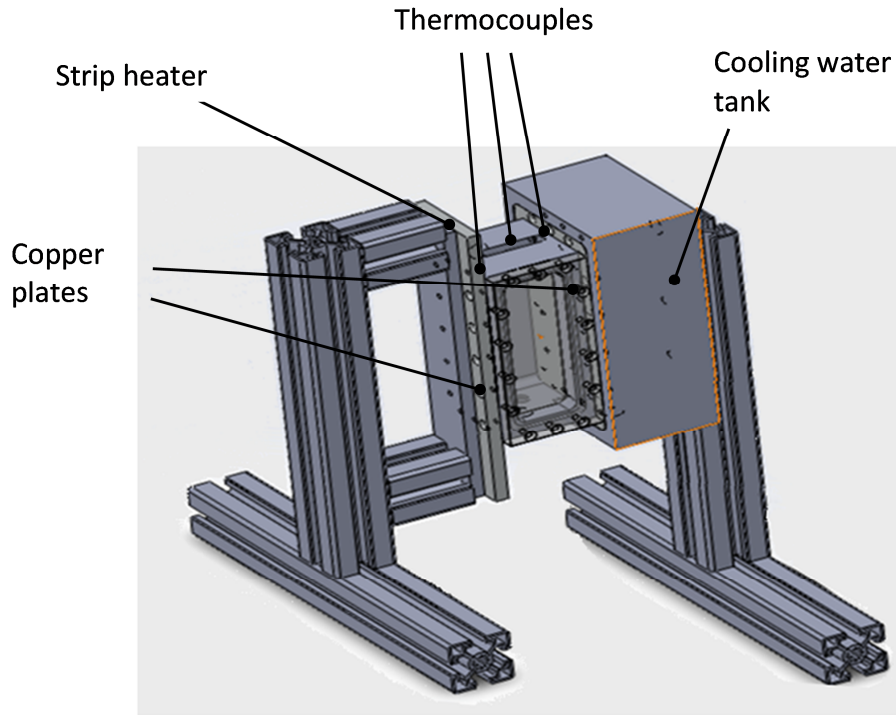


Figure 5.7: Schematic of the experimental setup.

5.5 Experimental Study

Different parts of the setup were designed in SolidWorks and built in the machine shop of the WPI-Higgins Lab. A schematic of the experimental setup is shown in Fig. 5.7. The setup includes the following parts:

The main experimental enclosure: This part is shown in the mid-section of Fig. 5.7 as well as enlarged in Fig. 5.8. The interior dimensions of this part are $0.13m \times 0.05m \times 0.04m$. This part is made of white Delrin acetal resin due to its low thermal conductivity ($k=0.23 \text{ W/mK}$) to provide insulation on the back, top and bottom sides of the enclosure. Two rectangular holes on the sides have been considered that match the location of copper side walls. On the front of the box there is an opening that allows for inserting a polycarbonate sheet window to visualize the experience. Also, on the left, right and front sides of the enclosure, grooves are machined for Buna-N O-ring cords to be

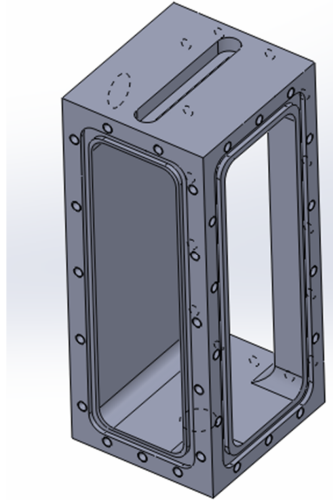


Figure 5.8: The main enclosure.

placed between the copper plates and the enclosure as well as between the polycarbonate sheet and the enclosure. This main enclosure contains the liquid under study which is either water or any of the two types of the MEPCM slurry (explained in the materials section) with different concentrations in each test. A 0.05 m wide slotted hole on the top of this part allows for the horizontal traverse of a J-type thermocouple for measuring the temperature profile of the liquid across the two side walls of the enclosure. To empty the enclosure from the test liquid at the end of each experiment, a drainage hole is made at the bottom of the enclosure.

Side walls: Two copper plates were inserted in the rectangular holes on the two sides of the main enclosure. The dimensions of these two side walls are $0.130m \times 0.038m \times 0.019m$. The side wall on the left side of the enclosure, referred to as the hot plate, is in contact with a strip heater. The right side wall, referred to as the cold plate, is adjacent to a cooling tank. A ceramic insulated strip heater (OMEGA model number HCS-105-120V) shown in Fig. 5.7 is mounted next to the left side wall of the main enclosure to provide the heat flux and maintain high temperature on this surface. Thermal paste is applied on the contact surfaces of the strip heater and the left side wall for better heat conduction. The

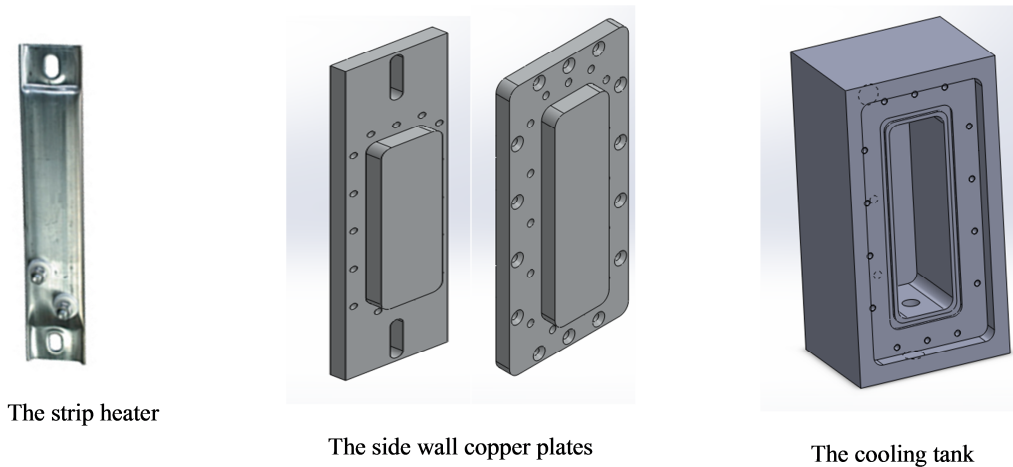


Figure 5.9: The side wall copper plates.

applied heat flux to the strip heater is provided by a variable autotransformer and voltage is measured using a Hewlett Packard (model number 34401A) multimeter. When the temperature of the heater exceeds a threshold temperature of $60^{\circ}C$ a LabVIEW process immediately switches off the solid state relay, cutting the power to the heater. Nomex insulation with thermal conductivity of 0.029 W/mK was wrapped on the side of the heater to minimize the heat loss from the system to the ambient air. A cooling tank (see Fig. 5.7) was installed adjacent to the right side wall of the main enclosure to maintain cold temperature on this surface by passing the cooling water from a chiller (Thermo Scientific-NESLAB Liquid-Liquid Recirculator) through it. The cooling tank is made out of CPVC (Chlorinated Polyvinyl Chloride). On each of the wall side walls, 5 drilled holes were allocated for installing T-type thermocouples at a 0.001m distance from the inner surface of the side walls to measure the local temperatures of the copper plates.

The front window: The front window of the main enclosure is a $0.130\text{m} \times 0.050\text{m} \times 0.009\text{m}$ transparent polycarbonate rectangle to allow for visualization of the experiment. The polycarbonate is also a good insulating material to prevent heat loss from the inside liquid to the outside.

Thread sealant SB75-010 from SPEARS manufacturing company is used as the sealant

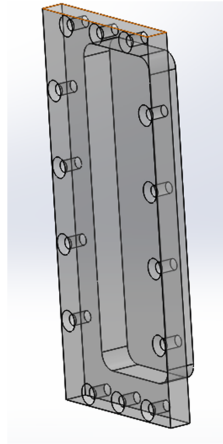


Figure 5.10: The front window of the main enclosure.

for all the PVC fittings. For safety considerations, an indoor steel enclosure with lift-off cover (nema 1) is used to enfold all the electrical connections. 3M Scotch brand electrical tape is used for the electrical insulation. Electrical protection rubber gloves were used for safety purposes during running the experiment and data acquisition.

Specification of the Working Fluid

The natural convection experiments were conducted for both water and MEPCM slurry. Two different types of MEPCM slurries were obtained from PureTemp company [4] as samples. The initial volumetric concentration of the MEPCM slurries were 40% which were modified according to the desired concentration values for each experiment. Photos of these MEPCM slurries are shown in Fig. 5.13. The properties of the MEPCM materials are listed in Table 5.2 and their corresponding DSC curves are included in Fig. 5.3.

5.6 Experimental Procedure

For each experiment, the heater power was manually adjusted using the variable transformer until the device reached steady state with the desired applied heat flux and the

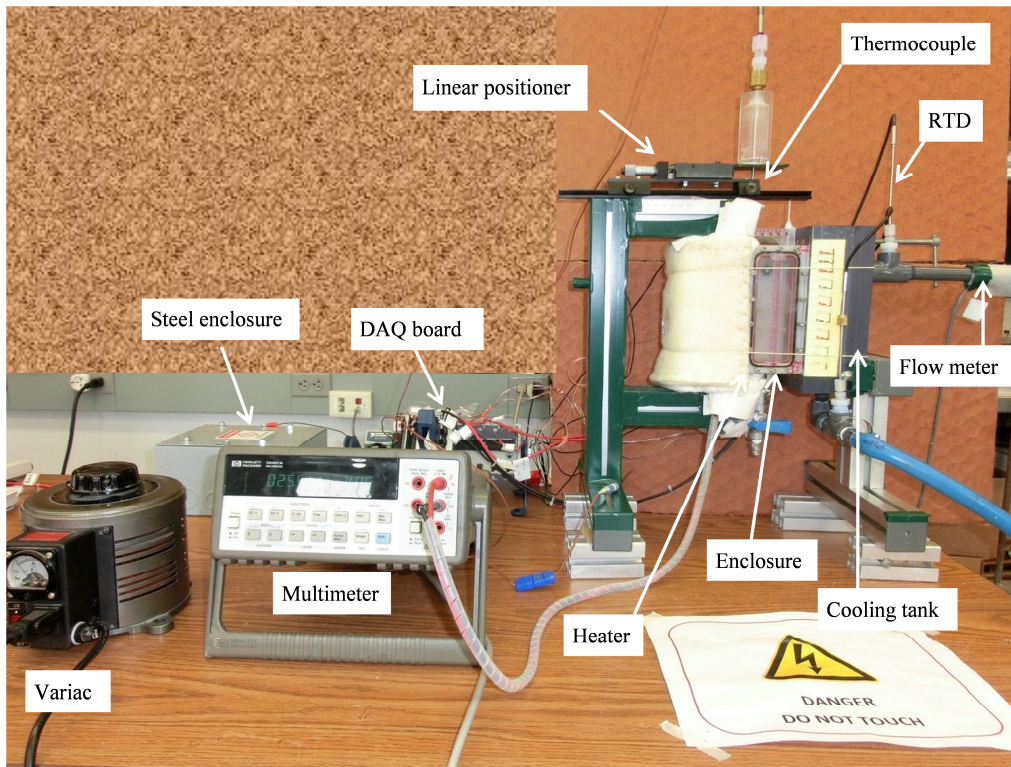


Figure 5.11: Photo of the experimental setup arrangement.

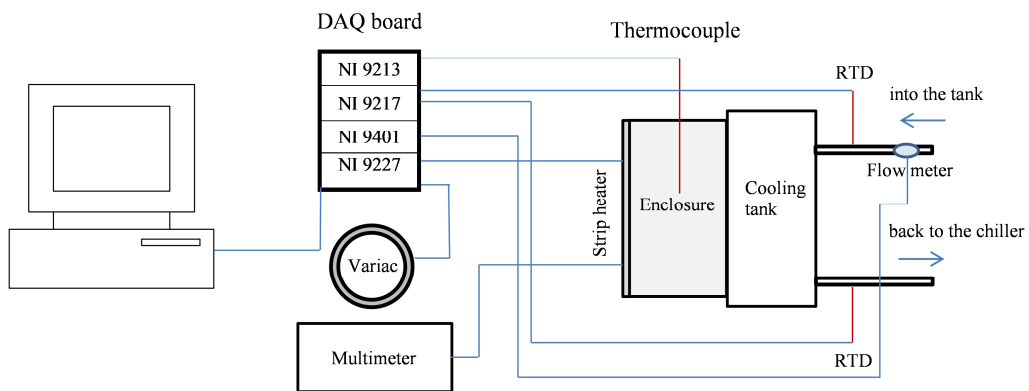


Figure 5.12: Schematic of the experimental setup arrangement.

Table 5.2: PCM properties provided by PureTemp [4]

Property	PureTemp 28 Technical Information	PureTemp 37 Technical Information
Appearance	Clear liquid, waxy solid	Clear liquid, waxy solid
Melting Point	29°C	38°C
Heat storage capacity	205 J/g	222 J/g
Density	0.86 g/ml	0.84 g/ml
Specific heat liquid	2.54 J/g°C	2.63 J/g°C
Specific heat solid	2.34 J/g°C	2.21 J/g°C
Solubility in water	Insoluble	Insoluble
Stability	Stable under normal conditions	Stable under normal conditions



Figure 5.13: Samples of MEPCM slurries.

Table 5.3: Summary of operating conditions.

Case	Material	MEPCM Concentration (%)	q'' (W/m ²)	T_c (C)
1	Water	0	2700, 3524	20, 30
2	PureTemp28	10, 15	2700, 3524	20, 30
3	PureTemp37	10, 15	2700, 3524	20, 30

cold wall temperature. The chiller set point temperature was tuned according to the cold wall temperature settings. The tests were performed for pure water, and the two types of the MEPCMs with concentrations of 10% and 15%. The operating conditions for different experimental tests are summarized in Table. 5.3.

The NI LabVIEW was used to create a custom user interface for data acquisition. Figure 5.15 shows the graphical user interface (GUI) for data acquisition of this experiment to measure and monitor the values of temperature, flow rate, current, resistance and power. Once steady state was reached, all data readings were recorded. The NI cDAQ-9178 DAQ boards with the following modules have been used for the corresponding measurements:

- NI 9213 for temperature measurements of the J-type and T-type thermocouples.
- NI 9217 for temperature measurements of the RTDs.
- NI 9401 for the frequency measurement of the flow meter.
- NI 9227 for the current measurement. This is a 4-Channel Current Input C Series Module.

The details of each of the mentioned measurements are explained as follows:

Side wall temperatures: The temperatures of the two side copper walls were recorded by measuring the temperature on 5 locations on each of the side walls. T-type PFA in-

sulated wire thermocouples (model number 5TC-TT-T-36-36) from OMEGA were used. They met Special Limits of Error (SLE) and Tolerance Class EN 60584-2.

Liquid temperature profile: To get the bulk liquid temperature profile across the two sides of the enclosure, a SUB MINI TJ W/FITTING thermocouple (model number JMTSS-010G-12) from OMEGA with 24-bit ADC for up to 0.02C measurement sensitivity was used. This is a J-type thermocouple, with stainless steel sheath material. The sheath diameter is 0.010 inches and it is 12 inches long. The thermocouple junction is grounded. The J-type thermocouple was manually moved using a linear positioner with 1 mm step increments near the boundaries of the side walls and 5 mm steps in the mid-section of the enclosure where the variation of temperature is less significant. At each position of the J-type thermocouple, the data acquisition was controlled through the VI for duration of 60 seconds at a sample rate of one sample per second.

Ambient air temperature: To measure the ambient air temperature a T-type thermocouple (part number TMTSS-062U-6) from OMEGA was used.

Cooling water temperatures: The inlet and outlet temperatures of the cooling water from the chiller were measured using two RTD probes inserted in the connecting tubes. The RTD sensors used in this study were 100 Ω platinum-type sensors conforming to IEC Standard 60751 Class B tolerances.

Cooling water flow rate: The FTB2001 turbine flow rate sensor by OMEGA was used to measure the flow rate of the cooling water from the chiller. The flow meter had to be calibrated in order to convert the frequency into flow rate. The following calibration curve for the flow rate vs. flow meter frequency is obtained and displayed in Fig. 5.14.

Applied voltage: Hewlett Packard (model number 34401A) multimeter was used to measure the applied voltage.

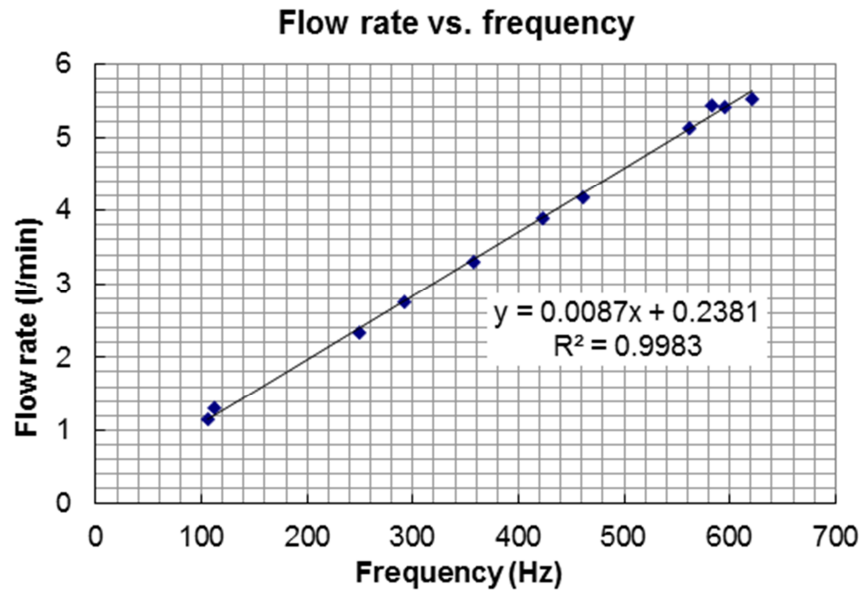


Figure 5.14: Flow rate vs. frequency of the flow meter.

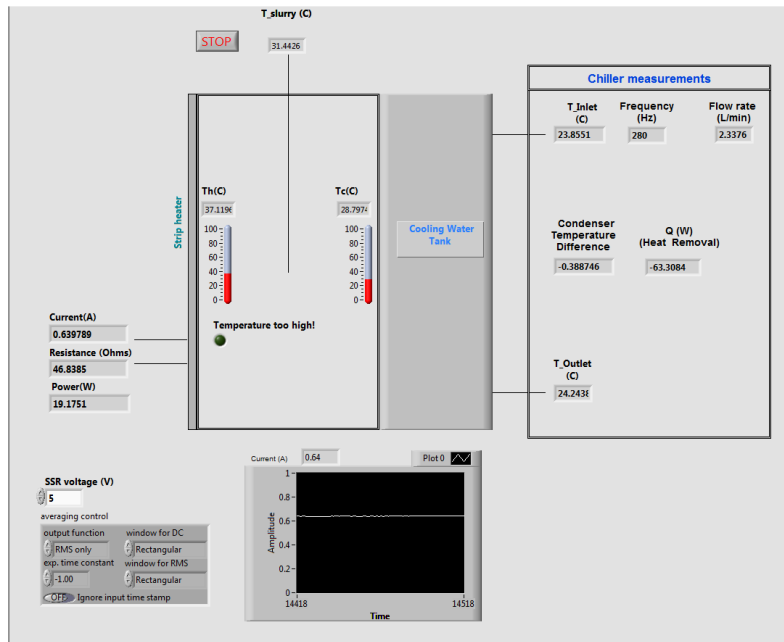


Figure 5.15: The LabVIEW GUI for the current experiment.

Table 5.4: Accuracy of the measurement devices.

Measurement	Accuracy
Temperature	± 0.05 °C
Current	± 10.6 mA
Voltage	± 0.168 V
Resistance	± 0.87 Ω
Flow rate	± 0.0013 kg/s

Data Analysis

The average heat transfer coefficient is calculated as follows,

$$h = \frac{q''}{T_h - T_c} \quad (5.23)$$

where q'' is the heat flux applied to the left side wall of the enclosure and T_h and T_c are the average values of the measured temperatures along the side copper walls. The heat flux, q'' , is defined as,

$$q'' = \frac{Q}{A} \quad (5.24)$$

where A is the surface area of the heater and Q is the total heat supplied to the heater and measured by acquiring the values the heater resistance and applied current as follows,

$$Q = RI^2 \quad (5.25)$$

5.7 Analysis of Experimental Results

The experimental data is obtained for various operating conditions presented in Table 5.3. The accuracy of the measurement devices are provided in manufacturer specification sheets. These values are given in Table 5.4

Figure 5.16 shows the variation of local temperature long the centerline of the reser-

	h (W/m ² K)	q'' (W/m ²)	T_h (C)	T_c (C)
Exp-water-H-02-19-14	339 ± 11	3523 ± 108	40.81 ± 0.024	30.42 ± 0.080
Exp-water-H-02-21-14-Test 1	364 ± 11	3758 ± 115	40.78 ± 0.024	30.45 ± 0.083
Exp-water-H-02-21-14-Test2	340 ± 11	3735 ± 115	41.2 ± 0.023	30.21 ± 0.083

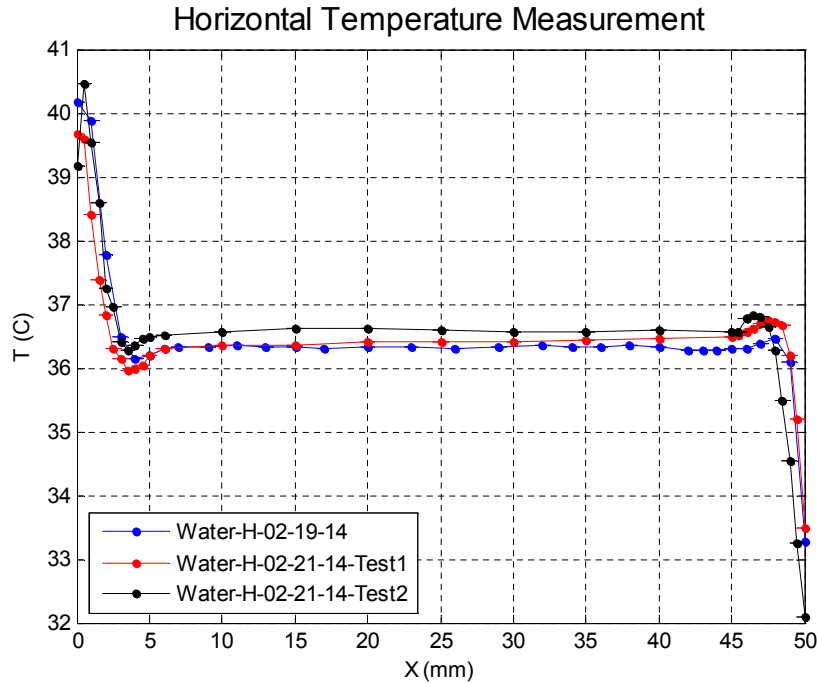


Figure 5.16: Experimental measurement of temperature profile along the centerline for case of pure water for different tests.

voir for case of pure water obtained at different tests. The plot demonstrates the repeatability of the experimental data over similar operating conditions with maximum deviation in the measured temperature not exceeding $\approx 0.2^{\circ}C$. The temperature of the incoming fluid (from the cold side wall) towards the hot side wall is lower than the fluid in the center. This results in the presence of the dips in the temperature profile in the vicinity of the hot side wall as shown in Fig. 5.16. Same explanation for the liquid flow next to the hot side wall is valid for to account for the variation of the temperature profile in that region. The effect of MEPCM concentration on the temperature profile across the centerline is presented in Fig. 5.17. The value of the measured heat transfer coefficient is also reported

	h (W/m ² K)	q'' (W/m ²)	T_h (C)	T_c (C)
Exp-water-H-02-19-14	339 ± 11	3523 ± 108	40.81 ± 0.023	30.42 ± 0.082
Exp-water-H-02-21-14-Test 1	309 ± 10	3525 ± 108	41.93 ± 0.022	30.52 ± 0.081
Exp-water-H-02-21-14-Test2	300 ± 9	3529 ± 108	42.28 ± 0.021	30.5 ± 0.084

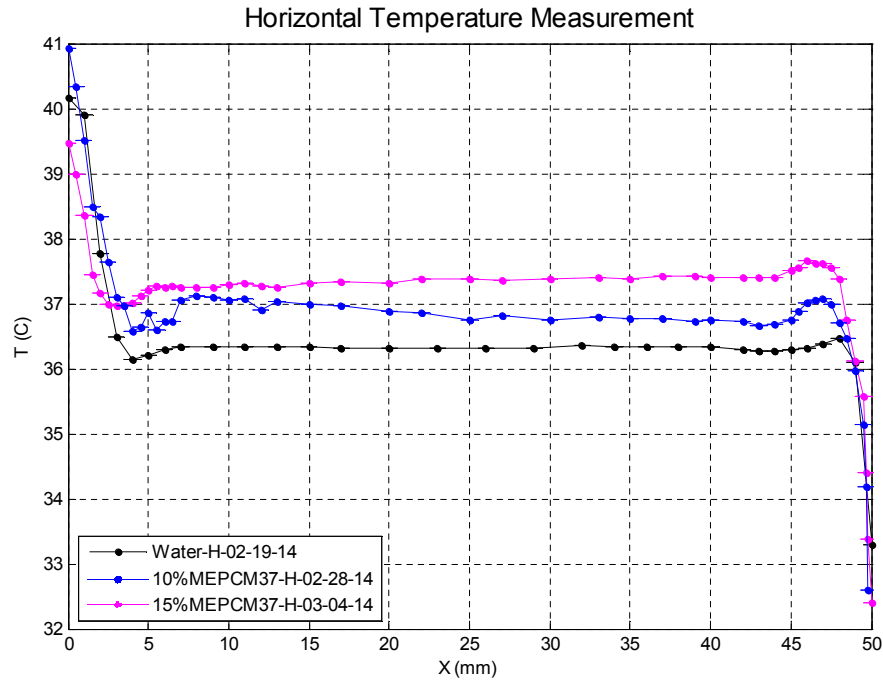


Figure 5.17: Experimental measurement of temperature profile along the centerline for case of pure water and slurry of different MEPCM concentrations.

for comparison. The experimental results show that the presence of MEPCM results in lower heat transfer coefficient compared to that of pure water with higher concentration resulting in aggregated deterioration of heat transfer coefficient. In addition, the temperature profile across the centerline suggests that lower heat transfer coefficient of MEPCM slurries is associated with higher temperature values along the centerline. This suggests that when MEPCM is present, the generated flow field is suppressed due to a lower overall temperature difference between the hot plate and the centerline. The physical explanation for this behavior is provided in the following section. The experimental results for the temperature profiles of water along with two MEPCM slurry cases (different types) are

	h ($W/m^2 K$)	q'' (W/m^2)	T_h (C)	T_c (C)
Exp-water-H-02-19-14	331 ± 10	2702 ± 83	36.31 ± 0.021	28.14 ± 0.085
Exp-water-H-02-21-14-Test 1	273 ± 9	2701 ± 83	37.92 ± 0.023	28.01 ± 0.080
Exp-water-H-02-21-14-Test2	250 ± 8	2694 ± 83	38.81 ± 0.021	28.02 ± 0.081

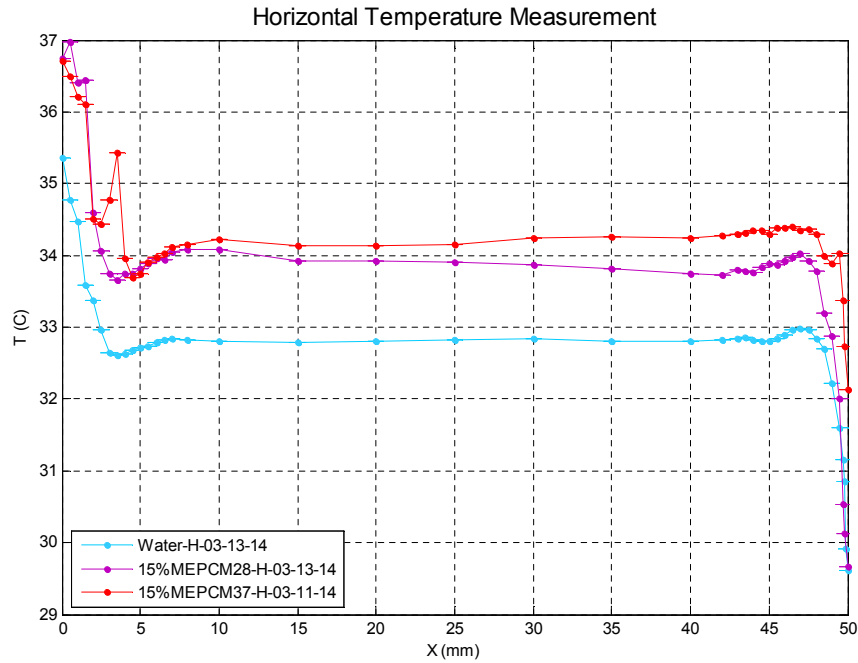


Figure 5.18: Experimental measurement of temperature profile along the centerline for case of pure water and slurry of different MEPCM types.

shown in Fig. 5.18. The applied heat flux is $q'' = 2701.43W/m^2$ in all cases and the cold wall temperature is maintained at $28^{\circ}C$. The results show that temperature at the centerline of the enclosure is lowest for pure water and it is followed by the MEPCM28 and then by MEPCM37. According to the reported values of heat transfer coefficient, the slurry with both MEPCMs exhibits lower thermal performance compared to that of pure water with a more significant drop for case of MEPCM28.

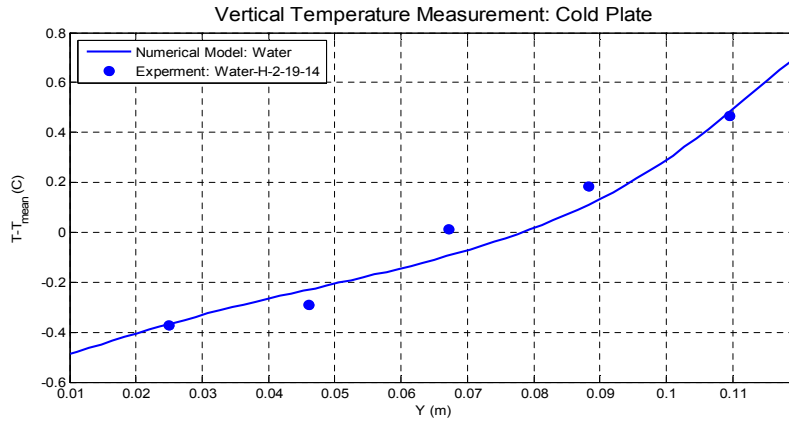


Figure 5.19: Variation of the deviation of local wall temperature from the mean temperature both calculated on the cold plate: Comparison of experimental measurement and numerical prediction for case of pure water.

5.8 Comparison of Numerical and Experimental Results

Local temperature measurement along walls: comparison between model and experiment

Figure 5.19 shows the variation of the local wall temperature from the mean temperature. The mean temperature is calculated across the entire plate and among the five measurement points, respectively, for the numerical model and the experimental data set. A comparison between the experimental data and numerical results for water shows a good agreement. In both cases, the applied heat flux is $q'' = 3500W/m^2$ and $T_c = 30^\circ C$. The plate temperature increases along the wall due to the naturally driven flow of the warmer fluid towards the top of the enclosure. Same trend could be established for the temperature variation along the hot plate.

Temperature variation across the enclosure

Figure 5.20 compares the experimental and numerical results of the horizontal temperature profile along the centerline of the enclosure with a good agreement. In both cases, the

	h (W/m ² K)	q'' (W/m ²)	T_h (C)	T_c (C)
Exp-water-H-02-19-14	339 ± 11	3523 ± 108	40.81 ± 0.021	30.42 ± 0.083
Exp-water-H-02-21-14-Test 1	310 ± 10	3523 ± 108	42.81 ± 0.024	31.45 ± 0.080
Exp-water-H-02-21-14-Test2	309 ± 10	3525 ± 108	41.93 ± 0.022	30.52 ± 0.083
Numerical-10%MEPCM37	296	3525	42.88	30.96

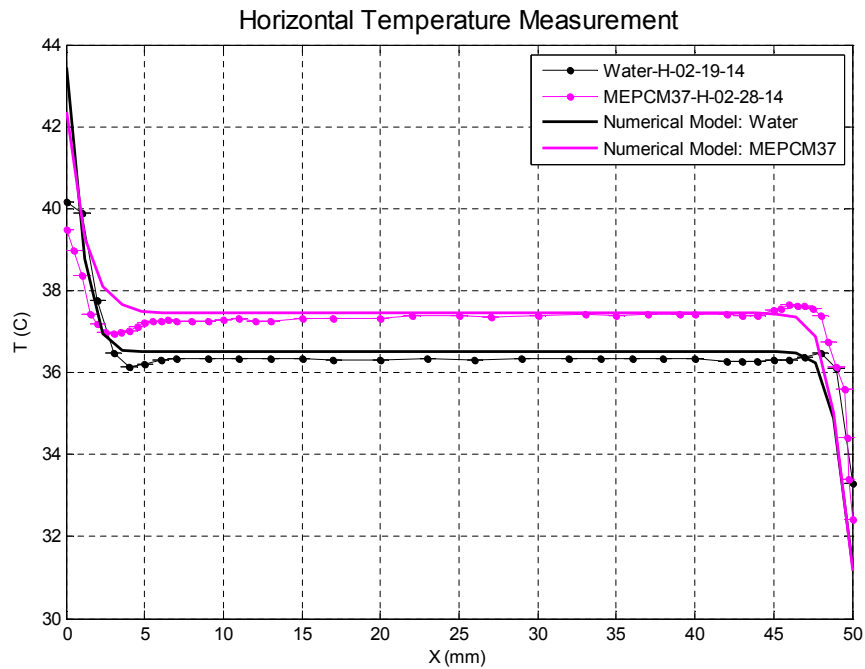


Figure 5.20: Temperature profile across the centerline of the enclosure: Comparison of experimental measurement and numerical prediction for case of pure water and MEPCM slurry.

applied heat flux is $q'' = 3500W/m^2$ and $T_c = 30^\circ C$. Both the model and experimental measurements demonstrate the sharp variation of temperature from the wall value to the centerline value, though the temperature gradient appears to be sharper on the cold side than on the hot side.

Effect of concentration on temperature distribution and heat transfer coefficient

The following figures compare the effect of MEPCM concentration on the temperature profile along the centerline (5.21) and the heat transfer performance (5.22) relative to water. Figure 5.21 presents the temperature profile for water, 10% MEPCM slurry and 15% MEPCM slurry based on experimental data for similar applied heat flux ($q'' = 3500W/m^2K$). The temperature on the centerline has its lowest values when water is used as the fluid and its highest value when 15% MEPCM slurry is present. Both slurries show lower heat transfer coefficient compared to water as depicted in Fig. 5.22, though the rate of decline appears to be significantly suppressed for concentrations of larger than 10%. The numerical results, show consistently that the heat transfer coefficient for all the slurries remain largely the same and significantly less than the one for water ($h/h_w < 0.85$). This suggests that the presence of MEPCM tends to decrease the primary heat-transfer property of the fluid (that is the thermal conductivity) irrespective of its concentration and as shown later, the type of MEPCM.

Effect of MEPCM type on overall heat transfer coefficient

The heat transfer performance of two different MEPCM slurries are compared with that of pure water. The applied heat flux and the cold wall temperatures are $q'' = 3524W/m^2$ and $T_c = 30^\circ C$ in Fig. 5.23 and $q'' = 2701W/m^2$ and $T_c = 20^\circ C$ in Fig. 5.24. The primary motivation for this selection of operating conditions is to achieve hot plate temperatures that are close to the corresponding melting temperature of MEPCM37 ($q'' = 3524W/m^2$) and MEPCM28 ($q'' = 2701W/m^2$). The plots also compare the experimental results with the numerical simulations. As shown in these plots, the heat transfer coefficient of pure water is highest compared to the MECPM slurries in both numerical and experimental

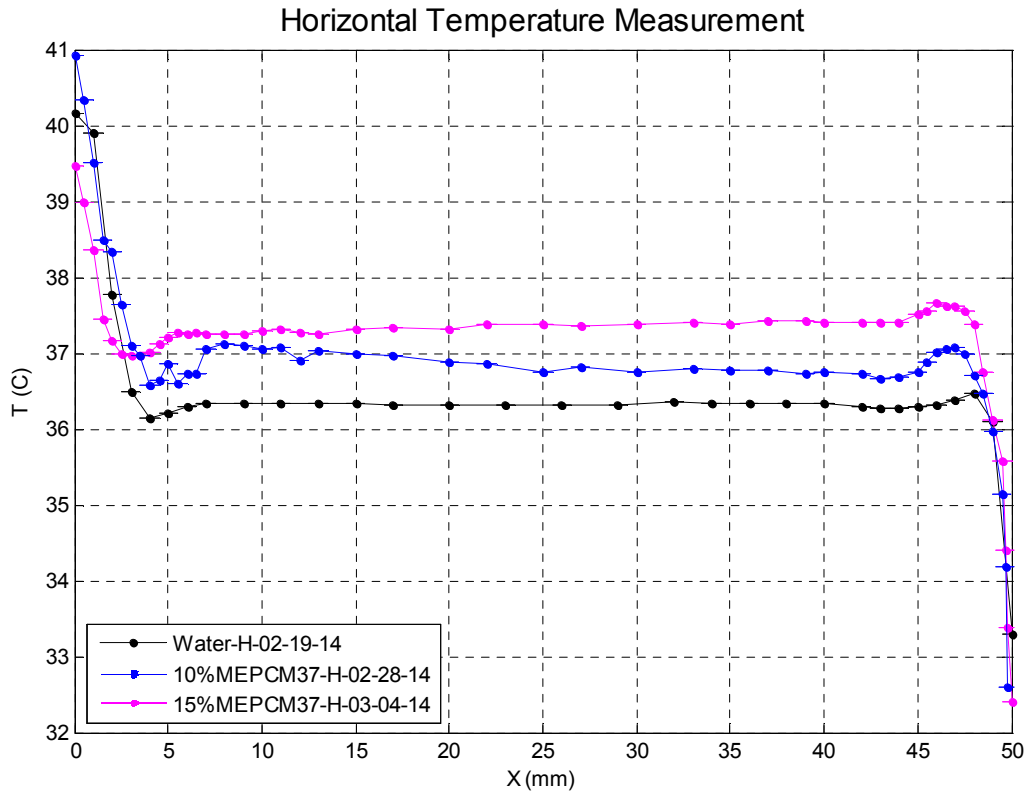


Figure 5.21: Experimentally measured temperature profile across the centerline for different MEPCM concentrations.

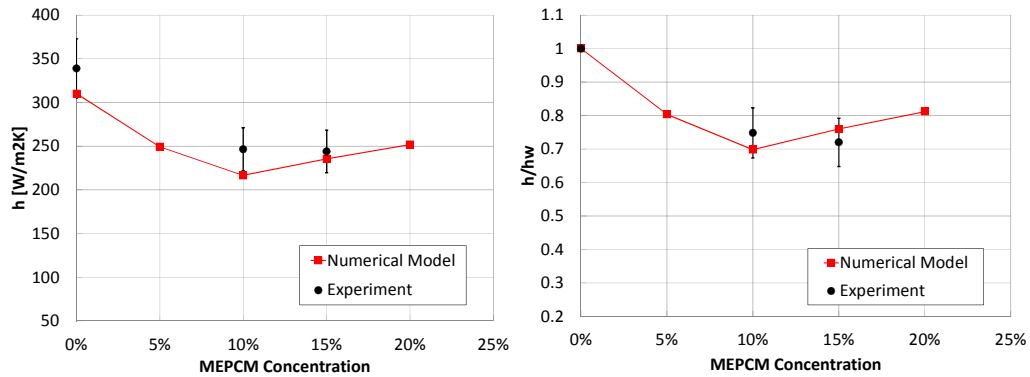


Figure 5.22: Variation of heat transfer coefficient (left) and its ratio with respect to the one for pure water with MEPCM concentration: Comparison of experimental measurement and numerical prediction

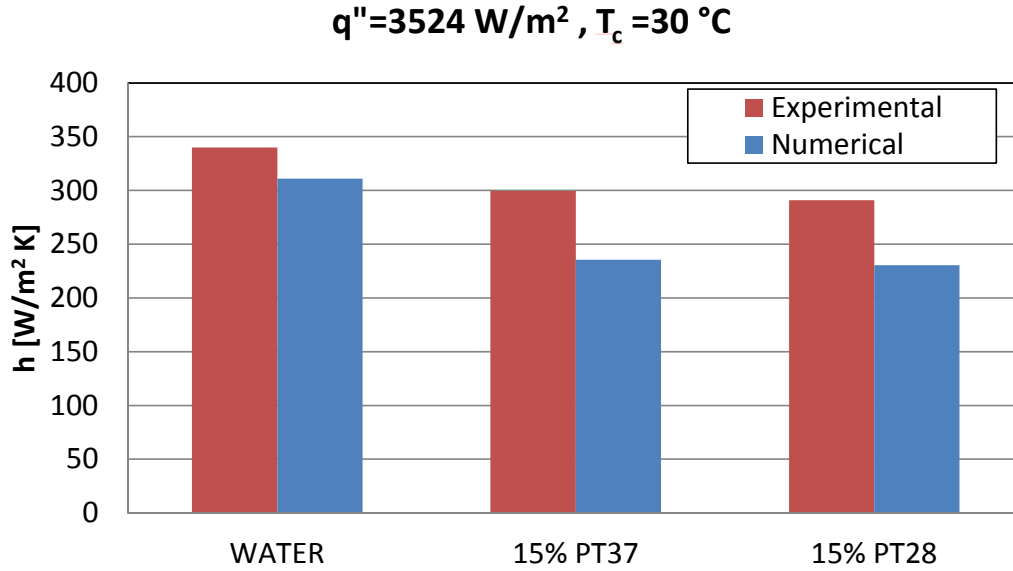


Figure 5.23: Average heat transfer coefficient for pure water and 15% MEPCM slurry at $q'' = 3524 \text{ W/m}^2$ and $T_c = 30^\circ\text{C}$: Comparison of experimental measurement and numerical prediction

results and for the two different applied heat fluxes. There is a slight difference between the performance of the two MEPCM slurries which confirms the earlier theory that the presence of MEPCM, irrespective of its concentration and type, reduces the overall heat transfer performance. The differences between the numerical and experimental results can be attributed to that fact that the particle size distribution in numerical model is considered based on a mean diameter value while in reality and in the experimental material, there is range of particle diameters existing in the slurry. The numerical and the experimental results are non-dimensionalized to be presented in terms of variation of Nusselt number as a function of operating Rayleigh number. The operating Rayleigh number is conventionally defined for fluids with known thermal expansion coefficient and has the following form,

$$Ra = \frac{g\beta(T_h - T_c)W^3}{\nu_{\text{eff}}\alpha_{\text{eff}}} \quad (5.26)$$

For the cases presented here, however, the thermal expansion coefficient, β , changes with temperature and does not possess a constant value for neither pure water nor for

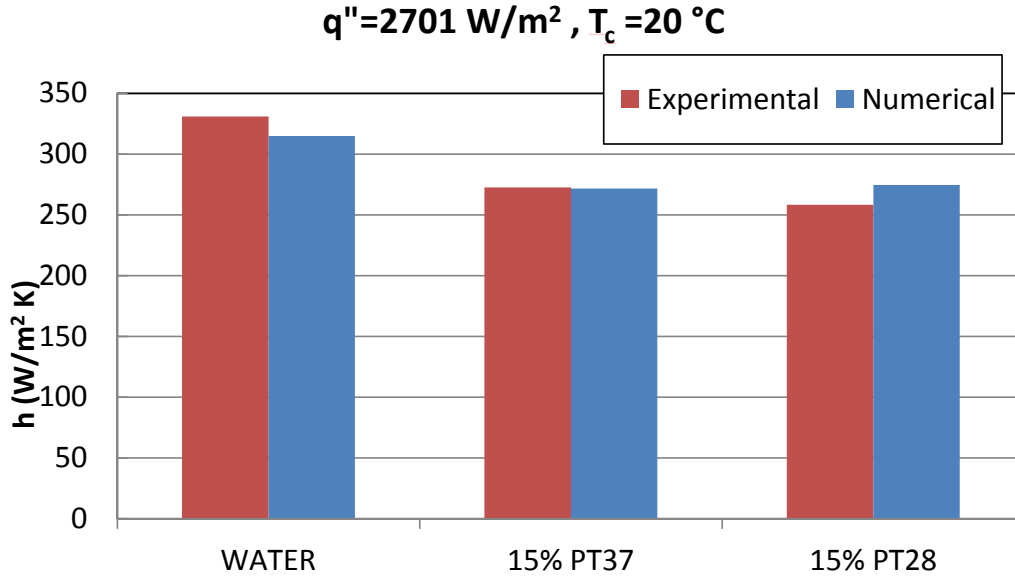


Figure 5.24: Average heat transfer coefficient for pure water and 15% MEPCM slurry at $q'' = 2701 \text{ W/m}^2$ and $T_c = 20^\circ\text{C}$: Comparison of experimental measurement and numerical prediction

MEPCM slurry. Therefore, an approximate value of β is defined as follows,

$$\beta \approx -\frac{1}{\rho_{\text{eff}}} \left(\frac{\partial \rho_{\text{eff}}}{\partial T} \right)_{T=\bar{T}}, \quad \bar{T} = \frac{T_h + T_c}{2} \quad (5.27)$$

Figure 5.25 presents the variation of Nusselt number as a function of Rayleigh number for the same operating conditions presented so far. This plots suggests that the combination of the differences between the properties of the pure water and MEPCM leads to the correspondingly different Rayleigh number for similar operating conditions (i.e. applied heat flux and cold side temperature). As the result, despite a lower heat transfer performance of MEPCM slurry flow than the one for water for same operating conditions, it shows superior performance for similar Ra number. This difference can be attributed to the fact that the temperature dependency of the thermal expansion coefficient for the case of slurry flow varies more significantly across the temperature range investigated here which leads to a more dramatic drop in the Ra number when the temperature is reduced.

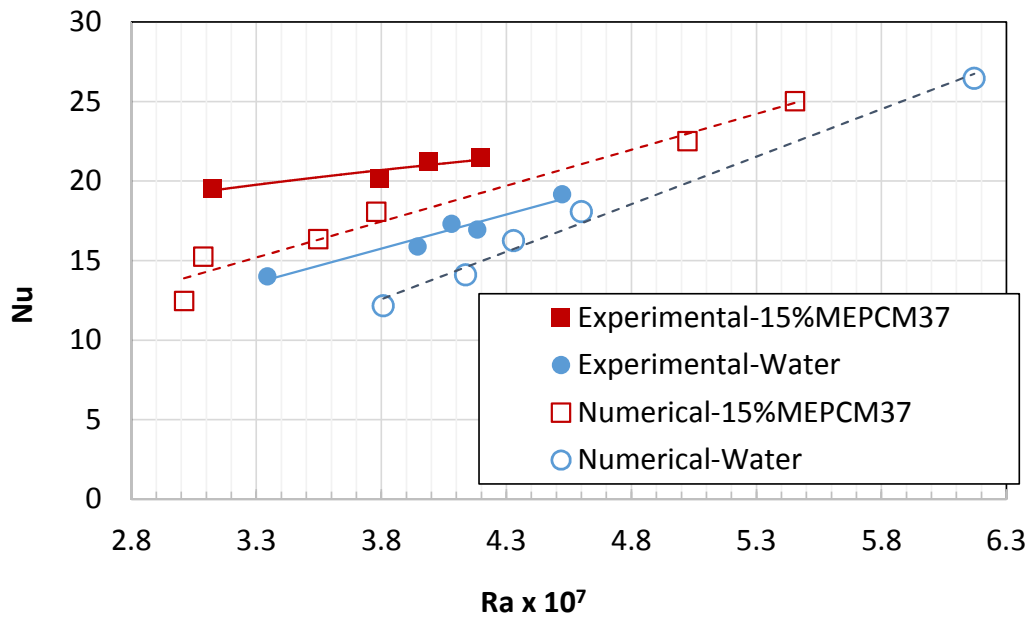


Figure 5.25: Average Nusselt number as a function of Ra number for case of pure water and 15% MEPCM slurry: Comparison of experimental measurement and numerical prediction

5.9 Conclusions

A numerical and experimental study was conducted to investigate the thermo-fluid characteristics of buoyancy driven liquid flow inside a rectangular enclosure subject to a certain temperature difference on the vertical side walls. The temperature difference was maintained by applying a constant heat flux on one side and a coolant water on the opposite side. As for the heat transfer performance of the natural convection flow, the numerical results were in good agreement with experimental data. Both the predictions and measurements showed that the MEPCM slurry underperforms the pure water counterpart for the considered operating conditions. The decline in heat transfer performance was attributed to the lower thermal conductivity of the MEPCM slurry compared to that of pure water along with the increase in the effective viscosity of the liquid. The numerical results showed that the larger effective viscosity results in lower velocities raised by the naturally induced liquid flow which leads to a diminished thermal performance when assessed against the case of pure water. In addition, the results were recast into dimensionless values where the variation of Nusselt number with Rayleigh number showed that despite lower heat transfer performance for similar operating conditions, the MEPCM slurry's thermal performance is superior to that of pure water for a given Rayleigh number. This difference in the trend-wise behavior of the heat transfer coefficient was attributed to the difference in the thermo-fluid properties of the MEPCM slurry and pure water.

Chapter 6

Enhancement of Paper Drying Process with PCM

6.1 Objective

This work numerically investigates the transport characteristics associated with the drying process of a paper sheet in the presence and absence of a layer of phase change material (PCM). This unique concept offers a new approach to drying by utilizing the latent-heat of fusion associated with the PCM resulting in improvement in energy efficiency of the drying process. The results indicate that the PCM layer acts as a heat source and heat sink throughout the drying process. The proposed operating conditions and configuration presented here are solely for the purpose of illustration of the concept of drying in the presence of PCM.

6.2 Introduction

Drying is one of the most energy intensive unit operations in the industrial sector, accounting for 1/3 of the total energy in paper-making. Drying is also extremely energy inefficient and represents a major production bottleneck in many industrial processes [69].

Almost all major industries used thermal drying systems during some stage of the manufacturing process [69]. Drying in the pharmaceutical industry removes moisture from chemicals in powder or granular form. The agricultural industry uses industrial dryers to produce dehydrated vegetables, soups, beverages and other products. The textile industry adds water during washing, bleaching and dyeing stages. This moisture is later removed by a combination of thermal and mechanical processes. Drying in the plastic industry removes moisture from resins and extruded plastics. The pulp and paper industry uses thermal dryers from pulp products and for the continuous drying of paper products.

Depending on the industry and technology, drying can represent a significant fraction of the industrial energy use. For example, energy for drying consists up to 70% of the total energy in manufacturing most wood products, about 50% of finished textile fabrics, 27% of paper, and 33% of pulp production [70].

The pulp and paper industry is the fifth largest manufacturing industry in the United States. It ranks fourth in total energy consumption by U.S. manufacturers behind chemicals, steel and petroleum [69]. Rising energy costs are forcing paper makers to pay more attention to energy efficiency, and specially steam usage [71]. That being said, even a slight improvement in the drying efficiency can reduce the energy consumption in the drying technology and hence resulting a major impact in the global energy costs. For instance and to underline the significance of the energy saving in drying industry, Lawrence Berkeley national laboratory provided a detail report of the description of the processes involved in the production of paper, providing typical energy use in each process step [72].

The commercially available state-of-the-art technologies were identified and potential energy savings were calculated towards carbon dioxide emissions reductions.

The paper making process is essentially a very large dewatering operation where a diluted solution of pulp suspension with less than 0.5% fibre solid is used. The major sections of a paper machine consist of: forming section, press section and dryer section. In the forming section, the fibres present in the diluted pulp and water slurry form paper web through drainage by gravity and applied suction below the forming fabric. In the press section additional water is removed by mechanical pressure applied through the nips of a series of presses or rotating rolls and the wet web is consolidated in this section. Most of the remaining water is evaporated and inter-fibre binding developed as the paper contacts a series of steam heated cylinders in the dryer section. The type and quality of the final paper product depends on the moisture removal in the final step which makes it one of the most critical steps of paper making [71].

Several conditions drive and determine the efficiency of the paper drying process. For instance, the effectiveness of the moisture removal which is largely driven by the heat and water and vapor mass transfer depends on the steam pressure, cylinder surface temperature, dryer pocket conditions, hood balance and condensate removal [71]. The rate of drying, therefore, is governed by the rate of heat and mass transfer across the paper sheet. Energy transfer as heat from the surrounding environment to the wet solid can occur as a result of convection, conduction, or radiation and in some cases as a result of a combination of these effects. Industrial dryers differ in type and design, depending on the principal method of heat transfer employed. In most cases heat is transferred to the surface of the wet solid and then to the interior [73].

Despite the criticality of the drying process in paper making industry, it remains one of the the least optimized processes in the paper making operation, due, in large part, to the complexity of the processes involved. Along with the increase in computer speed and

capabilities and an increased recognition of the complexities of the transport phenomena involved in drying, the models grew more complicated [74].

The first comprehensive literature review [75], covered simulation models to 1980, although it must be recognized that the preliminary models for drying processes go back to the 1950s [74]. The primary contribution to paper drying modeling was accomplished by Nissan and Kaye [76]. Their model allowed for contact heat transfer by conduction from the cylinder, for convection and radiation to the paper and for evaporation from the sheet. Later and in a work by Lampinen and Toivonen [77], a cylinder drying model was developed which treated mass transfer as water vapor diffusion and liquid moisture capillary flow. The Asensio and Seyed-Yagoobi model [78, 79] is an improved version of the Han work [80] in which correlations for estimation of sheet thickness and porosity during drying were included and experimental results were used to develop an empirical correlation for the cylinder-paper contact heat transfer coefficient. In addition, Asensio [81] developed a model for convective drying of lumber which is distinguished by its thorough description of internal transport phenomena, including the treatment of water vapor transport by diffusion and convection as well as liquid transport by both capillary action and diffusion of sorbed water. Although it covers literatures only up to 1992, [82] provided a concise tabular summary which was extended by Sidwall et al. [83]. They underscore the great variability to the approach several researchers had taken to include aspects external to the sheet involving the steam and condensate system, the cylinder dynamics (shell resistance, condensate layer, spoiler bars) and ventilation of the dryer pocket air.

The investigation of alternative drying techniques was a subject of research recently. For instance, Etemoglu et. al [84] presented a theoretical and experimental study of paper drying process and developed a mathematical model for the heat and mass transfer for both impinging air jets and through air drying methods. They predicted the results of the

total drying time of paper and showed good agreement with the experimental results. In addition, Lu et al. [85] developed a numerical model which was also validated against their experimental data where convective drying in unsaturated porous media with bound water was investigated. Further innovative approaches towards enhancing the moisture removal efficiency during the drying process is yet to be explored.

To the best of knowledge of the authors, no previous study has investigated the effect of phase change material (PCM) on drying of moist porous medium. The current numerical approach investigates the transport characteristics associated with the drying process of a paper sheet in the presence of a layer of PCM. The main objective of this study is to understand the effect of adding a PCM layer in the paper sheet on the moisture removal and drying process. This unique concept offers a new approach to drying by utilizing the latent-heat of fusion associated with the PCM to improve the energy efficiency of paper drying process. Also, to avoid the complications of the problem, no felt is present in the drying setup of the current study.

6.3 Approach

The drying process involves the evaporation of liquid moisture inside the paper sheet due to its exposure to the heated drums as well as the hot air. The different stages of drying are presented schematically in Fig. 6.3. The paper sheet is heated due to its contact to the heated cylinders from one side while it is exposed to ambient air on the other end in the process known as pocket air ventilation which is defined as the space in the dryer section between two adjacent cylinders, in case of single-tier system, or between three cylinders, in case of conventional two-tier system. The energy for the drying process comes from saturated steam injected under pressure into the cylinders. The steam pressures in conventional dryers range from 0-1000 kPa (0-145 psi) as steam condenses on the inside of

the dryer shell the latent heat of evaporation is released. The heat is transferred through the condensate layer and dryer shell to the paper on the outside surface [69].

Individual pocket is separated by dryer fabric and paper web. In this area majority of evaporation occur from the web. For the efficient drying of paper, it is extremely important to remove the water vapor from around the web to increase the driving force for evaporation. Therefore, not only the surface temperature is important in the water removal from the paper sheet, the drying performance is dependent on the rate of water removal to the hot and dry air. For instance, if the movement of air in the pockets is too low or close to stagnation, higher temperature in the pockets does not help in improving drying rate. There should be sufficient airflow in the pockets for efficient drying [71]

In the following stage and while the paper sheet is travelling to the subsequent cylinder, the sheet is exposed to ambient air from both sides. The contact heating on the subsequent cylinder is switched to the opposite end of the paper sheet while the other end is now being exposed to the ambient air.

Given the significance of moisture removal performance in the overall efficiency of the drying process and the inherent availability of latent heat raised by Phase-Change-Material during the melting process, the use of PCM on enhancing the moisture removal performance of the paper sheet is explored here. The primary objective of this work is to illustrate the effect of adding a PCM layer to the drying performance under a given set of operating condition. To take the advantage of latent heat of melting of the PCM, the PCM layer is proposed to be designated in the middle of the paper sheet as illustrated in Fig. 6.1.

The presence of PCM layer is accounted by adjusting the thermal properties of the paper sheet assuming that the liquid and vapor mass transfer processes are not affected by the presence of PCM layer and only occur from the paper sheet to the ambient air. The following steps illustrate the concept of drying process in the presence of a layer of PCM,

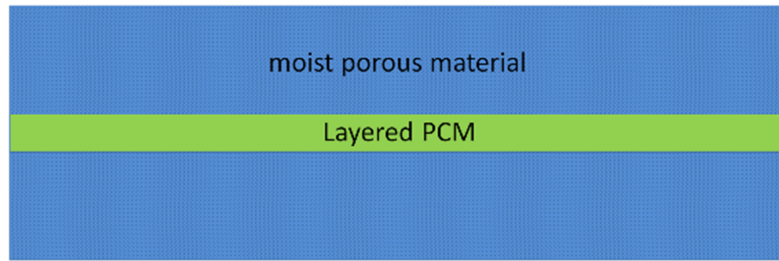


Figure 6.1: Schematic illustration of the approach presented in this work.

1. The PCM layer absorbs heat at its contact interface with the paper sheet during the heating period and undergoes solid-to-liquid phase change,
2. During the pocket ventilation process, the PCM releases the stored heat due to the exposure of the sheet to the lower temperature, extending the duration of water evaporation from the paper sheet,
3. While releasing heat to the paper sheet, the PCM solidifies during the pocket ventilation process and preceding the subsequent heating cycle,
4. Steps 1-3 repeat as the sheet goes to the next cycle.

Note that the PCM phase change properties must be tuned to the corresponding drying operating conditions. The latent heat of melting of PCM is represented by the temperature dependent specific heat presented in Fig. 6.2 where the peak in the value of specific heat corresponds to the melting of the PCM. The temperature value at which the melting occurs depends on the type of the PCM which can be selected based on the operating temperatures of the drying process. It is worth emphasising that since the objective of this work is to demonstrate the benefits of using PCM layer, an arbitrary PCM melting temperature has been selected. The proposed operating conditions presented here are solely for the purpose of illustration of the concept of drying in the presence of PCM. The advantage of using the latent heat of the PCM layer is exploited in this case study by tuning its peak temperature, $T_{\text{peak,PCM}}$ to the temperature of the paper sheet at the end the

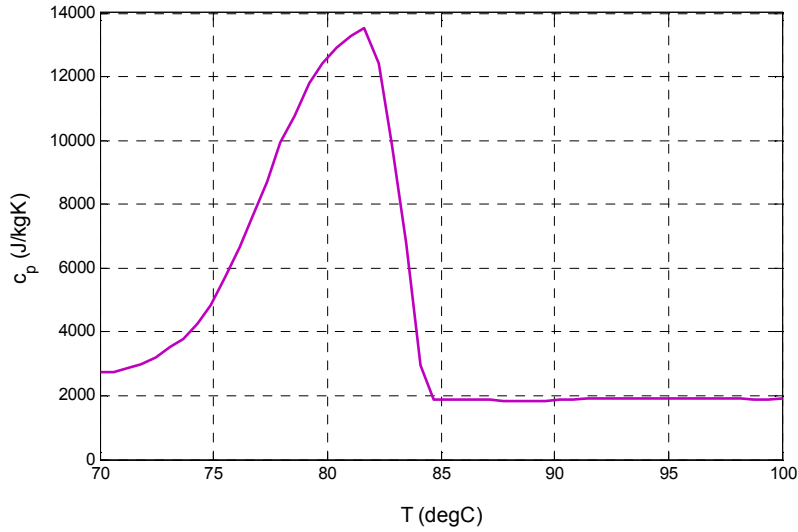


Figure 6.2: Variation of PCM specific heat during the solid-liquid phase change.

heating cycle (see Table. 6.6). In the present work, a PCM with melting temperature of $T_{peak,PCM} = 85^{\circ}C$ is selected to illustrate its effect on the drying process.

6.4 Theory

The drying process involves the evaporation of liquid moisture inside the paper sheet due to its exposure to the heated drums as well as the hot air. The different stages of drying are presented schematically in Fig. 6.3. The paper sheet is heated due to its contact to the heated cylinders from one side while it is exposed to ambient air on the other end. In the following stage and while the paper sheet is travelling to the subsequent cylinder, the sheet is exposed to ambient air from both sides. The contact heating on the subsequent cylinder is switched to the opposite end of the paper sheet while the other end is now being exposed to the ambient air.

The theoretical model presented in this section addresses the drying process across the paper sheet neglecting the lateral variation of moisture and vapor content. That in effect requires the model to be translated into the reference frame moving with the paper sheet

Schematic	Description
	Contact heating ($x=0$) & Convection ($x=\delta$)
	Convection ($x=0$) & Convection ($x= \delta$)
	Convection ($x=0$) & Contact heating ($x= \delta$)
	Convection ($x=0$) & Convection ($x= \delta$)

Figure 6.3: Schematic description of different phases during the drying process.

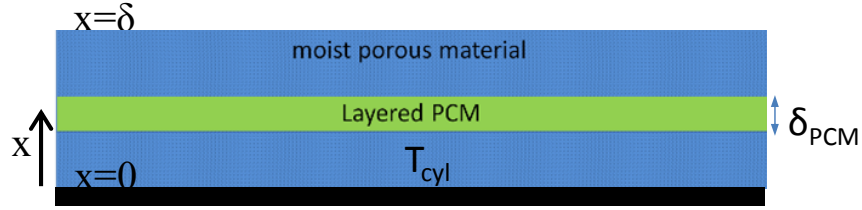


Figure 6.4: Schematic of the theoretical domain in the absence and presence of PCM layer.

along the cylinders which implies that the thermal and mass transfer boundary conditions should be represented as time-dependent parameters as illustrated schematically in Fig. 6.4. The temporal duration of each boundary condition is determined by the geometrical and operating conditions of each case as will be discussed in the boundary conditions section.

6.4.1 Governing Equations

The governing equations for the mass and energy balance through the sheet thickness are taken from [79, 86] and presented in this section. The mass balance equation is stated as:

$$\frac{\partial M}{\partial t} = -\frac{\partial J_w}{\partial x} - \frac{\partial J_v}{\partial x} \quad (6.1)$$

The transport of liquid water inside the paper sheet is modelled through Darcy's law which governs the capillary pressure distribution inside the porous moist sheet,

$$J_w = \left(\frac{K}{v_w}\right) \frac{\partial P_{ca}}{\partial x} \quad (6.2)$$

The capillary pressure, P_{ca} , is obtained from an empirical correlation developed by Spolek [87]:

$$P_{ca} = 0.84 \times 10^5 s^{-0.63} \quad (6.3)$$

where $0 < s < 1$ is the liquid saturation inside the porous medium. This correlation determines the capillary pressure in wood as a function of saturation. It was developed with consideration of both experimental data and a mechanistic model and includes an irreducible saturation level of approximately 0.1, below which liquid flow was no longer possible. An additional expression for capillary pressure in paper needs to be developed, since the porous structure of wood is not the same as the structure of paper. The transport of vapor phase inside the paper sheet is governed through Ficks law:

$$J_v = - \frac{D_{app} MW_v}{(1 - y_v)} \frac{\partial C_v}{\partial x} \quad (6.4)$$

where D_{app} is the apparent mass diffusivity of water vapor and is related to its molecular diffusivity through the following equation,

$$\frac{D_{app}}{D_v} = \frac{\Phi}{\alpha} \epsilon^m (1 - s)^n \quad (6.5)$$

where Φ/α is the ratio of the pore shape factor to the tortuosity factor. In this model, the values of Φ and n are chosen as 1 according to Han's model [80]. The values of α and m are assumed to be 1.5 [78]. The molecular diffusivity, D_v , is related to the operating temperature through,

$$D_v = A_1 \frac{T^{1.5}}{P_{atm}} \quad (6.6)$$

where $A_1 = 8.076 \times 10^{-4} (kg.m(s^3 K^{1.5}))$. The energy transfer inside the paper sheet is governed by the following energy balance equation,

$$\rho_{sh} c_{p,sh} \frac{\partial T}{\partial t} = - \frac{\partial q''}{\partial x} - \frac{\partial (J_w H_w + J_v H_v)}{\partial x} \quad (6.7)$$

where

$$q'' = -k_{sh} \frac{\partial T}{\partial x} \quad (6.8)$$

The thermal mass of the paper sheet, $\rho_{sh}c_{p,sh}$, is calculated based on the temporal and spatial distribution of liquid and vapor content as well as the properties of the dry paper sheet and its porosity.

$$\rho_{sh}c_{p,sh} = \rho_f c_{p,f}(1 - \epsilon) + \rho_w c_{p,w} s \epsilon, \quad (6.9)$$

$$k_{sh} = k_f(1 - \epsilon) + k_w s \epsilon + k_a(1 - s)\epsilon \quad (6.10)$$

here ϵ is the sheet's porosity which is assumed to be constant. In the presence of PCM layer (see Fig. 6.4), the energy equation for the PCM layer is given as:

$$\rho_{PCM} c_{p,PCM} \frac{\partial T}{\partial t} = k_{PCM} \frac{\partial^2 T}{\partial x^2} \quad (6.11)$$

At the two interfaces of the paper and PCM layer, the following condition is valid: $T_{paper} = T_{PCM}$. Note that the thermal contact resistance between the paper and PCM layer is neglected.

While the thermal conductivity of both the paper and the PCM are assumed to be constant with temperature, the specific heat of the PCM is defined as a function of temperature illustrated in Fig. 6.2 and included in the numerical code as a fourth order polynomial function of T.

6.4.2 Boundary Conditions

As discussed earlier, the one-dimensional representation of the paper sheet implies that one will have to represent its motion along the heated drums through time-dependent boundary conditions. In this section, the mass and energy transport boundary conditions

as explained by Asensio and Seyed-Yagoobi [79] are presented for each of the aforementioned processes followed by the modifications to be made to represent their temporal variations. In addition, similar to the work by Asensio and Seyed-Yagoobi [79] the moisture evaporation is represented through the following boundary condition at the two ending nodes of the paper sheet (see Fig. 6.4),

$$J_{v,o} = k_m \left(\frac{P_v - P_{va}}{P_{atm}} \right) \frac{MC(t)}{MC_{init}} \quad (6.12)$$

where the mass transfer coefficient, k_m , is determined from the Chilton-Colburn form of the Reynolds analogy [88]. The last term in Eq. 6.12 is an arbitrary factor included to represent reductions in moisture available for evaporation at the free surface during drying, since evaporation relationships available in the literature are based on the presence of a fully wetted surface. Use of an adjusted evaporation rate to reflect reductions in evaporation from the paper web during drying is similar to previous studies which forcibly decreased the sheet evaporation rate at pre-determined critical moisture content in order to simulate the falling rate period of drying. [75].

The vapor pressure, P_v , is calculated using an exponential curve fit as explained in the theoretical model by Nissan and Kaye [76]:

$$P_v = A_2 \exp(-B/T) \quad (6.13)$$

where $A_2 = 4.0309 \times 10^{10}(Pa)$ and $B = 4832.16(K)$. P_{va} is also calculated from Eq. 6.13, then multiplied by humidity ratio of the ambient air, ω_a .

The heat exchange on the heated cylinder is estimated through the thermal contact conductance equation,

$$q'' = h_i(T_{cyl} - T) \quad (6.14)$$

where the following empirical expression is used for the thermal conductance, h_i [79, 89]

$$h_i = -20.13 + 19.87 \ln(P) + 21.00/BW + 97.70\omega^2 \ln(P) - (8.54\omega^{5/4})/BW + 188.65\omega^{3/2} \quad (6.15)$$

where $0.68 < P < 328.81 kPa$, $0.084 < BW < 0.313 kg/m^2$, $4.8\% < \omega < 60\%$, and $T_{avg} = 85^\circ C$. The contact conductance increases with increasing pressure, increasing moisture levels, and decreasing sheet basis weight.

It is assumed that the temperature of the heated cylinder, T_{cyl} , remains constant due to its continuous exposure to the superheat steam. On the opposite side of the paper sheet where it is exposed to convective air flow, the following convection boundary condition is applied

$$q''_{conv} = h_a(T - T_a) \quad (6.16)$$

The convection heat transfer coefficient is estimated through turbulent flow over cylinders [90] and flat plate [91], respectively, for the portion pertinent to the paper sheet on the heated drums and traveling in between. The aforementioned boundary conditions are summarized in Tables. 6.1 and 6.2, respectively for mass transfer and energy transfer. These boundary conditions correspond to the two ends of the paper sheet as the paper travels along the heated cylinders and within the pocket-drying regions.

6.5 Numerical Technique

COMSOL 4.3 software [92] is used for the numerical modeling of the problem under study. The mathematical model to represent the governing equations and appropriate boundary conditions are incorporated in the program through the COMSOL model libraries (Transport of Diluted Species and Heat Transfer in Solids) as well as the user-defined-functions. A one dimensional, transient model to calculate the temperature and

Table 6.1: Summary of mass transfer boundary equations.

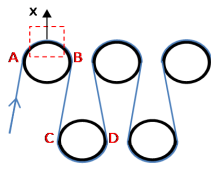
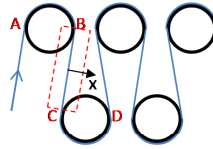
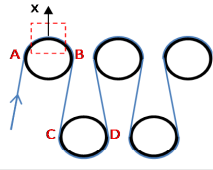
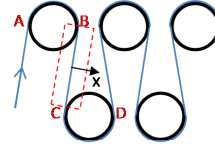
Transport property	Boundary	Contact Heating	Pocket Ventilation
			
Mass	$x = 0$	$J_v + J_w = 0$	$J_w + J_v + J_{v,o} = 0$
	$x = \delta$	$J_w + J_v - J_{v,o} = 0$	$J_w + J_v - J_{v,o} = 0$

Table 6.2: Summary of energy transfer boundary equations.

Transport property	Boundary	Contact Heating	Pocket Ventilation
			
Energy, Paper	$x = 0$	$-k_{sh} \frac{\partial T}{\partial x} + J_v H_v + J_w H_w = h_i (T_{cyl} - T)$	$-k_{sh} \frac{\partial T}{\partial x} + J_w H_w + J_{v,o} H_v = h_{\infty} (T_a - T)$
	$x = \delta$	$-k_{sh} \frac{\partial T}{\partial x} + J_w H_w - J_{v,o} H_v = h_{\infty} (T - T_a)$	$-k_{sh} \frac{\partial T}{\partial x} + J_w H_w - J_{v,o} H_v = h_{\infty} (T - T_a)$
Energy, PCM	$x = \delta_{1,PCM}$ $x = \delta_{2,PCM}$	$T = T_{PCM}$	

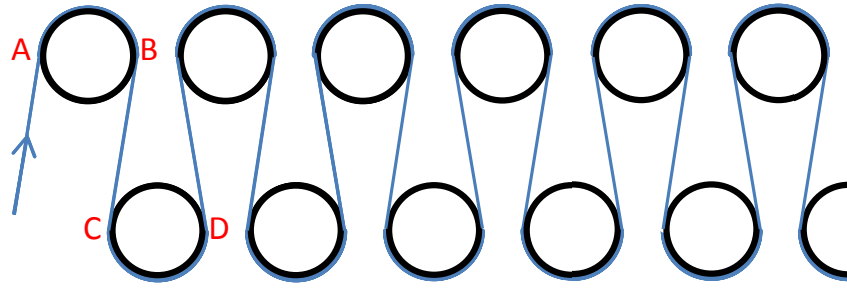


Figure 6.5: Schematic representation of drying process in the conventional heating arrangement.

moisture and vapor variation inside the paper sheet is considered.

6.6 Case Description

Conventional dryers used widely in the pulp and paper industry include a series (30-100 units) of cylindrical cast iron dryer drums. These drums are continuously heated by the superheat steam which serves as the energy required to extract the moisture from the paper sheet. In what follows, the results of paper-sheet drying under this conventional setting, hereafter referred to as Conventional Heating Arrangement is presented and compared against the case with PCM layer. The schematic representation of this arrangement is presented in Fig. 6.5

Next, a periodic heating concept is proposed and demonstrated which exploits the advantage of PCM latent heat of melting during the pocket ventilation. In the Periodic Heating Arrangement, n number of heated cylinders are followed by an extended length of paper sheet being exposed to the ambient air. The schematic of this arrangement is shown in Fig. 6.6.

The operating conditions for each of the aforementioned cases and the properties of the paper sheet and the PCM layer are summarized in Tables. 6.3 and 6.4, respectively.

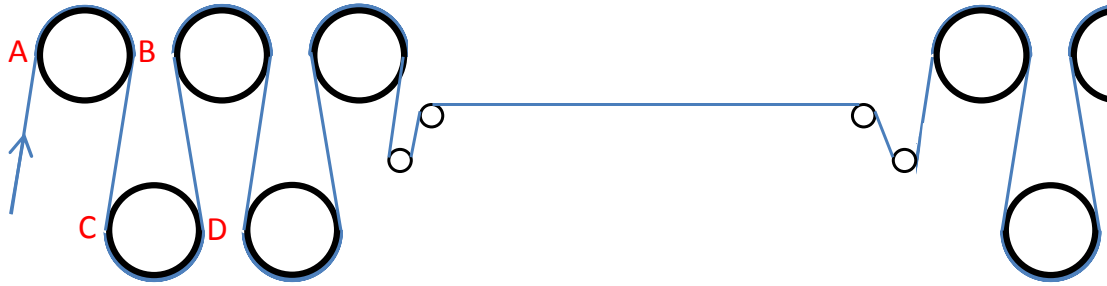


Figure 6.6: Schematic representation of drying process in the periodic heating arrangement.

Table 6.3: Summary of the operating conditions for the present case study.

Parameter	δ (mm)	δ_{PCM} (mm)	T_{cyl} (C)	T_{init} (C)	T_a (C)	$T_{peak-PCM}$ (C)	u (m/s)	L_1 (m)	L_2 (m)	BW (kg/m ³)
Value	0.5	0.15	165.6	43.3	60	85	4.630	3.030	0.940	0.300

Table 6.4: Summary of the properties for the present case study.

Material	ρ (kg/m ³)	c_p (J/kgK)	k (W/mK)
Paper	600	1340	0.09 (fiber)
PCM Layer	870 (Solid) 760 (Liquid)	see Fig.6.2	0.20

6.7 Results and Discussions

6.7.1 Conventional Heating Arrangement

As described earlier, in the conventional arrangement of paper-drying, the paper sheet undergoes a continuous series of heating cylinders and pocket ventilation processes. In this setting, every heated cylinder is followed by a duration of pocket ventilation with the corresponding times obtained from the operating velocity and the length of each phase (see Table. 6.3). Figure 6.7 illustrates the variation of the sheet temperature and moisture content in the presence and absence of PCM layer. The amount of heat to the paper sheet depends on the value of the thermal contact conductance heating given in Eq. 6.15 which is related to the moisture content of the paper sheet. Therefore, with the variation of the moisture content in the paper sheet, as the paper sheet gets dryer in the process, the energy transfer decreases in magnitude. As a result, the temperature decreases at the last stages of drying process. It is observed that under this set of operating conditions, the difference between the moisture content of the two cases of paper with and without PCM is not significant. Therefore, no potential benefit could be obtained by using the PCM layer. The slight increase in moisture content at the early stages of the drying process ($Cyl < 3$), is due to the condensation of the initial vapor content in the paper sheet since its initial temperature, T_{init} , is lower than the ambient temperature.

The variation of temperature and moisture profiles across the paper sheet thickness for select cylinders is presented in Figs. 6.8 and 6.9, respectively. In addition, the figures present the evolution of temperature and moisture content as the sheet travels from the heated cylinders (i.e. point A to point B on each cylinder, see Fig. 6.5) to the pocket ventilation section (i.e. point C to point D). Note that the presented x-axis on these plots only corresponds to the plain paper material and the PCM section is not shown here since there is no mass transfer in the region of PCM layer. For the cases representing the paper

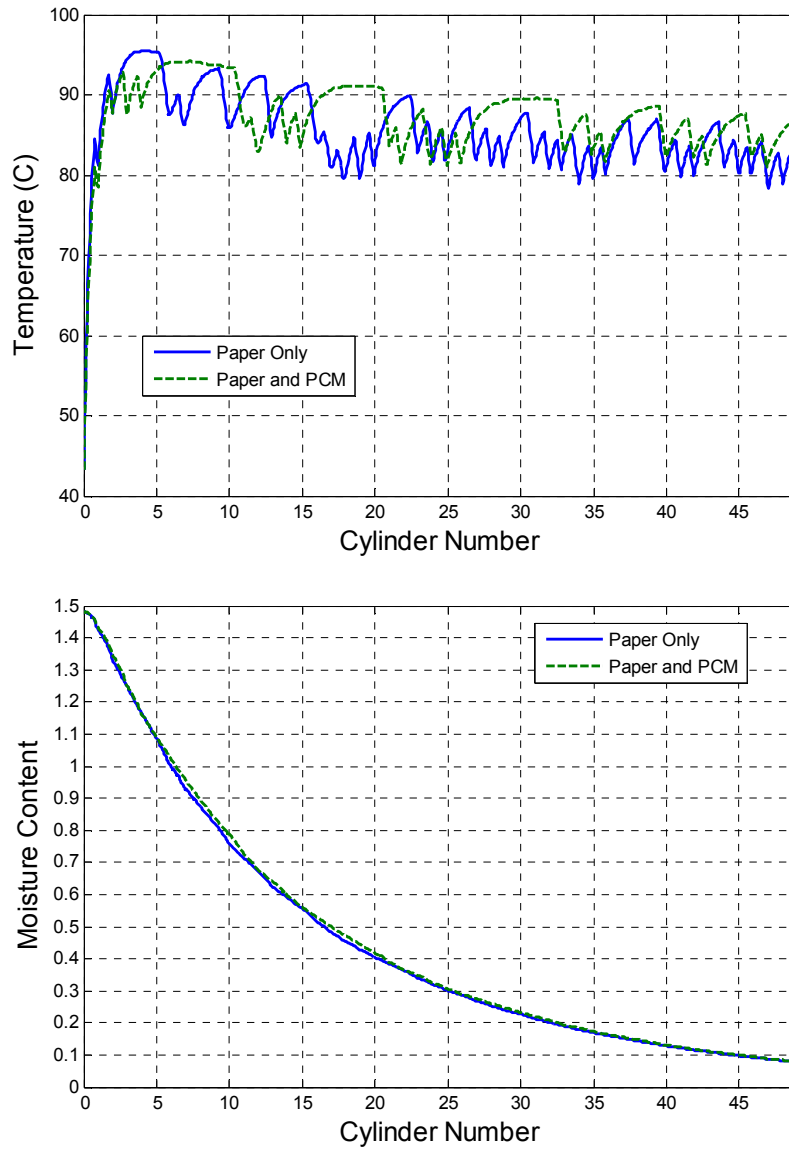


Figure 6.7: Time evolution of paper sheet average temperature (top) and moisture content (bottom) in the presence and absence of PCM layer for conventional heating arrangement.

Table 6.5: Correspondence of the cylinder numbers in the two heating arrangements.

Conventional Arrangement	1	2	3	4	5	6	7	8	9	10	11	12	13	14	15	16	17	18	19	20	21
Periodic Arrangement	1	2	3	4	5	-	-	-	-	-	-	-	6	7	8	9	10	-	-	-	-
Conventional Arrangement	22	23	24	25	26	27	28	29	30	31	32	33	34	35	36	37	38	39	40	41	42
Periodic Arrangement	-	-	-	11	12	13	14	15	-	-	-	-	-	-	-	16	17	18	19	20	-

being in A and B positions (i.e. Fig. 6.8-left), the difference in sheet temperature between the cases with and without PCM layer is more pronounced on the sheet surface exposed to the ambient air. In these cases, the temperature difference is minimum on the side in contact with the heated cylinder. The temperature difference between the contact side and the side exposed to the ambient air for each case depends on the location (Cyl number) where the paper sheet is traveling on. The larger temperature difference on the convection side implies that the contribution of the excess thermal mass raised by the presence of the PCM layer is maximum on the convection side where the tendency of the paper sheet to lose energy to the ambient is suppressed by the presence of the PCM layer.

6.7.2 Periodic Heating Arrangement

The variation of temperature and moisture content for the periodic heating arrangement is presented in Fig. 6.10. As mentioned before, the paper sheet goes through the heating process over the first 5 cylinders followed by an extended length of pocket ventilation which is equal to the time if the paper sheet had to pass over additional 7 cylinders. Table. 6.5 shows the correspondence of the cylinder numbers in the periodic heating arrangement with that of the conventional heating arrangement. It is observed that during the heating period (e.g. $1 < Cyl < 5$), the temperature rise is higher for the case of paper with PCM layer. At this stage, the PCM layer absorbs the heat required for its phase change since the temperature of the paper is in the vicinity of the melting point of the PCM layer. Therefore, the whole paper-PCM material exhibits higher heat gain capacitance which

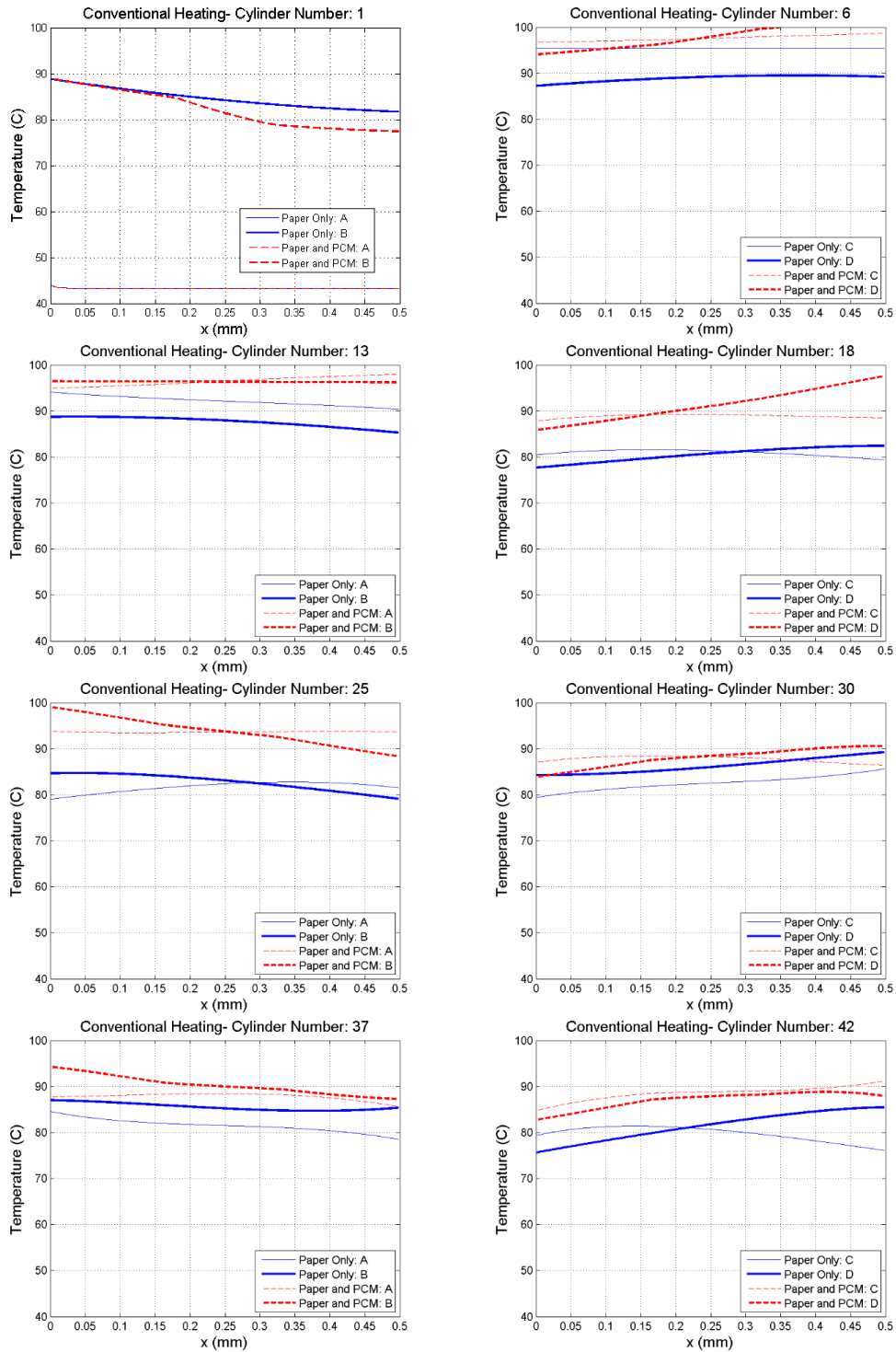


Figure 6.8: Temperature profiles across the paper sheet in the presence and absence of PCM layer for different points during the drying process for conventional heating arrangement.

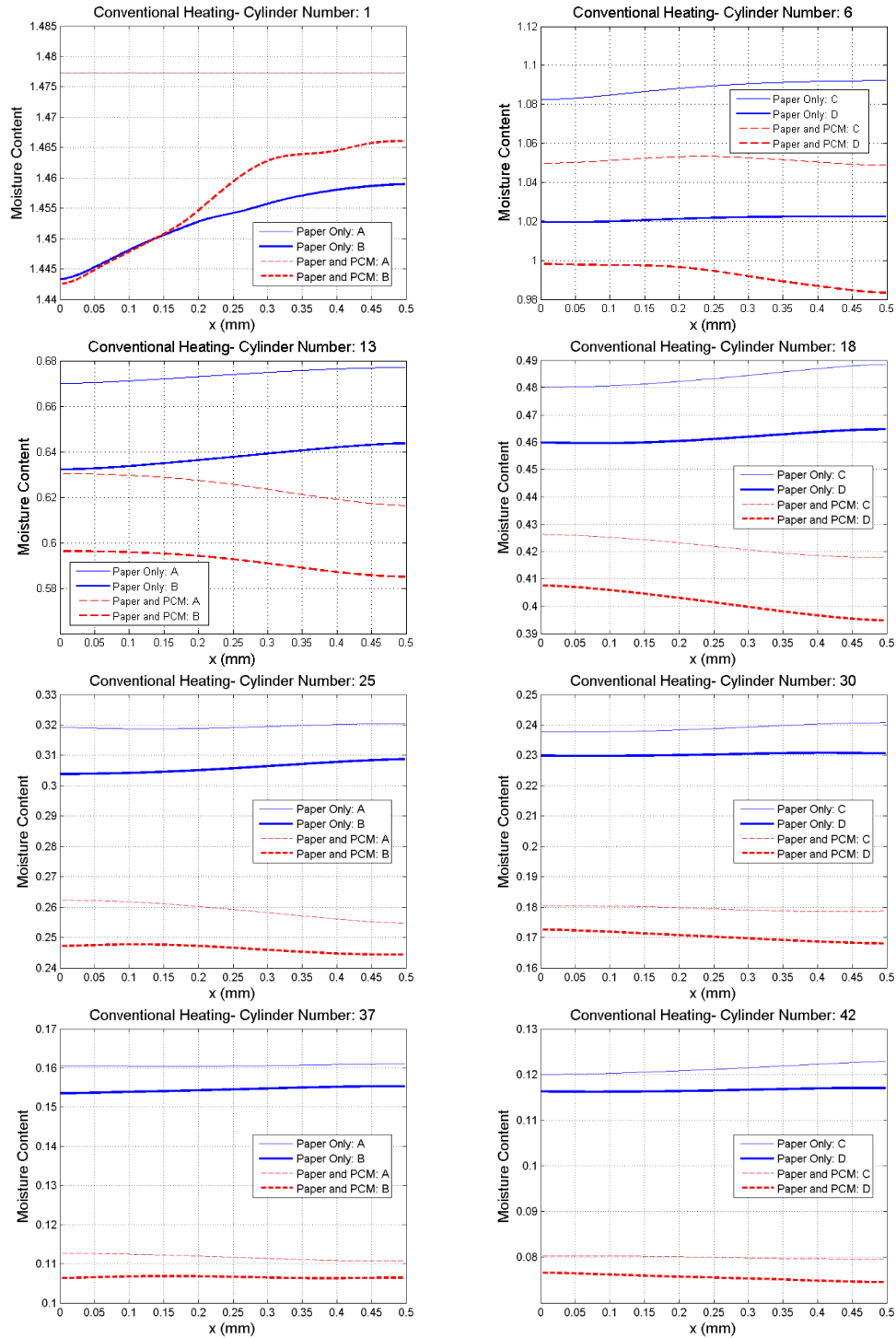


Figure 6.9: Moisture content profiles across the paper sheet in the presence and absence of PCM layer for different points during the drying process for conventional heating arrangement.

ultimately results in the temperature increase of the paper sheet compared to that of without PCM layer. Also, during the pocket ventilation the case with PCM layer encounters a slower decline of temperature so as to approach temperatures that are higher than the paper-only counterpart at the end of pocket ventilation cycle. This is attributed to the release of latent heat during solidification of the PCM layer (i.e. acting as a heat source). Higher rates of evaporation results in the reduction of the sheet temperature especially at the outer surface of the paper sheet which is adjacent to the ambient air. In the presence of the PCM layer in the paper sheet; however, due to the existence of heat source (i.e. PCM layer acting as source of energy), despite high evaporation rate, the sheet average temperature stays above that of plain paper. As the result of this delay in the temperature drop, the sheet temperature in the presence of PCM remains superior to that of paper-only case which is the primary reason for a faster drop of the moisture content in the paper sheet (Fig. 6.10b). When the paper sheet reaches the end of each period (end of its cooling cycle), the cooling effect of the ambient air prevails the heating provided by the heated cylinder which results in the continuous decline of the temperature until it reaches the ambient air temperature, $T_a = 60^\circ C$. At this point, the cooling performance by the ambient air becomes effectively zero ($T - T_a \approx 0$) and the sheet temperature resumes its ascend as the heating cycles begins. This is an indication of the long pocket ventilation which obviously is not desired. Therefore, for a more effective drying process, the length of the pocket ventilation should be optimized to avoid reaching the ambient air temperature at the end of the pocket ventilation. In summary, in the periodic heating arrangement, where the paper-sheet is exposed to an extended unheated period, the case with no PCM is more susceptible to a decline of temperature and eventual reduction in drying efficiency. As the result of higher overall temperature, the paper sheet with PCM layer encounters a more dramatic reduction in its moisture content over time. At the end of the drying process the moisture removal efficiency is improved by 15%. Such an increase in moisture removal

difference between the plain paper and the paper with PCM layer has a significant impact on the paper drying process.

Figures 6.11 and 6.12 present the evolution of temperature and moisture profiles in the paper thickness direction as the sheet travels on select dryer drums. As the paper sheet travels from point A to point B, an increase in the average temperature of the paper sheet is observed. The relatively higher temperature values of the paper with PCM compared to the plain paper counterparts are due to the ability of the PCM layer in absorbing heat during the heating cycles and storing the energy at the longer duration of time. The temperature difference between the cases of with and without PCM is minimum on the side in contact with the heated cylinder. However, due to the presence of the PCM layer, larger temperature difference on the convection side ($x = \delta$) occurs which prevents the paper sheet to lose heat to the ambient and reduction of its temperature.

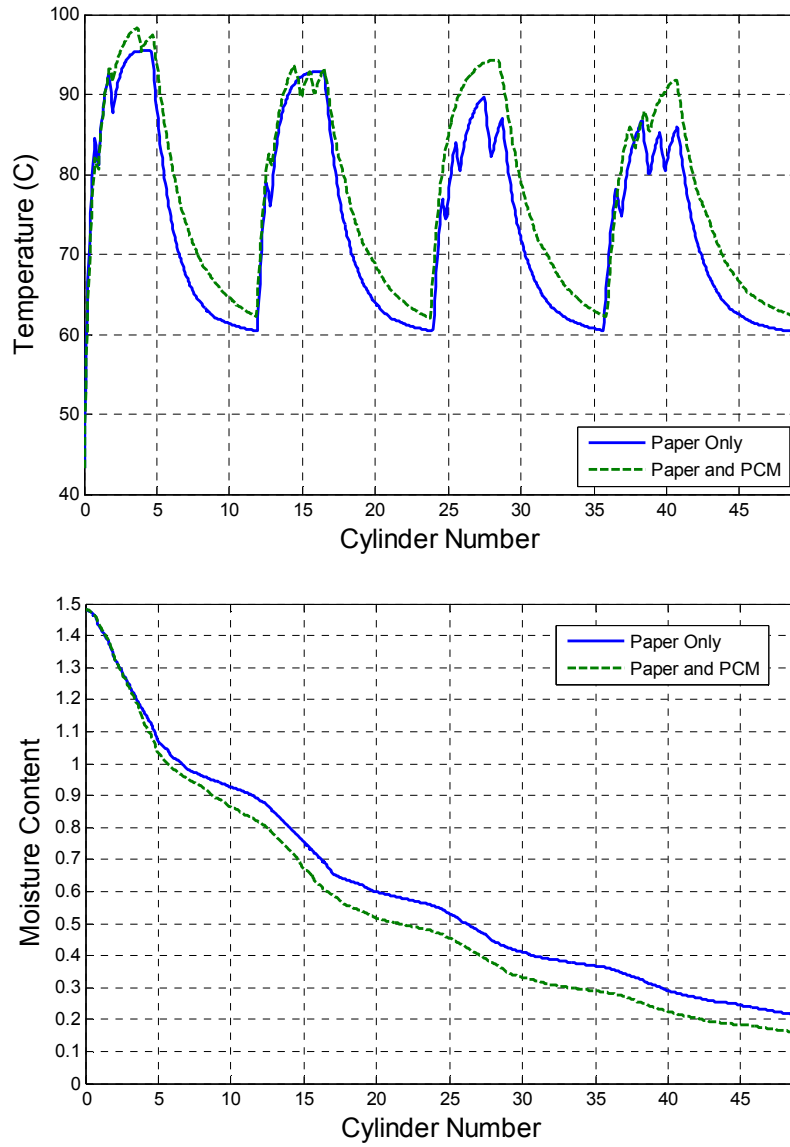


Figure 6.10: Time evolution of paper sheet average temperature (top) and moisture content (bottom) in the presence and absence of PCM layer for periodic heating arrangement.

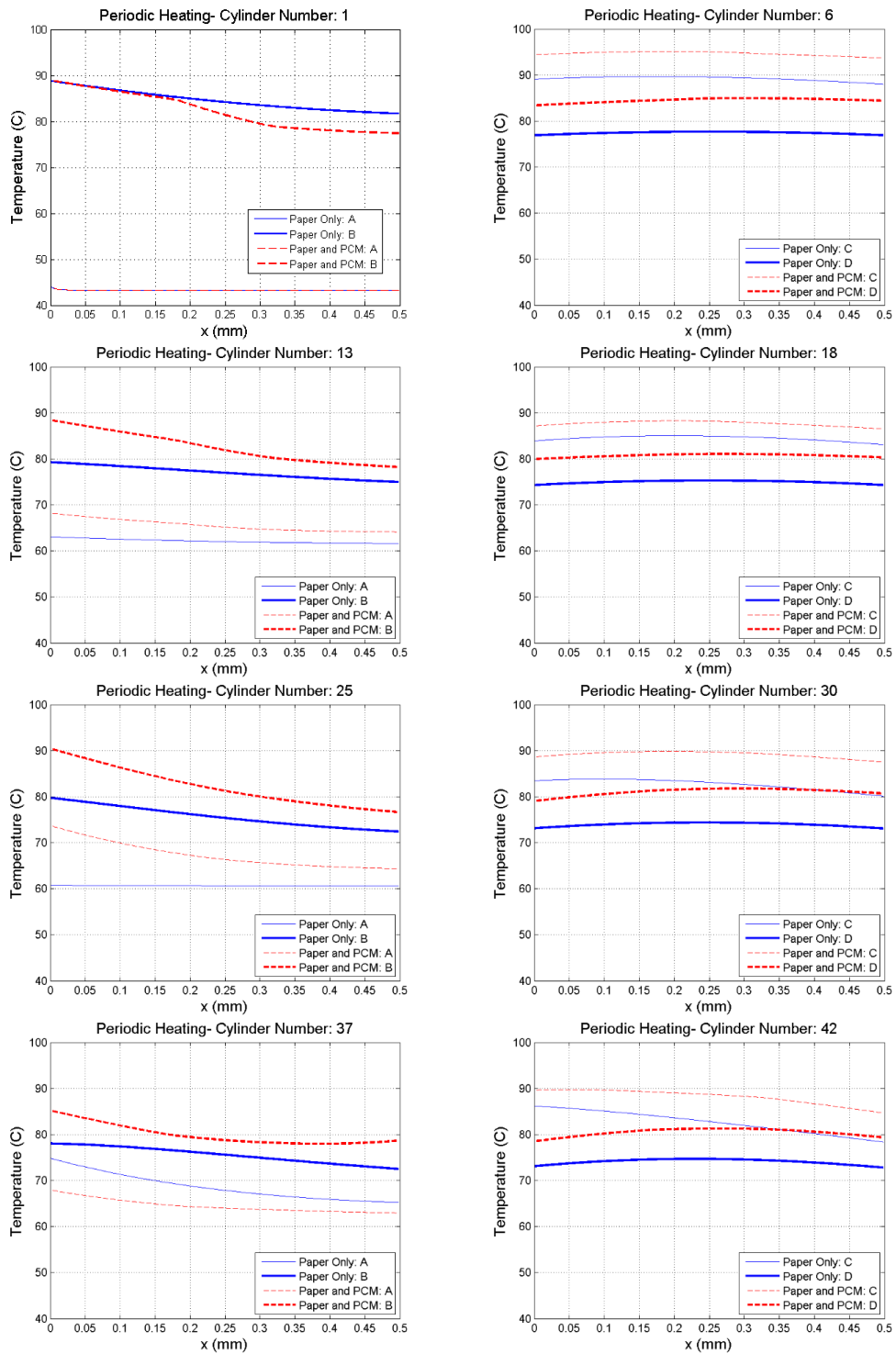


Figure 6.11: Temperature profiles across the paper sheet in the presence and absence of PCM layer for different points during the drying process for periodic heating arrangement.

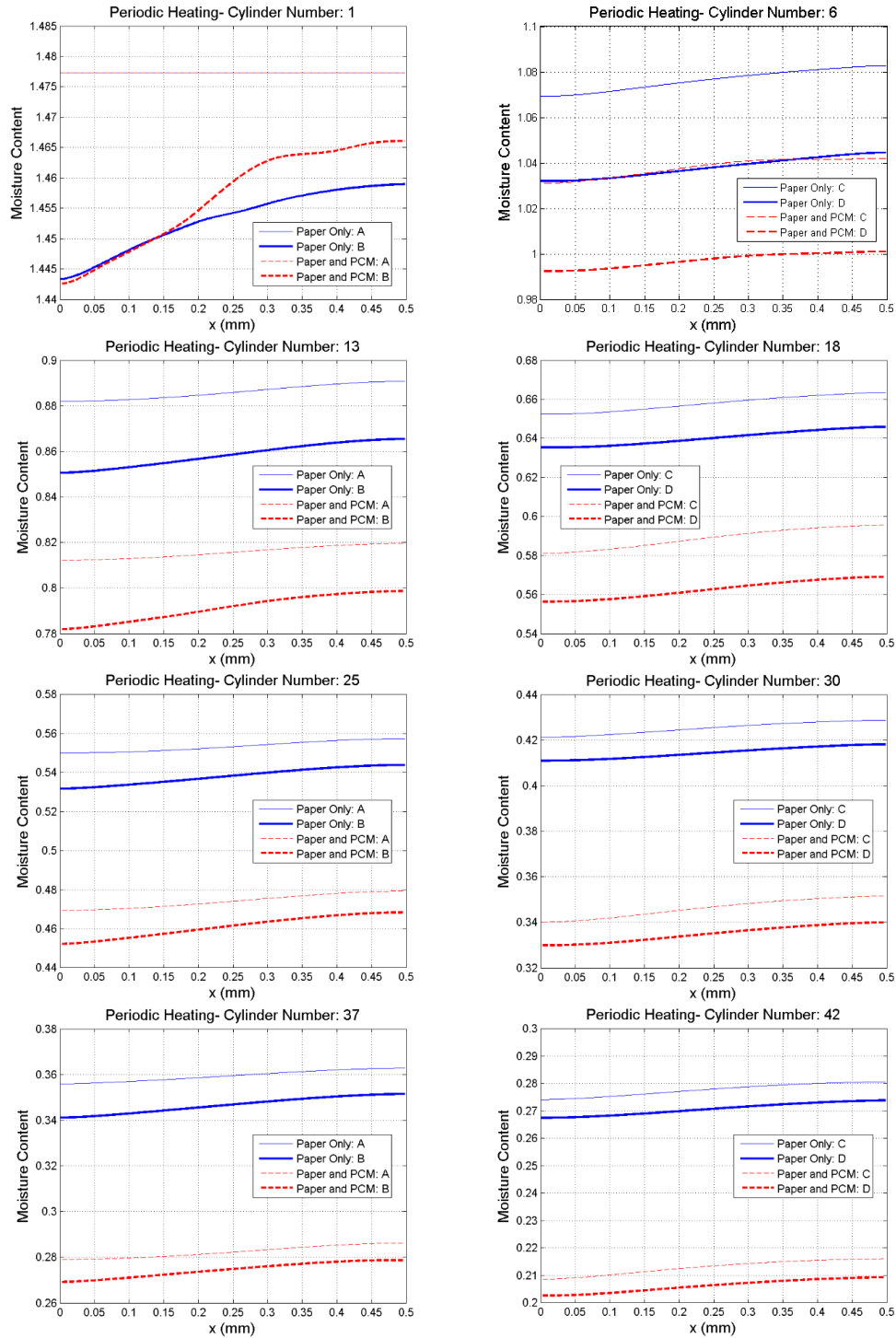


Figure 6.12: Moisture content profiles across the paper sheet in the presence and absence of PCM layer for different points during the drying process for periodic heating heating arrangement.

6.8 Conclusions

In this study, the transport characteristics associated with the drying process of a paper sheet in the presence and absence of a layer of phase change material (PCM) was investigated. The numerical solution of the mathematical model provides the moisture and temperature profiles within the paper sheet thickness in the presence and absence of PCM. Two different arrangements of the heated cylinders and air ventilation pockets have been introduced. The results demonstrate that drying can be enhanced by introducing PCM layer to improve moisture removal from the porous paper sheet. Further study is needed to understand the combined effects of operating parameters and PCM properties on the extent of enhancement and optimization of drying.

Chapter 7

Conclusions and Recommendations

7.1 Conclusions

Fundamental study of heat and mass transfer enhancement using phase change materials (PCM) in terms of microencapsulated as well as layered PCM and in the single-component or multi-component was accomplished. To that effect, numerical and experimental investigations were conducted to explore the role of using PCM on heat and mass transfer characteristics of multi-scale applications involving single-phase and two-phase flow phenomena. Below is the summary of the accomplishments:

- Single-phase Microtube flow: Mathematical formulation was developed for multi-component blend of MEPCM and then applied to study the heat transfer characteristics of MEPCM slurry flow in a microtube. The role of various parameters, including particle diameter and MEPCM concentration on the level of heat transfer enhancement was studied and physically analyzed. It was shown that although the blend slurry showed locally higher heat transfer coefficient compared to each of the single slurry cases, its overall heat transfer enhancement falls between the ones provided by either of the single-component slurry counterpart.

- Single-phase natural convection flow: Mathematical model was developed to account for density variation of the slurry due to the phase change of MEPCM and incorporated into the numerical model. The numerical model was validated against experimental measurements of heat transfer characteristics of buoyancy driven flow in an enclosure over a range of operating conditions. The heat transfer performance of the flow in the presence and absence of MEPCM particles was physically discussed.
- Two-phase liquid film flow with evaporation: The mathematical formulation for evaporating liquid film flow was developed to account for the presence of MEPCM particles. Significant evaporation heat transfer enhancement was demonstrated by using MEPCM which could potentially result in the delay in dry-out in liquid film evaporation region.
- Drying of paper sheet: The mathematical model for drying process for a paper sheet of a certain thickness in the presence of layered PCM was developed and numerically solved over a range of practical operating conditions. The results demonstrate that drying can be enhanced by introducing PCM layer and improve moisture removal from the porous medium of the paper sheet. In addition, a new drying arrangement is proposed which takes advantage of the latent heat provided by the presence of PCM so as to reduce the number of heating cycles over a certain time.

7.2 Recommendations

While the application of blend of MEPCM particles was demonstrated for single-phase liquid flow, its use for two-phase evaporating liquid film can provide additional benefits due to a wider range of enhanced thermal mass raised by the presence of MEPCM particles. The tunability of the melting range of MEPCM particles and its impact on

evaporation heat transfer performance can, therefore, be a subject of further research. In addition, the thermal and flow characteristics of naturally induced flow in the presence of multi-component MEPCM particles could be explored. Furthermore, the model developed for the drying process of paper sheet in the presence of layered PCM can be used to study alternative and novel arrangements to optimize the drying efficiency over a wide range of operating condition. Moreover, it is worth performing an in depth parametric study of drying using different PCM materials. There is a wide perspective for the potential use of PCM in enhancement of drying processes. The advantage of using PCM, either in the layered form or dispersed particles can be extended to different applications such as pharmaceutical, food, clothing and textile industries for optimized energy consumption. Thus, the model can be applied to study other applications relevant to the removal of moisture from porous medium.

Bibliography

- [1] Microtek Laboratories, I. How do pcms work?
- [2] Sinha-Ray, S., Sahu, R. P., and Yarin, A. L., 2011. “Nano-encapsulated smart tunable phase change materials”. *Soft Matter*, **7**, pp. 8823–8827.
- [3] Faghri, A., and Zhang, Y., 2006. *Transport phenomena in multiphase systems*. Academic Press.
- [4] PureTemp, 2014. Puretemp llc.
- [5] Lane, G. A., 1980. “Low temperature heat storage with phase change materials”. *International Journal of Ambient Energy*, **1**(3), pp. 155–168.
- [6] Sabbah, R., 2008. “Numerical and experimental investigation of heat transfer characteristics of liquid flow with micro-encapsulated phase change material”. PhD thesis, Illinois Institute of Technology, Chicago, IL.
- [7] Farid, M. M., Khudhair, A. M., Razack, S. A. K., and Al-Hallaj, S., 2004. “A review on phase change energy storage: materials and applications”. *Energy conversion and management*, **45**(9), pp. 1597–1615.
- [8] Farid, M., and Mohamed, A., 1987. “Effect of natural convection on the process of melting and solidification of paraffin wax”. *Chemical engineering communications*, **57**(1-6), pp. 297–316.

- [9] Farid, M. M., and Kanzawa, A., 1989. “Thermal performance of a heat storage module using pcms with different melting temperatures: mathematical modeling”. *Journal of solar energy engineering*, **111**(2), pp. 152–157.
- [10] Farid, M. M., and Husian, R. M., 1990. “An electrical storage heater using the phase-change method of heat storage”. *Energy Conversion and Management*, **30**(3), pp. 219–230.
- [11] Hasnain, S., 1998. “Review on sustainable thermal energy storage technologies, part i: heat storage materials and techniques”. *Energy Conversion and Management*, **39**(11), pp. 1127–1138.
- [12] Sahan, N., and Paksoy, H. O., 2014. “Thermal enhancement of paraffin as a phase change material with nanomagnetite”. *Solar Energy Materials and Solar Cells*, **126**(0), pp. 56 – 61.
- [13] Dincer, I., and Rosen, M., 2002. *Thermal energy storage: systems and applications*. John Wiley & Sons.
- [14] Garg, H., Mullick, S., and Bhargava, A., 1985. *Solar thermal energy storage*. Springer.
- [15] Gschwander, S., Schossig, P., and Henning, H.-M., 2005. “Micro-encapsulated paraffin in phase-change slurries”. *Solar Energy Materials and Solar Cells*, **89**(2), pp. 307–315.
- [16] Yang, R., Xu, H., and Zhang, Y., 2003. “Preparation, physical property and thermal physical property of phase change microcapsule slurry and phase change emulsion”. *Solar energy materials and solar cells*, **80**(4), pp. 405–416.

- [17] Lane, G., and Rossow, H., 1976. "Encapsulation of heat of fusion storage materials". In Proceedings of 2nd southeastern conference on application of solar energy, pp. 442–50.
- [18] Lane, G. A., 1980. "Low temperature heat storage with phase change materials". *International Journal of Ambient Energy*, **1**(3), pp. 155–168.
- [19] Stark, P., 1990. "Pcm-impregnated polymer microcomposites for thermal energy storage". In SAE, 20th Intersociety Conference on Environmental Systems, Vol. 1.
- [20] Royon, L., Guiffant, G., and Flaud, P., 1997. "Investigation of heat transfer in a polymeric phase change material for low level heat storage". *Energy conversion and management*, **38**(6), pp. 517–524.
- [21] Hong, Y., and Xin-shi, G., 2000. "Preparation of polyethylene–paraffin compound as a form-stable solid-liquid phase change material". *Solar Energy Materials and Solar Cells*, **64**(1), pp. 37–44.
- [22] Zalba, B., Marin, J. M., Cabeza, L. F., and Mehling, H., 2003. "Review on thermal energy storage with phase change: materials, heat transfer analysis and applications". *Applied thermal engineering*, **23**(3), pp. 251–283.
- [23] Kimura, H., and Kai, J., 1984. "Phase change stability of $\text{CaCl}_2 \cdot 6\text{H}_2\text{O}$ ". *Solar Energy*, **33**(6), pp. 557 – 563.
- [24] Gibbs, B., and Hasnain, S., 1995. "Dsc study of technical grade phase change heat storage materials for solar heating applications". *Solar Engineering*, pp. 1053–1053.
- [25] Porisini, F. C., 1988. "Salt hydrates used for latent heat storage: corrosion of metals and reliability of thermal performance". *Solar Energy*, **41**(2), pp. 193–197.

- [26] Khudhair, A., Farid, M., Ozkan, N., and Chen, J., 2002. "Thermal performance and mechanical testing of gypsum wallboards with latent heat storage". In International Conference and 4th Experts Meeting on Thermal Energy Storage Technologies.
- [27] Sengupta, S., 1991. Microencapsulated phase change material slurry heat sinks. US Patent 5,007,478.
- [28] Colvin, D. P., and Bryant, Y. G., 1998. "Protective clothing containing encapsulated phase change materials". *ASME Heat Transfer Div Publ HTD*, **362**, pp. 123–132.
- [29] Colvin, D. P., and Mulligan, J. C., 1986. Spacecraft heat rejection methods: Active and passive heat transfer for electronic systems-phase i. Tech. Rep. AFWAL-TR-3074, U.S. Air Force Wright Aeronautical Labs, Dayton, OH.
- [30] Colvin, D. P., and Mulligan, J. C., 1987. Microencapsulated phase change for storage of heat. Tech. Rep. MFSA-27198, NASA George C. Marshall Space Flight Center, Huntsville, AL.
- [31] Goel, M., Roy, S., and Sengupta, S., 1994. "Laminar forced convection heat transfer in microcapsulated phase change material suspensions". *International Journal of Heat and Mass Transfer*, **37**(4), pp. 593 – 604.
- [32] Inaba, H., Kim, M., and Horibe, A., 2004. "Melting heat transfer characteristics of microencapsulated phase change material slurries with plural microcapsules having different diameters". *ASME Journal of Heat Transfer*, **126**, p. 558.
- [33] Alvarado, J. L., Marsh, C., Sohn, C., Phetteplace, G., and Newell, T., 2007. "Thermal performance of microencapsulated phase change material slurry in turbulent flow under constant heat flux". *International Journal of Heat and Mass Transfer*, **50**(910), pp. 1938 – 1952.

- [34] Wang, X., Niu, J., Li, Y., Zhang, Y., Wang, X., Chen, B., Zeng, R., and Song, Q., 2008. “Heat transfer of microencapsulated {PCM} slurry flow in a circular tube”. *AIChE Journal*, **54**(4), pp. 1110–1120.
- [35] Zhao, Z., Hao, R., and Shi, Y., 2008. “Parametric analysis of enhanced heat transfer for laminar flow of microencapsulated phase change suspension in a circular tube with constant wall temperature”. *Heat Transfer Engineering*, **29**(1), pp. 97–106.
- [36] Sabbah, R., Farid, M. M., and Al-Hallaj, S., 2009. “Micro-channel heat sink with slurry of water with micro-encapsulated phase change material: 3d-numerical study”. *Applied Thermal Engineering*, **29**(23), pp. 445 – 454.
- [37] Sabbah, R., Seyed-Yagoobi, J., and Al-Hallaj, S., 2011. “Heat transfer characteristics of liquid flow with micro-encapsulated phase change material: Numerical study”. *ASME Journal of Heat Transfer*, **133**(12), p. 121702.
- [38] Sabbah, R., Seyed-Yagoobi, J., and Al-Hallaj, S., 2012. “Heat transfer characteristics of liquid flow with micro-encapsulated phase change materials: Experimental study”. *ASME Journal of Heat Transfer*, **134**, p. 044501.
- [39] Kuravi, S., Du, J., and Chow, L. C., 2010. “Encapsulated phase change material slurry flow in manifold microchannels”. *Journal of Thermophysics and Heat Transfer*, **24**(2), pp. 364–373.
- [40] Hao, Y. L., and Tao, Y. X., 2004. “A numerical model for phase-change suspension flow in microchannels”. *Numerical Heat Transfer, Part A: Applications*, **46**(1), pp. 55–77.
- [41] Xing, K. Q., Tao, Y. X., and Hao, Y. L., 2004. “Performance evaluation of liquid flow with {NPCM} in microchannels”. *ASME Conference Proceedings*, **2004**(46938), pp. 283–292.

- [42] Roy, S. K., and Sengupta, S., 1991. “An evaluation of phase change microcapsules for use in enhanced heat transfer fluids”. *International Communications in Heat and Mass Transfer*, **18**(4), pp. 495 – 507.
- [43] Guyer, E. C., and Brownell, D. L., 1999. *Handbook of applied thermal design*. CRC Press LLC.
- [44] Maxwell, J. C., 1881. *A Treatise on Electricity and Magnetism*, 3 ed. Oxford University, Dover, NY.
- [45] Vand, V., 1945. “Theory of viscosity of concentrated suspensions”. *Nature (London)*, **155**, pp. 364–365.
- [46] Leal, L. G., 1973. “On the effective conductivity of a dilute suspension of spherical drops in the limit of low particle pecelet number”. *Chemical Engineering Communications*, **1**(1), pp. 21–31.
- [47] Nir, A., and Acrivos, A., 1976. “The effective thermal conductivity of sheared suspensions”. *Journal of Fluid Mechanics*, **78**(01), pp. 33–48.
- [48] Sabbah, R., Seyed-Yagoobi, J., and Al-Hallaj, S., 2012. “Natural convection with micro-encapsulated phase change material”. *ASME Journal of Heat Transfer*, **134**(8), p. 082503.
- [49] ANSYS INC., 2008. *FLUENT V12.0 User’s Guide*. Lebanon, NH.
- [50] Kuravi, S., Kota, K. M., Du, J., and Chow, L. C., 2009. “Numerical investigation of flow and heat transfer performance of nano-encapsulated phase change material slurry in microchannels”. *ASME Journal of Heat Transfer*, **131**(6), p. 062901.

- [51] Thome, J., Groll, M., and Mertz, R., 2003. *Heat transfer and fluid flows in microchannels, Heat Exchanger design update*, Vol. 2. Begell House, New York, ch. Heat Transfer and Fluid Flow in Microchannels.
- [52] Kandlikar, S., 2001. *Compact Heat Exchangers and Enhancement Technology for the Process Industries*. Begell House, New York, ch. Two-phase flow patterns, pressure drop and heat transfer during boiling in minichannel and microchannel flow passages of compact heat exchangers, pp. 319–334.
- [53] Bergles, A. E., Lienhard V, J. H., Kendall, G. E., and Griffith, P., 2003. “Boiling and evaporation in small diameter channels”. *Heat Transfer Engineering*, **24**(1), pp. 18–40.
- [54] Thome, J., Dupont, V., and Jacobi, A., 2004. “Heat transfer model for evaporation in microchannels. part i: presentation of the model”. *International Journal of Heat and Mass Transfer*, **47**(1416), pp. 3375 – 3385.
- [55] Mehendale, S., and Jacobi, A., 2000. Evaporative heat transfer in mesoscale heat exchangers. Tech. rep., Univ. of Illinois, Urbana, IL (US).
- [56] Jacobi, A. M., and Thome, J. R., 2002. “Heat transfer model for evaporation of elongated bubble flows in microchannels”. *ASME Journal of Heat Transfer*, **124**(6), p. 1131.
- [57] Lakehal, D., Meier, M., and Fulgosi, M., 2002. “Interface tracking towards the direct simulation of heat and mass transfer in multiphase flows”. *International Journal of Heat and Fluid Flow*, **23**(3), pp. 242–257.
- [58] Zhao, J. J., Duan, Y. Y., Wang, X. D., and Wang, B. X., 2011. “Effect of nanofluids on thin film evaporation in microchannels”. *Journal of Nanoparticle Research*, **13**(10), pp. 5033–5047.

- [59] Charunyakorn, P., Sengupta, S., and Roy, S., 1991. “Forced convection heat transfer in microencapsulated phase change material slurries: flow in circular ducts”. *International Journal of Heat and Mass Transfer*, **34**(3), pp. 819 – 833.
- [60] Sanchez-Silva, L., Rodriguez, J. F., Romero, A., Borreguero, A. M., Carmona, M., and Snchez, P., 2010. “Microencapsulation of {PCMs} with a styrene-methyl methacrylate copolymer shell by suspension-like polymerisation”. *Chemical Engineering Journal*, **157**(1), pp. 216 – 222.
- [61] Dupont {ISCEON 39TC(R-423A)}: Technical information.
- [62] Snchez Silva, L., Rodriguez, J. F., Carmona, M., Romero, A., and Snchez, P., 2011. “Thermal and morphological stability of polystyrene microcapsules containing phase-change materials”. *Journal of Applied Polymer Science*, **120**(1), pp. 291–297.
- [63] Carey, V., 1992. *Vapor-Liquid Phase Change Phenomena: An Introduction to the Thermophysics of Vaporization and Condensation Processes in Heat Transfer Equipment*. Hemisphere Publishing, New York, NY.
- [64] Horibe, A., Shimoyama, R., Haruki, N., and Sanada, A., 2012. “Experimental study of flow and heat transfer characteristics of natural convection in an enclosure with horizontal parallel heated plates”. *International Journal of Heat and Mass Transfer*, **55**(23-24), pp. 7072 – 7078.
- [65] Andreozzi, A., Buonomo, B., and Manca, O., 2009. “Transient natural convection in vertical channels symmetrically heated at uniform heat flux”. *Numerical Heat Transfer, Part A: Applications*, **55**(5), pp. 409–431.

- [66] Inaba, H., Dai, C., and Horibe, A., 2004. “The Convective Instability in a Microemulsion Phase-Change-Material Slurry Layer”. *JSME International Journal Series B*, **47**, pp. 126–137.
- [67] Omari, K. E., Kousksou, T., and Guer, Y. L., 2011. “Impact of shape of container on natural convection and melting inside enclosures used for passive cooling of electronic devices”. *Applied Thermal Engineering*, **31**(14-15), pp. 3022 – 3035.
- [68] Khakpour, Y., and Seyed-Yagoobi, J., 2012. “Transport characteristics of liquid flow with blend of micro-encapsulated phase change material: Numerical study”. In Proceedings of IMECE2012, ASME, ed.
- [69] Bell, D., Seyed-Yagoobi, J., and Fletcher, L., 1994. “Recent developments in paper drying”. *Advances in Drying. Washington DC: Hemisphere Publ. Corp*, **5**.
- [70] Kudra, T., 2004. “Energy aspects in drying”. *Drying Technology*, **22**(5), pp. 917–932.
- [71] Ghosh, A. K. “Fundamentals of paper drying–theory and application from industrial perspective”. *Principal, AKG Process Consulting*, **33**.
- [72] Martin, N., Anglani, N., Einstein, D., Khrushch, M., Worrell, E., and Price, L., 2000. “Opportunities to improve energy efficiency and reduce greenhouse gas emissions in the us pulp and paper industry”.
- [73] Mujumdar, A. S., 2006. *Handbook of industrial drying*. CRC Press.
- [74] Sadeghi, M., and Douglas, W. M., 2004. “From tissue to linerboard: validation of a microscale simulator for single technique and hybrid dryers”. In Proceedings of the 14th International Drying Symposium, vol. A, Sao Paulo, Brazil, pp. 444–451.

- [75] Kirk, L., and Mujumdar, A., 1984. "A literature review of computer simulation and paper drying". *Advances in Drying*, **3**, pp. 1–37.
- [76] Nissan, A., and Kaye, W., 1955. "An analytical approach to the problem of drying of thin fibrous sheets on multicylinder machines". *Tappi Journal*, **38**(7), pp. 385–398.
- [77] Lampinen, M., and Toivonen, K., 1984. "Application of a thermodynamic theory to determine capillary pressure and other fundamental material properties affecting the drying process". In *Drying84 Conference Proceedings*, p. 228.
- [78] Asensio, M., and Seyed-Yagoobi, J., 1992. "Further analysis of heat and mass transfer in a paper sheet during drying". *ASME-PUBLICATIONS-HTD*, **193**, pp. 123–123.
- [79] Asensio, M., and Seyed-Yagoobi, J., 1993. "Simulation of paper-drying systems with incorporation of an experimental drum/paper thermal contact conductance relationship". *Journal of energy resources technology*, **115**(4), pp. 291–300.
- [80] Han, S., 1970. "Drying of paper". *Tappi*, **53**(6), p. 1034.
- [81] Asensio, M. C., 2000. *Transport phenomena during drying of deformable, hygroscopic porous media: Fundamentals and applications*. College Station.
- [82] Wilhelmsson, B., Nilsson, L., Stenstram, S., and Wimmerstedt, R., 1993. "Simulation models of multi-cylinder paper drying". *Drying Technology*, **11**(6), pp. 1177–1203.
- [83] Sidwall, S., Bond, J.-F., and Douglas, W., 1999. "Industrial validation of a multiple technique paper drying simulator". In *Process and Product Quality Conference and Trade Fair*, Vol. 1, pp. 271–302.

- [84] Etemoglu, A., Can, M., Avcı, A., and Pulat, E., 2005. “Theoretical study of combined heat and mass transfer process during paper drying”. *Heat and mass transfer*, **41**(5), pp. 419–427.
- [85] Lu, T., Jiang, P., and Shen, S., 2005. “Numerical and experimental investigation of convective drying in unsaturated porous media with bound water”. *Heat and mass transfer*, **41**(12), pp. 1103–1111.
- [86] Seyed-Yagoobi, J., Bell, D., and Asensio, M., 1992. “Heat and mass transfer in a paper sheet during drying”. *Journal of heat transfer*, **114**(2), pp. 538–541.
- [87] Spolek, G., and Plumb, O., 1981. “Capillary pressure in softwoods”. *Wood Science and Technology*, **15**(3), pp. 189–199.
- [88] Chilton, T. H., and Colburn, A. P., 1934. “Mass transfer (absorption) coefficients prediction from data on heat transfer and fluid friction”. *Industrial & engineering chemistry*, **26**(11), pp. 1183–1187.
- [89] Seyed-Yagoobi, J., Ng, K., and Fletcher, L., 1992. “Thermal contact conductance of a bone-dry paper handsheet/metal interface”. *Journal of heat transfer*, **114**(2), pp. 326–330.
- [90] Churchill, S., and Bernstein, M., 1977. “A correlating equation for forced convection from gases and liquids to a circular cylinder in crossflow”. *Journal of Heat Transfer*, **99**(2), pp. 300–306.
- [91] Eckert, E., and Jackson, T. W., 1950. Analysis of turbulent free-convection boundary layer on flat plate. Tech. rep., DTIC Document.
- [92] COMSOL INC., 2010. *COMSOL V4.3 User Guide*. Burlington, MA.

- [93] Kasza, K., and Chen, M., 1985. “Improvement of the performance of solar energy or waste heat utilization systems by using phase-change slurry as an enhanced heat-transfer storage fluid”. *Journal of Solar Energy Engineering*, **107**, pp. 229–236.
- [94] Hu, X., and Zhang, Y., 2002. “Novel insight and numerical analysis of convective heat transfer enhancement with microencapsulated phase change material slurries: laminar flow in a circular tube with constant heat flux”. *International Journal of Heat and Mass Transfer*, **45**(15), pp. 3163 – 3172.
- [95] Zhang, Y., Hu, X., and Wang, X., 2003. “Theoretical analysis of convective heat transfer enhancement of microencapsulated phase change material slurries”. *Heat and Mass Transfer*, **40**, pp. 59–66. 10.1007/s00231-003-0410-7.
- [96] Ma, H., Cheng, P., Borgmeyer, B., and Wang, Y., 2008. “Fluid flow and heat transfer in the evaporating thin film region”. *Microfluidics and Nanofluidics*, **4**(3), pp. 237–243.
- [97] Chávez, R., Solorio, F., and Cervantes, J., 2011. “Natural convection in a rocking square enclosure: Experimental results”. *ASME Journal of Heat Transfer*, **133**(7).
- [98] Zhang, Y., Rao, Z., Wang, S., Zhang, Z., and Li, X., 2012. “Experimental evaluation on natural convection heat transfer of microencapsulated phase change materials slurry in a rectangular heat storage tank”. *Energy Conversion and Management*, **59**, pp. 33 – 39.
- [99] Delgado, M., Lzaro, A., Mazo, J., and Zalba, B., 2012. “Review on phase change material emulsions and microencapsulated phase change material slurries: Materials, heat transfer studies and applications”. *Renewable and Sustainable Energy Reviews*, **16**(1), pp. 253 – 273.

- [100] Bell, D., Seyed-Yagoobi, J., and Fletcher, L., 1992. *Developments in Paper Drying*, Vol. 5. Hemisphere Publishing Corporation, New York, ch. 6, pp. 203–261.
- [101] Abhat, A., 1983. “Low temperature latent heat thermal energy storage: heat storage materials”. *Solar energy*, **30**(4), pp. 313–332.
- [102] Coleman, H. W., and Steele, W. G., 2009. *Experimentation, validation, and uncertainty analysis for engineers*. John Wiley & Sons.